INTERNATIONAL JOURNAL OF
IJCOE
COASTAL, OFFSHORE & ENVIRONMENTAL ENGINEERING

Volume 5 | Issue 1 | Apr 2020

www.ijcoe.org info@ijcoe.org 17 Volume 5| Issue 1| Apr 2020

International Journal of Coastal, Offshore and Environmental Engineering (IJCOE) | Vol. 5 | Issue. 1 | Apr 2020

International Journal of Coastal, Offshore & Environmental Engineering
Since 2015
ISSN: 2980-8731 (online)

IJCOE
Editor-in-Chief: Prof. Hamid S.Bahai

International Journal of Coastal, Offshore & Environmental Engineering
Since 2015
ISSN: 2980-8721 (online)

In The Name of God

Message from the Editor-in-Chief

The IJCOE journal office was established in 2015,and its first issue was published in 2016. TheIJCOE covers a wide range of research in thefields of oceanography & ocean technology, aswell as marine industries & marine engineering.The editorial board of IJCOE consists of nearly130 of the greatest scientists and researchersfrom over 30 countries worldwide, and thejournal's review board comprises 1,000 membersfrom all five continents. The membership andapplication process for joining the editorial andreview boards of this journal is ongoing. IJCOE isa research-academic quarterly journal that haspublication and distribution permissions fromthe Press Organization and permission topublish scientific-research articles from theMinistry of Science, Research, and Technology(MSRT) with an "A" rating. It also holds a "Q1"rating from the ISC institute with an impactfactor (IF) of approximately 0.43 and isconsidered a "core journal" (prestigious andoutstanding journal). IJCOE is an open-accessjournal and allows the download and receipt ofaccepted articles in full text for free. It respectsand adheres to copyright and COPE regulations.The journal's office operates 24/7, providingservices to researchers. In addition to publishinga regular quarterly journal, IJCOE has 16 specialissues on specific topics in preparation. It alsoprovides conditions for publishing specializedbooks, references, and handbooks. Moreover, itis ready to cooperate with the secretariats ofreputable international conferences to publishtheir selected and outstanding articles. IJCOEevaluates, appraises, and publishes books,articles, and the scientific achievements andfindings of esteemed researchers and scientistsworldwide who are innovating and conductingin-depth research in the "important and strategicfield of the maritime technology & Oceanengineering." It welcomes any form of jointcooperation with universities, research institutes,and related research centers at the national,regional, and international levels, and extends ahand for collaboration.

Classification of Editorial Board in IJCOE

Editor-in-Chief

Director-in-Chief

Deputy Editor

Executive Managers

English Text Editor

Technical Editor

International Editorial Board

National Editorial Board

Editorial Board Associate

Editorial Board Assistant

Guest Editorial Board

Advisory Board

Administrative Coordinator

Honorary Board Member

Methodology Advisor

Author Benefits

- Open Access
- Rapid Publication
- Thorough Peer-Review
- No Copyright Constraints
- Coverage by Leading Indexing Services
- Discounts On Article Processing Charges (APC)
- No Space Constraints, No restriction on the maximum length of the papers, number of figures or colors

INTERNATIONAL JOURNAL OF IJCOE COASTAL, OFFSHORE & ENVIRONMENTAL ENGINEERING

Aims of IJCOE

Hydrodynamics

Marine equipment

Structural mechanics

Ocean environmental predictions

Stochastic calculations Experimental

Automatic Control of Marine Systems

Scope of IJCOE

Marine Hazards

Ocean Acoustics

Naval Architecture

Ocean Engineering

Coastal Engineering

Marine Meteorology

Marine Earth Sciences

Underwater Technology

Marine Renewable Energy

Polar & Arctic Engineering

Marine Renewable Energy

Marine Geography & Geodesy

Marine Environmental Engineering

Automatic Control of Marine Systems

Hydro Physics & Physical Oceanography

Type of papers

- Case Studies
- Book Reviews
- Review Article
- Letters to the Editor
- Methodology Papers
- Editorials and Commentaries
- Response or Rejoinder Papers
- Perspective or Opinion Papers
- Conceptual or Theoretical Papers
- Meta-Analysis and Systematic Reviews
- Short Communications or Brief Reports
- Research Articles (Original Research Papers)

Scientific Research Journal

Ministry of Science, Research And Technology (MSRT)

Jurnal Ranking 2023: A

Ministry Of Science, Research And Technology (ISC)

Citation Impact 2022: 0.429

Quartile 2022 : Q1

Core Collection

IJCOE is a Member of

Cantact Us

Office 1 | Research Institute of Meteorology and Atmospheric Science

Address | Tehran, Shahid Kharrazi Highway, Pajoohesh Blvd, Research Institute of Meteorology and Atmospheric Science, Sand and Dust Storm International Research Center (SDS-IRC), No. 13, 1st floor.

Phone | +982144787652

Postal code | 13611-14977

website | www.rimac.ac.ir

Office 2 | Iranian National Institute for Oceanography and Atmospheric Science

Address | Tehran, Dr. Fatemi Gharbi St., Shahid Etemadzade St., No. 3, third floor.

Phone | +982166944873

Postal code | 13389 – 14118

website | www.inio.ac.ir

Email | Info@ijcoe.org

Website | www.ijcoe.org

Follow Us

www.ijcoe.org

INTERNATIONAL JOURNAL OF IJCOE COASTAL, OFFSHORE & ENVIRONMENTAL ENGINEERING

Volume & Issue:

Volume 5, Issue 1, April 2020

Number of Articles: 6

Content

INTERNATIONAL JOURNAL OF
COASTAL & OFFSHORE ENGINEERING IJCOE Vol.5/No. 1/Spring 2020 (1-9)

Available online at: www. Ijcoe.org

The choice between Radial Basis function and Feed Forward Neural Network to predict long term tidal condition

Hengameh Motamedi[1], Maryam Rahbani [2]*, Abbas Harifi[3], Danial Ghaderi[4]

[1] *MSc. Student, Faculty of Marine Science and Technology, University of Hormozgan, Bandar Abbas 79131, Iran; hengameh.motamedi@gmail.com*
[2*] *Associate Professor, Faculty of Marine Science and Technology, University of Hormozgan, Bandar Abbas 79131, Iran; maryamrahbani@yahoo.com*
[3] *Assistant Professor, Department of Electrical and Computer Engineering, University of Hormozgan, Bandar Abbas 79131, Iran; harifi@hormozgan.ac.ir*
Ph.D. Student, Faculty of Marine Science and Technology, University of Hormozgan, Bandar Abbas 79131, Iran; danialghaderi1@gmail.com

ARTICLE INFO

Article History:
Received: 02 Sep. 2020
Accepted: 18 Oct. 2020

Keywords:
Feed Forward Neural Network
Radial Basis Functions
Tidal Prediction
Beris port

ABSTRACT

Possessing precise water level data in any coastal area is crucial, for any coastal engineering or managements. One of the main processes responsible for a regular water level changes is tide. Due to its nature, tidal prediction is relatively easily accessible. However, the precision of the results depends on the number of constituents have been considered for the prediction. The aim of this paper is to identify the most relevant tidal constituents and their relevant amplitudes for tidal prediction in the Beris port, south of Iran, using artificial neural network (ANN). The main constituents in the area is obtained as M_2, K_1, S_2, N_2 and O_1. To regenerate the tidal condition considering these constituents two ANN methods has been applied including Feed Forward, and Radial Basis Functions (RBF). For the training and network test tidal data of the year 2017 has been considered. For the training a variety of months and constructions has been applied. For the Feed-Forward the Levenberg-Marquardt learning method has been considered. After executing different structures in terms of the number of neurons in the hidden layer and taking into account the minimum error and run time, the network with 5 neurons in the hidden layer and two months training was qualified. For the RBF, the radius of 2.5 has been qualified. The evaluated network of both Feed-Forward and RBF has been employed to reproduce tidal water level of the whole year 2018, and the results were compared with both field data and those derived from harmonic analysis. It was found that the three layers Feed-Forward network shows the best performance in tidal prediction with the correlation coefficient of 0.85, which is followed by RBF, with the correlation coefficient of 0.81.

1. Introduction

Sea level fluctuations caused by celestial gravitational forces and Earth's rotation is known as the tide. The effect of either of the celestial motions or forces including the sun and the moon is introduced as a tidal constituent [1–3]. Thus, each constituent has a specific period, oscillation amplitude, and phase, in which the period is constant throughout the Earth, but the amplitude and phase of each constituent depend on the location of interest [4]. In every aspect of marine science including maritime transport, sedimentation and coastline management, coastal protection, and tidal energy potential assessment, detailed tidal information is required [5, 6]. Table 1 shows the period of fundamental tidal constituents. Each of the frequencies of ω_s, ω_L, ω_1 and ω_5 of Table 1 is used to generate a specific tensile constituent [7, 8].

Table 1: The fundamental astronomical period of motions of the earth, moon and sun [8]

Description	Frequency notation (1/period)	Period (mean solar units)
Sidereal day(one rotation wrt vernal equinox)	Ω	23.9344 hours
Mean solar day(one rotation wrt to the sun)	w_s	24.0000 hours
Mean lonar day(one rotation wrt to the moon)	w_L	24.8412 hours
Period of lunar declination (tropical month)	w_1	27.3216 days
Period of solar declination(tropical year)	w_2	365.2422 days
Period of lunar perigee	w_3	8.847 years
Period of lunar node	w_4	18.613 years
Period of perihelion	w_5	20.940 years

As tides enter the coastal area and shallow water, nonlinear terms of the governing equations on the tidal propagation are activated. These terms represent the effect of shallow water disturbances mathematically, which depending on the type, are divided into two categories including over tide and compound tide [9]. There are several ways to obtain tidal constituents, but the limitations of the areas where an installed buoy records tidal data constantly can sometimes make the acquisition of data difficult and costly. Therefore, tensile prediction methods are always used in terms of time and cost savings. These methods have been developed according to specific region information and do not provide accurate results everywhere. Much research has been done in this field; Lee employed the application of a back-propagation neural network with the short-term measuring data of tidal level in Taichung Harbor in Taiwan to predict the long-term tidal levels [10]. Lee et. al. proposed a program based on harmonic analysis and back-propagation, artificial neural networks to predict tidal condition using short-term measurement data of sea-level records from the Hillarys Boat Harbor tide gauge, Western Australia. The results show that short-term sea-level registrations can be efficiently employed to produce accurate tidal predictions [11]. Okwuashi and Olayinka used the Kalman filter (KF) to forecast the height of tide based on seven main tidal constituents M_2, S_2, N_2, K_2, K_1, O_1, and P_1. The KF was found to outperform the conventional least squares regression technique [12]. Okwuashi et al. examined the novel use of the partial least squares regression (PLSR) as an alternative model to the conventional least squares (LS) model for modeling tide levels. their model is based on twenty tidal constituents: M_2, S_2, N_2, K_1, O_1, MO_3, MK_3, MN_4, M_4, SN_4, MS_4, $2MN_6$, M_6, $2MS_6$, S_4, SK_3, $2MK_5$, $2SM_6$, $3MK_7$, and M_8 [13].

In this study, the prediction of the tide in the Beris port has been performed by comparing two structures of radial basis function (RBF) neural network and three layers feed-forward back-propagation (FFBP) neural network, to find out which one could provide more reliable results. Besides the results are also compared with the harmonic analysis method.

2. Materials and Methods

2.1. Tidal prediction with harmonic analysis

The most common method to analyze tide is harmonic analysis. According to the theory, tidal analysis is the process of breaking a specific tide into its basic constituents. It means considering the effect of the moon, the sun, and their combined effect separately, as well as the shape of the coast and seabed topography [14].

The general equation of harmonic analysis is presented below. Total number of significant tidal constituents are selected considering the duration of tidal oscillation. Therefore, The height of the tide at time *t* can be computed by expressing it as the sum of harmonic terms [13];

$$Y(t) = A_0 + \sum_{i=1}^{N} h_i \cos(\omega_i t + \varepsilon_i) \quad (1)$$

For accurate tidal analysis, all astronomical periods must be used, meaning 18.6 years of sea-level observations are needed, which is quite a time consuming and in most of the coastal area is still not available. This issue can be resolved by entering the related components of the moon, the sun, and other parameters involved, in the equations and calculating the effects of these constituents. The linear model of the above equation is in the form of Equation 2.

$$h(t) = A_0 + \sum_{i=1}^{N} (A_i \cos(\omega_i t) + B_i \sin(\omega_i t)) \quad (2)$$

where, A_0 is the height of mean water level above the datum, A_i and B_i are the tidal constituent amplitudes, ω_i represents the tidal frequencies, *h(t)* denotes the height of the tide at time *t*, and *N* is the number of tidal constituents selected for tidal analysis [13], [15]. Having instantaneous water level records in a location, tidal constituent amplitudes can be calculated, for tidal prediction.

2.2. Artificial neural networks

Artificial neural networks (ANN) is a subset of artificial intelligence techniques, it's structure and function of which are like those of the human brain [16]. This system is consists of a large number of processing elements called neurons that coordinate with each other to solve a problem and connect input to output [17]. A neural network includes layers and weights, and its behavior dependents on the relationship between members. A neural network is composed of input, hidden and output layers. The input layer only receives the information and acts as an independent variable; on the other hand, the outer layer functions as the dependent variable and the number of its neurons depends on the number of dependent variables. In addition to the input and output layers, a neural network also includes a hidden layer which is the main part of processing [18].

A neural network is made up of artificial neurons which has the task of data processing. These neurons are connected to each other, to process received input information, and produce the desired output through the appropriate transfer function. The actual output depends on the special transfer function selected.

There are different types of ANN with different transfer functions, each with its own capabilities and features, so a suitable neural network must be selected to achieve the desired prediction result. In this study, a multilayer feed-forward neural network, as a well-known method, has been compared with the radial functions neural network for tidal prediction, in order to find which one is more reliable for tidal prediction.

2.2.1. Feed Forward Back-Propagation (FFBP) Neural Network

The most common back-propagation neural network architecture is the multilayer FFBP [19–21]. In this method network processors are divided into several layers, the minimum number of layers in these networks being two. Figure 1 shows the structure of a two (Figure 1A) and three (Figure 1B) layers FFBP network.

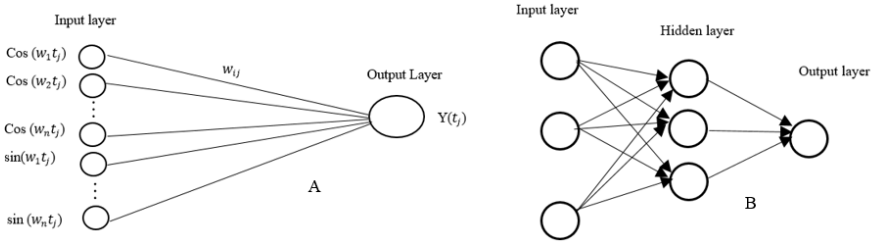

Figure 1: Structure of FFBP Network. A) Two layers and B) Three layers [14]

As mentioned, appropriate transfer functions must be selected according to the type of function and layer used. In the three-layer FFBP network, the tan-sigmoid transfer function and linear transfer function are used [22, 23]. Relationships 3 show how to obtain the tan-sigmoid functions: [24].

$$F(x) = \frac{1}{(1 + e^{-1})} \qquad (3)$$

An important aspect of the ANN is their training process. Training is generally a process that determines the weight and bias. There are different training algorithms to train the neural network, Levenberg-Marquardt among them is the one used in this study. The Levenberg-Marquardt is a method in which the second derivative known as the Hessian matrix is used in addition to the first derivative (the Jacobian matrix). One of the advantages of this method is that it does not need to determine the learning rate from the beginning and the algorithm is able to adjust the learning rate adaptively [25, 26]. In this algorithm, the method of changing the processing parameters of neural network neurons is calculated from relationship 4:

$$X_{k+1} = xk - [H + \eta^I]^{-1}\ J^T\ e(t) \qquad (4)$$

Where, *k* is repetitive learning counter, *x* represents the vector of weights and bias, *e(t)* denotes the error, is the training rate, *H* represents the Hessian matrix, and *J* represents the Jacobson matrix [27].

2.2.2. Radial Basis Function (RBF) Neural Network

The network of RBF requires a large number of neurons for training. The performance of these networks is also best achieved if a large number of training vectors are used [28]. RBF networks have just two layers (Figure 2), the first of which is of radial basis type and the output layer is linear. The network parameters here include the spread number and the goal number. By changing these two parameters, the network performance can be improved [29, 30].

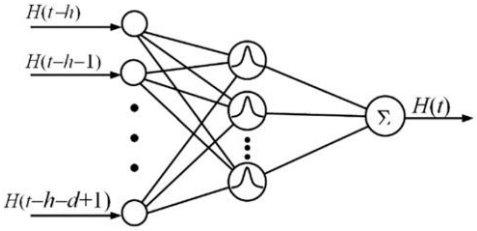

Figure 2: Structure of Radial Basis Function Neural Network [31]

The Gaussian transfer function is used in the RBF network [8]. Relationship 5 show how to obtain Gaussian transfer functions:

$$F(x) = a\, e^{-\frac{(x-b)^2}{2c2}} \quad (5)$$

where, *e* is Euler's number, *a*, *b* and *c* are real constant coefficients.

2.3. Study Area

For this study Beris port has been chose, which is located along the Makran coasts, northern part of the Gulf of Oman. This port has been selected since it has a characteristic of a coastal ocean. Longitude and latitude of the Beris port is 61°10´ and 25°08´ respectively. This port is located 85 km east of Chabahar [32, 33]. The water depth inside the por is approximately 5 meters [34]. The port of Beris bordered from the east by Goiter Bay and from the west by the Chabahar Bay. The port of Beris is mostly known as fishing port [32]. The average temperature is 36.2 °C in summer and 16 °C in winter. According to the tidal records, the highest and the lowest tidal range in this port is about 2.97m, and 1 m respectively. In addition, tidal regime in the port is semidiurnal type. Figure 3 shows the location of the Makran coast and the Beris port. As it can be seen Gulf of Oman is the extension of Indian ocean; Thus, the water depth in the coastal area deepen suddenly. Figure 3 shows the bathymetry of the area according to the ETOP1 data [35], and Figure 3B specifically shows that the depth around the Beris port is about 20 to 30 m.

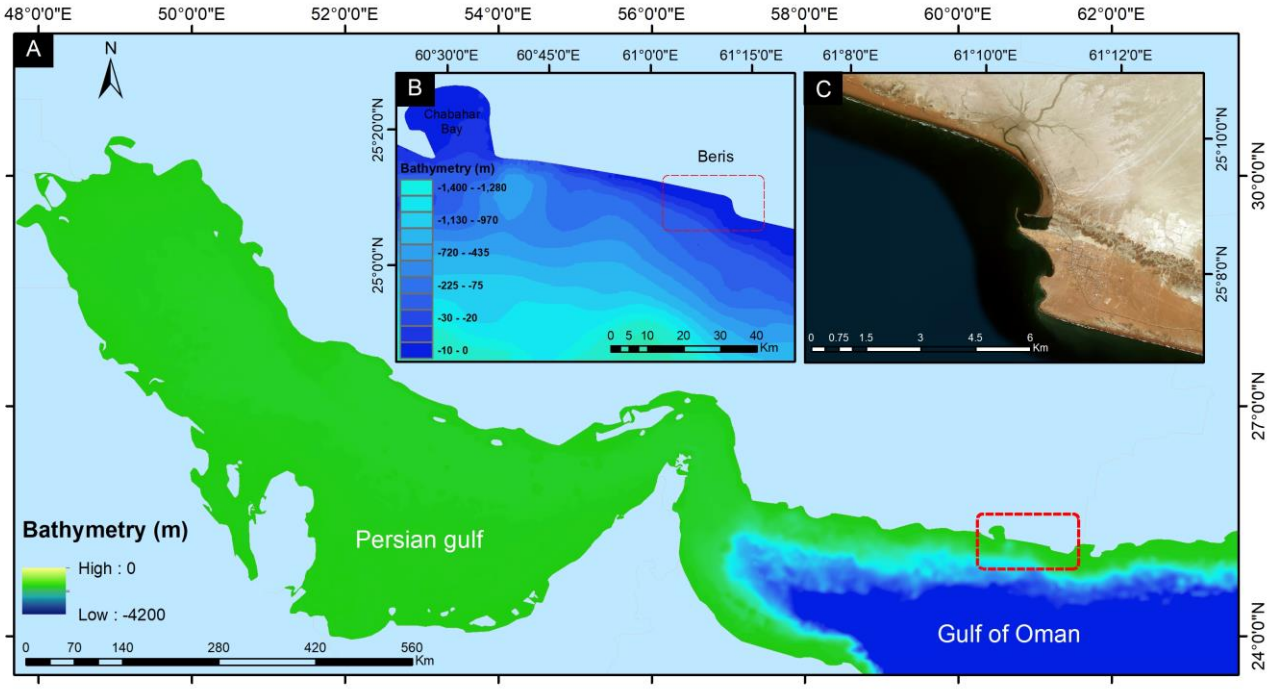

Figure 3: Location of the Beris port, relative to Iran and the Gulf of Oman. A) Bathymetry of the Persian Gulf and the Gulf of Oman, B) Bathymetry changes in areas near Beris port (Taken from ETOPO1 data [35]), and C) Satellite image of Beris port (Taken from Landsat 8 RGB bands) [36]

2.4. The evaluation method

To evaluate the accuracy of the proposed method, the mean squared error (MSE) index and correlation coefficient (R) are used. Relationships 6 and 7 show how these indices are obtained.

$$MSE = \frac{\sum_i^N (y_i - x_i)^2}{N} \quad (6)$$

$$R = \frac{\sum (x_i - \bar{x})\,(y_i - \bar{y})}{\sqrt{\sum (x_i - \bar{x})^2 \;\; \sum (y_i - \bar{y})^2}} \quad (7)$$

In relationships 6 and 7, x_i is the measured data, y_i is the predicted data, N is the number of data, $\bar{x}$ is the mean of the measured data, and $\bar{y}$ is the mean of the predicted data.

3. Results and discussions

3.1. Determining suitable tidal constituent for neural network inputs

It is obvious that considering the more number of tidal constituents means the closer condition to the reality. However, it should be considered that adding too many tidal constituents in ANN does not necessarily improve the predictive results. Sometimes adding unnecessary constituents only slightly improves results, and sometimes confuses the learning process. Therefore, at the very beginning the main tidal constituents efficient,

in the area under investigation, must be determined. That is, to apply major tidal constituents and their corresponding weights as input to the ANN. For this, the neural network structure without a hidden layer (Figure 1A) has been used. Lee, Lee at al. and Anran et. al. showed that 42 tidal constituents as input to ANN will cause optimal performance, for predicting tidal oscillation [10, 11], [37]. The tidal data of the years 2017 and 2018 has been used for network training and network testing respectively. To find out the proper months of training, the method of trial and error has been considered. Table 2 shows part of the procedure. Between 2 and 5 months of training, as the months of training increases, the order of tidal constituents involved, and their amplitude change. Above 5 training months, the ten most important tidal constituents are constant, and their corresponding amplitude varies slightly. Thus, 5 training months were considered.

Table 2: Trial to find proper number of training months

Training Months	Ten most important constituents	Corresponding Amplitude	MSE	Correlation coefficient
2	M_1, No_1,CHI_1 ,S_2,BET_1 ,R_2,M_2,T_2, SA,S_1	5.31, 4.77, 1.05, 1.02, 0.70, 0.67, 0.46, 0.44, 0.36, 0.37	60.78	0.04
3	M_2,S_2,K_1, M_1, N_2 , No_1,O_1,R_2,T_2,S_1	0.46, 0.26, 0.21, 0.17, 0.17, 0.16, 0.12, 0.08, 0.06, 0.05	0.19	0.75
4	M_2,S_2,K_1,N_2,O_1, No_1, M_1, S_1, R_2, NU_2	0.45, 0.21, 0.21, 0.15, 0.12, 0.063, 0.061, 0.060, 0.057, 0.045	0.15	0.78
5	***M_2, K_1, S_2, N_2, O_1, S_1, NU_2, MSF, P_1, No_1***	***0.44, 0.20, 0.19, 0.14, 0.11, 0.046, 0.044, 0.041, 0.035,0.032***	***0.13***	***0.81***
6	M_2, K_1, S_2, N_2, O_1, S_1, NU_2, MSF, P_1, No_1	0.44, 0.21, 0.18, 0.13, 0.11, 0.044, 0.041, 0.041, 0.030, 0.027	0.12	0.83
7	M_2, K_1, S_2, N_2, O_1, S_1, NU_2, MSF, P_1, No_1	0.44, 0.21, 0.18, 0.12, 0.11, 0.04, 0.039, 0.038, 0.028 0.027	0.10	0.84
8	M_2, K_1, S_2, N_2, O_1, S_1, NU_2, MSF, P_1, No_1	0.44, 0.21, 0.18, 0.18, 0.11, 0.040, 0.035, 0.032, 0.029, 0.024	0.10	0.85

The 42 tidal constituents and their corresponding's amplitude derived from the network are presented in Figure 4A, and in descended order in Figure 4B. The major constituents determining the tide at Beris port are the semi-diurnals (M_2, S_2 and N_2) and diurnal (O_1 and K_1) constituents. Among weakly tidal constituents, MS_4 and MN_4 are weaker, so, it seems they do not play important role in this area. Constituent impact ratio implies that the shallow water constituents (M_4 . M_6) are not significant in this area either, which is reasonable considering the feature of the area, with relatively steep coastal slope (Figure 3B).

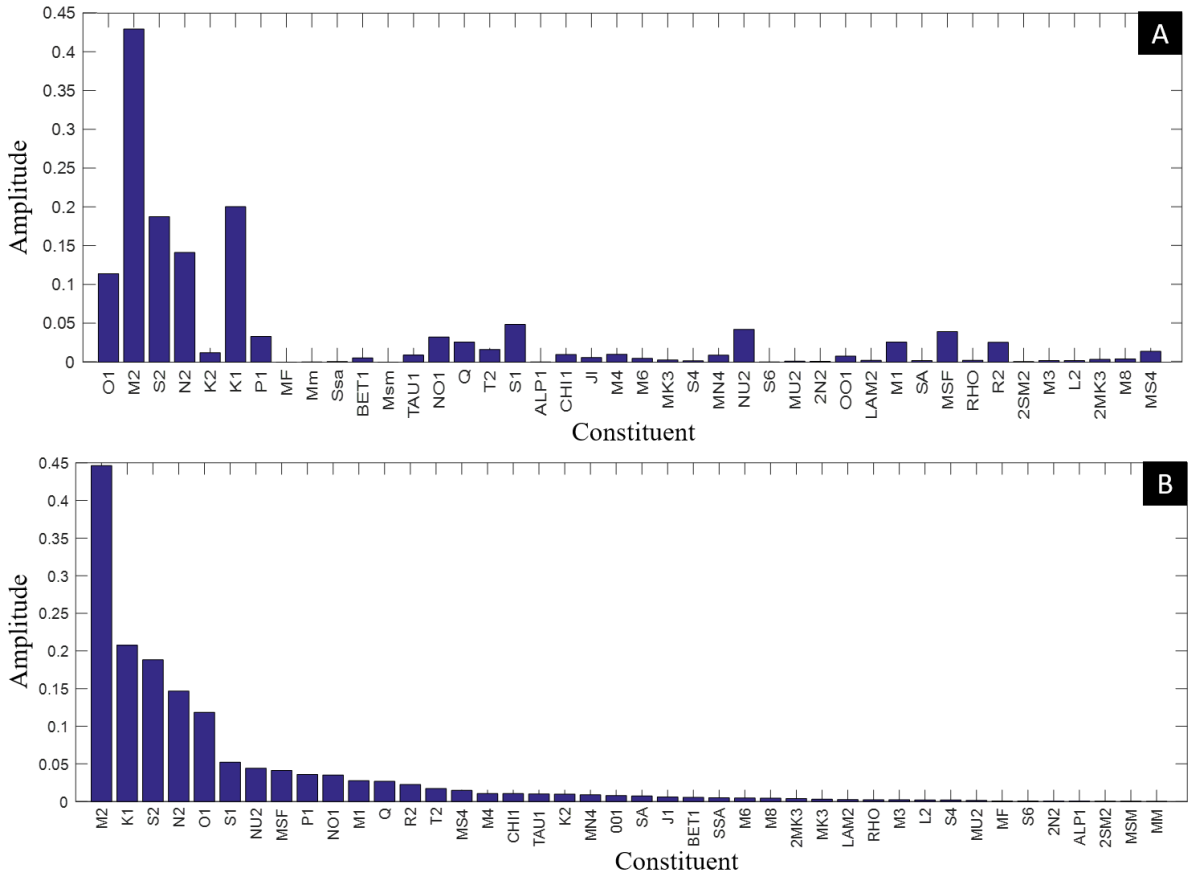

Figure 4: A) The amplitude of 42 tidal constituents shape the tide in Beris port employing 5 months training. B) The same constituents in descending order

Having major harmonic tidal constituents of the area including M_2, K_1, S_2 and O_1, it is possible to calculate Dietrich form number, to determine the regional tidal type [38, 39] for the area under investigation. Employing equation 8 the value of form factor is calculated as 0.49. This means the area can be considered as mixed mainly semidiurnal (0.25 <F <1.5), which is in agreement with Mahmodaf and Bagheri, 2018 study [40].

$$F = \frac{H_{K_1} + H_{o_1}}{H_{M_2} + H_{s_2}} \quad (8)$$

When most relevant tidal constituents and their amplitude verified, these constituents should be used for predicting tidal range of the year 2018. The question is how many of the constituents should be involved to derive precise prediction. To find out the proper number of constituents involved several executions carried out, starting from 4 most relevant constituents. The output results were compared with actual tidal data of 2018, and MSE was calculated. Results are presented in Table 3. It can be seen that the five constituents show the lowest MSE error. Considering Figure 4 it is obvious that the M_2 (the lunar semi-diurnal constituent) has the highest impact, besides, K_1 (Solar and Lunar diurnal constituent), S_2 (the Solar Semi-diurnal constituent), N_2 (Lunar Elliptic Semi-diurnal constituent) and O_1 (Lunar diurnal constituent) have relatively high impact (amplitude). These five constituents therefore selected as inputs for the further procedure.

Table 3: Test of various tidal constituents using FFBP network without the hidden layer (Beris port)

Name of input tidal constituent	MSE
M_2, ,K_1,S_2, N_2	0.1176
M_2, ,K_1,S_2, N_2,O_1	0.1132
M_2, ,K_1,S_2, N_2,O_1, S_1	0.1228
M_2, ,K_1,S_2, N_2,O_1, S_1, NU_2	0.1321
M_2, ,K_1,S_2, N_2,O_1, S_1, NU_2, MSF	0.1412
M_2, ,K_1,S_2, N_2,O_1, S_1, NU_2, MSF, P_1	3.1024
M_2, ,K_1,S_2, N_2,O_1, S_1, NU_2, MSF, P_1, NO_1	21.5272

3.2. Tidal prediction with three-layer FFBP neural network

After the optimum number of tidal constituents were selected, they should be feed to the selected network to be trained for prediction tidal conditions. As mentioned FFBP network is one of the most known among ANN. It has been, therefore, employed for predicting Beris port tidal conditions.

Three layers network was considered proper. Values of $cos(w_i t)$ and $sin(w_i t)$ of the five selected constituents are considered as input layer. A single hidden layer was considered suitable for an overall reliable estimate, which was also suggested by Hornik's, 1989 [41]. Finally, the water level as a tidal condition was considered as output.

Network training was evaluated through bunch of tests with a variety of a number of neurons and days of the year 2017, in order to predict the whole tidal condition of the year 2018. Many tests were performed with 7, 15, 30, and 60 days and 1, 5, 7, 10, and 15 neurons. The output of these tests was compared with the actual field data, and the MSE error and correlation coefficient of them were calculated. The results of some of these tests are presented in Table 4. Among the various tests as shown in Table 4, the lowest error and best correlation belonged to the test with 60 days of observational data and 5 neurons in the hidden layer.

Table 4: Test of various number of hidden layer neurons with the number of days of training (7, 15, 30, 60)

Number of training days	Number of neurons	MSE	Correlation coefficient
7	1	0.14	0.80
7	10	0.15	0.79
15	5	0.13	0.81
15	15	0.12	0.82
30	5	0.12	0.83
30	7	0.13	0.81
60	***5***	***0.10***	***0.85***
60	15	0.12	0.84

3.3. Tidal prediction with Radial Basis Function neural networks

As mentioned before, in RBF network the training can be achieved either when the error reaches the specified limit or when the network reaches the specified number of neurons and stops [42]. Here different radius numbers have been given to the network for the specified error, which has been gained in the three-layer FFBP network. The optimal point is then considered based on the computation time and the number of neurons. The output of each execution was compared with the actual tide data, and MSE error was calculated.

Table 5 represents the radius, number of neurons, and the MSE values for some of the executed tests. As mentioned, the goal for all of the execution was achievement to a specified error, on the basis of varying radius. Thus, this network could determine the radius that performs the results best. According to Table 5 the radius of 2.5 of RBF has the best performance to reproduce tidal data.

Figure 5 shows the distribution graph of the tidal condition derived from the three-layer FFBP network (Figure 5A), the RBF network (Figure 5B), and the harmonic analysis (Figure 5C) against the field data, for the year 2018. Accumulation of data around the diagonal axis (fit) indicates the proper performance of the three-layer FFBP network. It can be seen that the correlation coefficient is 0.85 for the three-layer FFBP neural network, 0.81 for the RBF network, and 0.83 for the harmonic analysis, which shows the acceptable accuracy of the three-layer FFBP neural network in predicting tidal condition, following by the RBF network.

Table 5: Test of various radius in the RBF network

Radius	Number of neurons	MSE
0.5	1650	1.830
1	300	0.536
1.5	50	0.153
2	50	0.129
2.5	***50***	***0.125***
3	0	0.129

Table 6: Correlation coefficient and MSE for predicting tidal condition in Beris port using FFBP network, RBF network, and harmonic analysis

Model	correlation coefficient	MSE
FFBP network	***0.85***	***0.101***
RBF network	0.81	0.125
Harmonic analysis	0.83	0.123

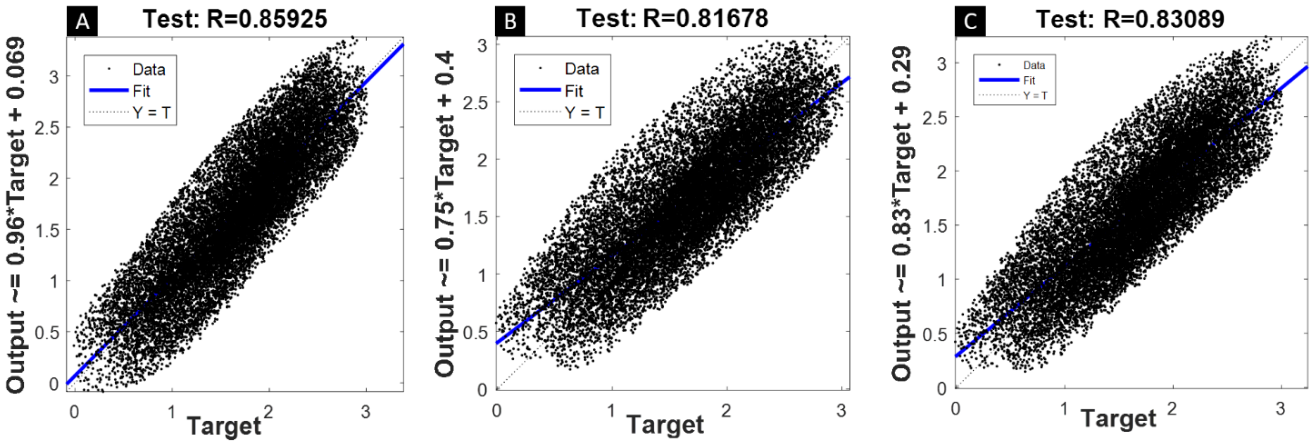

Figure 5: Distribution graph for one year tidal condition prediction using; A) FFBP network, B) RBF network, and C) Harmonic analysis against field data

Figure 6 presents the time series of tidal conditions predicted using the three-layer FFBP network, RBF network, and Harmonic analysis method, in comparison with the field data for the first 1000 time steps of 2018, (from 2018/01/01 to 2018/21/01). According to the figure, the tidal condition predicted by the FFBP network is in the best agreement with the field data.

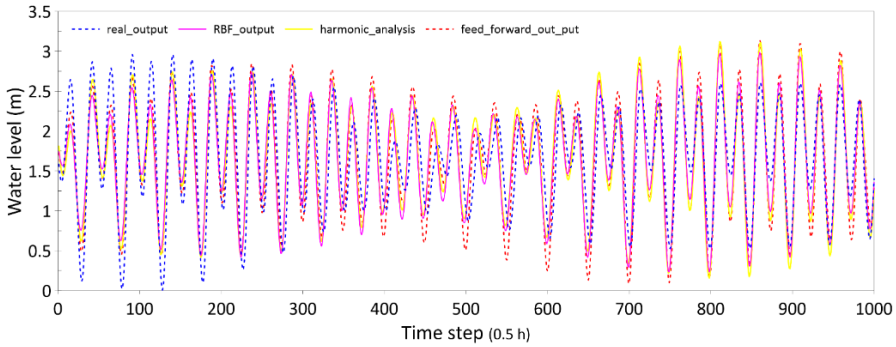

Figure 6: Time series of tidal condition predicted using FFBP network, RBF network, and Harmonic Analysis, in compare with the field data at Beris port for the year 2018 (from 2018/01/01 to 2018/21/01)

4. Conclusions

Even though the tidal water level is relatively easy to predict, its precision however depends on the number of tidal constituents that are considered for the prediction. In this research, the artificial neural network has been applied for this purpose. A feed forward back propagation neural network without hidden layer has been employed to provide the most relevant tidal constituents and their representative amplitude for Bris port, located in the northern of Gulf of Oman. According to the outcome M_2, K_1, S_2, N_2 and O_1 are the five major constituents, with the respective amplitudes of 0.44, 0.2, 0.19, 0.14, and 0.11, which play main role in the area. These five tidal constituents have been used for the prediction of tidal conditions for the year 2018 at Beris port. For this progress, two different neural networks were considered, including feed-forward backpropagation and radial bias function. The results then were compared with the harmonic analysis results and field data. It was found that the three-layer feed-forward backpropagation network with 60 days of training and 5 neurons in the hidden layer gives the best performance in terms of MSE error (0.101), correlation coefficient (0.85), and time consumption. For the radial bias function network the best performance was achieved with the radial 2.5, with the correlation coefficient of 0.81.

References

[1] *W. Wang and H. Yuan, "A Tidal Level Prediction Approach Based on BP Neural Network and Cubic B-Spline Curve with Knot Insertion Algorithm," Mathematical Problems in Engineering, vol. 2018, 2018.*

[2] *D. Pugh and P. Woodworth, Sea-level science: understanding tides, surges, tsunamis and mean sea-level changes. Cambridge University Press, 2014.*

[3] *M. Guan et al., "A method of establishing an instantaneous water level model for tide correction," Ocean Engineering, vol. 171, pp. 324–331, 2019.*

[4] *S. Cai, L. Liu, and G. Wang, "Short-term tidal level prediction using normal time-frequency transform," Ocean Engineering, vol. 156, pp. 489–499, 2018.*

[5] *G. W. Platzman, "Ocean tides and related waves," Mathematical problems in the geophysical sciences, vol. 14, no. Part 2, pp. 239–291, 1971.*

[6] *B. Hong et al., "Potential physical impacts of sea-level rise on the Pearl River Estuary, China," Journal of Marine Systems, vol. 201, p. 103245, 2020.*

[7] *Y. H. Song, Q. X. Xuan, and A. T. Johns, "Comparison studies of five neural network based fault classifiers for complex transmission lines," Electric power systems research, vol. 43, no. 2, pp. 125–132, 1997.*

[8] *B. B. Parker, "Tidal analysis and prediction.," 2007.*

[9] *E. A. Fanjul, B. P. Gómez, and I. R. Sánchez-Arévalo, "A description of the tides in the Eastern North Atlantic," Progress in Oceanography, vol. 40, no. 1, pp. 217–244, 1997.*

[10] *T.-L. Lee, "Back-propagation neural network for long-term tidal predictions," Ocean Engineering, vol. 31, no. 2, pp. 225–238, 2004.*

[11] *T.-L. Lee, O. Makarynskyy, and C.-C. Shao, "A combined harmonic analysis--artificial neural network methodology for tidal predictions," Journal of Coastal Research, vol. 23, no. 3 (233), pp. 764–770, 2007.*

[12] *O. Okwuashi and D. N. Olayinka, "Tide modelling using the Kalman filter," Journal of Spatial Science, vol. 62, no. 2, pp. 353–365, 2017.*

[13] *O. Okwuashi, C. Ndehedehe, and H. Attai, "Tide modeling using partial least squares regression," Ocean Dynamics, vol. 70, no. 8, pp. 1089–1101, 2020.*

[14] *G. Li, Y. Hao, and Y. Zhao, "Research of neural network to tidal prediction," in 2009 International Joint Conference on Computational Sciences and Optimization, 2009, vol. 2, pp. 282–284.*

[15] *F. A. Madah, "The amplitudes and phases of tidal constituents from Harmonic Analysis at two stations in the Gulf of Aden," Earth Systems and Environment, vol. 4, no. 2, pp. 321–328,*

2020.

[16] R. O. Strobl and F. Forte, "Artificial neural network exploration of the influential factors in drainage network derivation," Hydrological Processes: An International Journal, vol. 21, no. 22, pp. 2965–2978, 2007.

[17] R. Özçelik, M. J. Diamantopoulou, J. R. Brooks, and H. V Wiant Jr, "Estimating tree bole volume using artificial neural network models for four species in Turkey," Journal of environmental management, vol. 91, no. 3, pp. 742–753, 2010.

[18] J. A. Anderson, An introduction to neural networks. MIT press, 1995.

[19] A. M. Salim, G. S. Dwarakish, K. V Liju, J. Thomas, G. Devi, and R. Rajeesh, "Weekly prediction of tides using neural networks," Procedia Engineering, vol. 116, no. 1, pp. 678–682, 2015.

[20] B. L. Meena and J. D. Agrawal, "Tidal level forecasting using ANN," Procedia Engineering, vol. 116, pp. 607–614, 2015.

[21] L. Pashova and S. Popova, "Daily sea level forecast at tide gauge Burgas, Bulgaria using artificial neural networks," Journal of Sea Research, vol. 66, no. 2, pp. 154–161, 2011.

[22] M. Janati, M. Kolahdoozan, and H. Imanian, "Artificial Neural Network Modeling for the Management of Oil Slick Transport in the Marine Environments," Pollution, vol. 6, no. 2, pp. 399–415, 2020.

[23] S.-W. Kim, A. Lee, and J. Mun, "A Surrogate Modeling for Storm Surge Prediction Using an Artificial Neural Network," Journal of Coastal Research, no. 85, pp. 866–870, 2018.

[24] W. J. Palm, Introduction to MATLAB 7 for Engineers, vol. 7. McGraw-Hill New York, 2005.

[25] A. J. Adeloye and A. De Munari, "Artificial neural network based generalized storage--yield--reliability models using the Levenberg--Marquardt algorithm," Journal of Hydrology, vol. 326, no. 1–4, pp. 215–230, 2006.

[26] M. T. Hagan and M. B. Menhaj, "Training feedforward networks with the Marquardt algorithm," IEEE transactions on Neural Networks, vol. 5, no. 6, pp. 989–993, 1994.

[27] R. Battiti, "First-and second-order methods for learning: between steepest descent and Newton's method," Neural computation, vol. 4, no. 2, pp. 141–166, 1992.

[28] Z.-G. Zhang, J.-C. Yin, and C. Liu, "A modular real-time tidal prediction model based on Grey-GMDH neural network," Applied Artificial Intelligence, vol. 32, no. 2, pp. 165–185, 2018.

[29] M. H. Beale, M. T. Hagan, and H. B. Demuth, "Neural Network Toolbox™, User's Guide, MATLAB®R2015a, The MathWorks," Inc., Natick, MA, USA, vol. 410, 2015.

[30] S. E. Vt and Y. C. Shin, "Radial basis function neural network for approximation and estimation of nonlinear stochastic dynamic systems," IEEE transactions on neural networks, vol. 5, no. 4, pp. 594–603, 1994.

[31] J. Yin, Z. Zou, and F. Xu, "Sequential learning radial basis function network for real-time tidal level predictions," Ocean engineering, vol. 57, pp. 49–55, 2013.

[32] S. Ardani and M. Soltanpour, "Modelling of sediment transport in Beris fishery port," Civil Engineering Infrastructures Journal, vol. 48, no. 1, pp. 69–82, 2015.

[33] D. Ghaderi and M. Rahbani, "Detecting shoreline change employing remote sensing images (Case study: Beris Port-east of Chabahar, Iran)," International Journal of Coastal and Offshore Engineering, vol. 3, pp. 1–8, 2020.

[34] M. Sayehbani and D. Ghaderi, "Numerical Modeling of Wave and Current Patterns of Beris Port in East of Chabahar-Iran," International Journal of Coastal and Offshore Engineering, vol. 3, no. 1, pp. 21–29, 2019.

[35] C. Amante and B. W. Eakins, "ETOPO1 arc-minute global relief model: procedures, data sources and analysis," 2009.

[36] United States Geological Survey, "EarthExplorer," 2020. https://earthexplorer.usgs.gov/ (accessed Aug. 02, 2020).

[37] A. Zhang, J. Yin, J. Hu, and C. Yu, "Modular tidal level short-term forecasting based on BP neural networks," in Proceedings of the 33rd Chinese Control Conference, 2014, pp. 5037–5042.

[38] M. G. Foreman, "G, 1977: Manual for tidal heights analysis and prediction," Pac. Mar. Sci. Rep, vol. 77, no. 10, 1977.

[39] G. Dietrich and K. Kalle, "General oceanography; an introduction," 1957.

[40] M. Mahmoudof and M. Bagheri, "Determination of Compound and Overtide Constituents near the Eastern Iranian Coast of Makran," Journal of Oceanography, vol. 10, no. 37, pp. 33–41, 2019, doi: 10.29252/joc.2019.10.12162.

[41] K. Hornik, M. Stinchcombe, H. White, and others, "*Multilayer feedforward networks are universal approximators*.," Neural networks, vol. 2, no. 5, pp. 359–366, 1989.

[42] E. Sertel, H. K. Cigizoglu, and D. U. Sanli, "*Estimating daily mean sea level heights using artificial neural networks*," Journal of Coastal Research, vol. 24, no. 3 (243), pp. 727–734, 2008.

INTERNATIONAL JOURNAL OF
COASTAL & OFFSHORE ENGINEERING
IJCOE Vol.5/No. 1/Spring 2020 (11-23)

Wave Reflection of irregular waves from Multi-Layer Berm Breakwaters

Majid Ehsani[1], Mohammad Navid Moghim[2*], Mehdi Shafieefar[3], Amir Mostaghiman[4]

[1] *PhD, Department of Civil Engineering, Isfahan University of Technology, Isfahan, Iran; majid.ehsani@cv.iut.ac.ir*
[2*] *Associate Professor, Department of Civil Engineering, Isfahan University of Technology, Isfahan, Iran; moghim@iut.ac.ir*
[3] *Professor, Department of Civil and Environmental Engineering, Tarbiat Modares University, Tehran, Iran; shafieefar@modares.ac.ir*
[4] *MSc Student, Department of Civil Engineering, Isfahan University of Technology, Isfahan, Iran; a.mostaghiman@cv.iut.ac.ir*

ARTICLE INFO

Article History:
Received: 17 Mar. 2020
Accepted: 21 Oct. 2020

Keywords:
Wave Reflection
Multi-layer berm breakwater
Experimental study
Prediction formula

ABSTRACT

One of the emerging issues from an efficacious design of berm breakwaters is the estimation of wave reflection. In the present study, the wave reflection of a multi-layer berm breakwater (MLBB) has been studied based on model experimentation. To gain this goal, two-dimensional model tests have been carried out in a wave flume at Tarbiat Modares University. Irregular waves were generated using the JONSWAP spectrum. The effect of various parameters like wave height, wave period, water depth, and berm elevation from still water level is investigated on the wave reflection. The achieved outcomes of this study proposes a new formula estimating MLBBs wave reflection. Finally, the performance of the derived formula against the existing formulae proposed by other researchers is checked thoroughly. The results of the statistical evaluation indices revealed that the predicted wave reflection using the new formula is more accurate than the existing ones. Thus, it would be obvious that the present formula can provide a well-founded estimation of wave reflection on the MLBBs. Moreover, the new formula and those estimated by existing ones are validated by employing the data set exclusively used in drawing the comparison. This fair validation illustrates that the current formula is more accurate than the existing formulae.

1. Introduction

In the early 1980s, berm breakwaters had been evolved by accepting the reshaping concept in rubble mound breakwaters in the course of wave action on the front slope. Berm breakwaters are a particular type of rubble mound breakwaters built with a porous berm above the still water level at the seaward side [1]. This type of structure can be divided into two disparate categories encompassing homogeneous berm breakwaters (HBBs) and multi-layer berm breakwaters (MLBBs). The HBB's armor layer comprises only one stone grading, whereas the MLBB's armor layer consists of several stone classes with unique stone gradation [2].

Since MLBBs have been typically constructed in Iceland – over 20 cases so far - they are also celebrated as Icelandic berm breakwaters [3]. Due to the wave attack, these structures perform more or less as statically stable structures, depending on the stability number. Moreover, the armor layer stones are sorted into diverse classes in accordance with their sizes [4]. The overwhelming advantage of using various classes in the structure could be the extensive utilization of dedicated quarries [5]. The largest rock size is categorized as 'class I', located in front of the berm, and even sometimes at the upper slope of the berm, which plays a quite prominent role in the stability of the structure. On the contrary, the smaller stone classes are placed in the lower parts of the slope and inner layers, where the influence of the wave is not significant. Typically, these classes are from the same dimensions of rocks used in the armor layer of HBBs [3]. Figure 1 demonstrates the different parameters schematically in an MLBB. Overall, one can express the advantages of MLBBs, including the utilization of dedicated quarry optimally, narrow stone gradation, and providing a high level of porosity, dissipating the wave energy greatly, lowering the stone gradation, and providing higher interlocking.

Hydraulic responses such as wave reflection, wave overtopping, run-up and run-down, and wave transmission are assumed to be determining factors in the design process of disparate coastal structures. Figure 2 gives an excellent display of these parameters

[6]. Providing further details, it is self-evident that the incident wave energy would definitely end up with reflection, dissipation and/or even transmission into the bay. The reflected wave from natural beaches or even human-made structures would considerably affect the sediment movements and hydrodynamics created at the toe of the structure [7]. Concerning this fact, a meticulous study into the nature of wave reflection in marine structures is crucial to be conducted. In the case of high reflection, the interaction of incident and reflected waves could potentially bring an extremely chaotic area into existence all along with very steep, standing, and breaking waves. Accordingly, on the one hand, it would be difficult to navigate in front of the bay entrance for smaller vessels in the presence of high reflected waves. On the other hand, these waves would increase the scouring level at the toe of the structure, the erosion at nearby beaches, and eventually behave towards the destabilization of the structure [8, 9]. On the whole, the prediction of wave reflection from coastal structures such as the rubble mound breakwaters is of utmost importance owing to its adverse effects [10].

The wave reflection is commonly expressed by the reflection coefficient (C_r). This coefficient is defined as the ratio of the reflected wave height to the incident wave height or of the root square ratio of the reflected wave energy to the incident wave energy as follows:

$$C_r = \frac{H_r}{H_i} = \sqrt{\frac{E_r}{E_i}} \qquad (1)$$

where H_i is the incident wave height, H_r is the reflected wave height, E_i is the incident wave energy, and E_r is the reflected wave energy.

For the design of rubble mounds, the reflection coefficient is one of the most significant hydraulic replies of a breakwater. Over the past 60 years, a diversity of experimental formulae predicting C_r, primarily inspired by Miche's approach [11] and expanded by Battjes [12], have been proposed. This approach presumes that the reflection process is governed by the wave breaking. First, investigations on the wave reflection date back to (1974) by Battjes, who theoretically derived a formula for the reflection coefficient [12]. He assumed C_r as a function of Iribarren number $(\xi = \frac{tg\alpha}{\sqrt{H_i/L_{om}}})$ and introduced Eq. (2) for smooth-impermeable slopes.

$$C_r = 0.1\xi^2 \qquad (2)$$

where, ξ is the Iribarren number, α is the front slope angle, $L_{om}=gT_m^2/2\pi$ is the deep-water wave-length, T_m is the mean wave period, and g is the gravitational acceleration.

A large number of researchers have sought to determine the wave reflection on the rubble mound breakwaters and proposed or even elaborated some formulae to estimate the reflection coefficient, e.g., Losada and Gimenez-Curto [13], Seelig and Ahrens [14], Postma [15], Hughes and Fowler [16], Chegini et al. [17], Davidson et al. [8], Muttray et al. [18], Zanuttigh and Van der Meer [19, 20], Calabrese et al. [21], Zanuttigh and Lykke Andersen [10], Park et al. [22], Van der Meer and Sigurdarson [23], Mahmoudi et al. [24] and Buccino et al. [25].

Postma [15] carried out 300 tests on rock slopes to investigate the effect of wave period, wave height, front slope, water depth, permeability, stone gradation, and spectral shape on wave reflection. The results obtained from his study disclose the great dependency of C_r upon wave period, front slope, and also the permeability, but marginal dependency on wave height and inconsiderable correlations with spectral form and water depth. More to his investigation, he proposed an empirical formula corresponding to

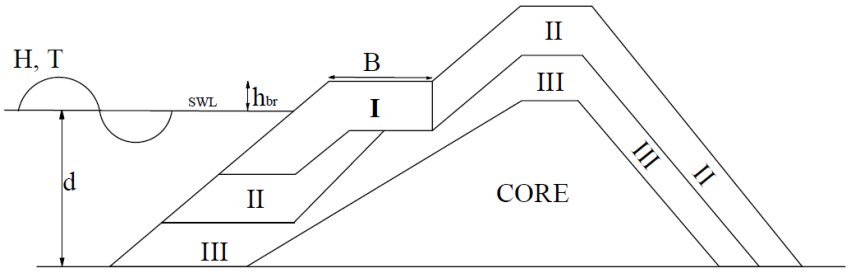

Figure 1. Illustration of various parameters in an MLBB

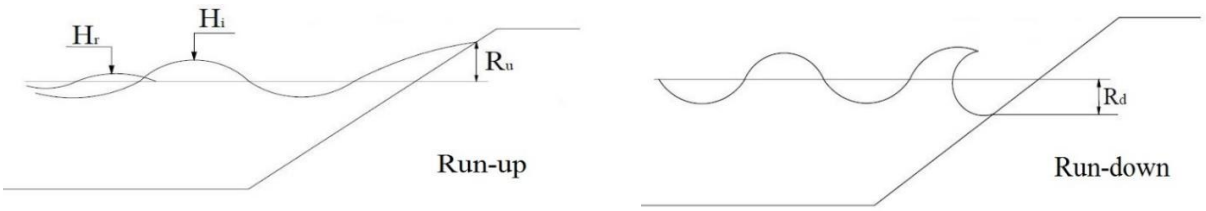

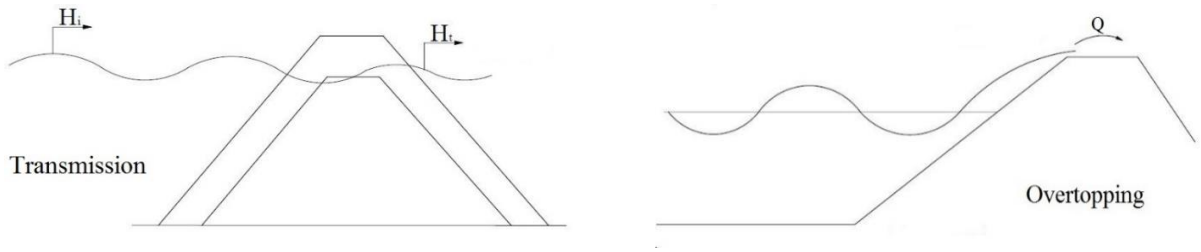

Figure 2. The various governing hydraulic parameters

Battjes' formula [12] in which:

$$C_r = 0.14\xi^{0.73} \quad (3)$$

Commenting on the Iribarren number, Van der Meer [6] argued that it could not explain the effects of both wave steepness and front slope and also, as he mentioned, by means of the multiple regression analysis, a better fit to Postma's data [15] is achievable. Overall, an empirical formula as the following form is derived:

$$C_r = 0.081P^{-0.14}\cot\alpha^{-0.78}S_{op}^{-0.44} \quad (4)$$

where, $S_{op} = \frac{H_s}{gT_p^2/2\pi}$ is the wave steepness, H_s is the incident significant wave height, P is the permeability, and T_p is the peak spectral period. Van der Meer [26] has put forward the structure's permeability, which is made up of the armor size, filter, and core layers from 0.1 for a relatively impervious core (sand or clay) to 0.6 in homogenous structures.

Hughes and Fowler [16] presented a formula to estimate the wave reflection coefficient using the novelty of the Iribarren number concept as follows:

$$C_r = 1/(1+7.1\xi^{0.8}) \qquad (\xi = \sqrt{d/(gT^2\tan\alpha)}) \quad (5)$$

in which d is the water depth, and T is the wave period in regular waves. Buccino et al. [25] developed Hughes and Fowler [16] formula to predict a reflection coefficient formula for sloped coastal structures by taking the advantage of wave momentum flux approach, which was formerly introduced by Melby and Hughes [27]. Chegini et al. [17] studied wave reflection from rubble mound breakwater. The model tests were carried out on two different sections of breakwaters with armor layers of tetrapod units and antifer blocks. They stated that the coefficient of wave reflection increases with increasing the surf-similarity parameter.

Lykke Andersen's [3] study on berm breakwatesr reveals that, as the slope and consequently the surf similarity parameter (ξ) differ, this would make it difficult to find a single value of (ξ) representing the breaking on the structure and also the phase lag between reflections from different parts of the structure. Van der Meer and Sigurdarson's [23] study was conducted on the wave reflection with data being gathered and analyzed from other researchers' investigations. Finally, they proposed the following formulae to estimate the wave reflection coefficient regarding Lykke Andersen's [3] assumptions:

$$C_r = 1.3 - 1.7S_{op}^{0.15}$$

(hardly and partly reshaping berm breakwaters) (6)

$$C_r = 1.8 - 2.65S_{op}^{0.15} \quad (7)$$

(fully reshaping berm breakwaters)

Owing to the unfavorable effects of wave reflection on coastal structures, their designing process lacks a requisite design criterion. A glance through previous studies indicates that there are some empirical predictive formulae merely encompassing the parameters by which the structure's wave reflection was affected. Notwithstanding the major focus of the earlier studies on the wave reflection in conventional rubble mound breakwaters, it has not been given any undivided attention. Moreover, considering the structures in the company of a berm – with higher capability in energy dissipation compared to the conventional type – like MLBBs, the wave reflection value is smaller than the conventional rubble mound breakwaters. Since some berm parameters such as berm elevation from SWL were not taken into account, employing the conventional rubble mound breakwaters formula for the berm breakwaters would lead to considerable uncertainties. Moreover, since MLBBs generally perform as hardly/partly reshaping breakwaters, the wave reflection values are far away from fully reshaping berm breakwaters. It is worth mentioning that due to poor stones extracted from quarries in the south of Iran, conducting a comprehensive study on MLBBs (exploiting the quarry stones optimally) seems to be essential for deeper understanding and future practical cases.

In the present research, a systematic experimental study was undertaken to examine the effect of various parameters on MLBBs wave reflection. To fulfill this task, a 2D experimental modeling in a wave-flume is considered to investigate the effects of wave height, wave period, water depth, and berm elevation, and finally, a proper formula is presented to estimate the wave reflection. The following structure of the study takes the form of six sections, including the experimental set-up, the range of dimensional and

dimensionless parameters, non-dimensional analyses, the effects of various parameters on wave reflection, the procedure of driving the proposed formula for the wave reflection coefficient, and in the final section the present formula is evaluated with the other existing ones.

2. Model test set-up

The present study was conducted in a wave flume in the hydraulic laboratory of the Faculty of Civil Engineering at Tarbiat Modares University equipped with a piston-type wave generator producing irregular waves (Figure 3). All experiments were conducted with irregular waves using a JONSWAP spectrum with a peak enhancement factor γ=3.3. To ultimately gain the definite wave combination, several tests have been repeated over and over again. Regarding the scale modeling, two highly permeable and active rock absorbers were set-up at both ends of the wave flume behind the paddle and also the opposite side to absorb the wave energy and consequently minimize the wave reflection impact on the newly waves generated by the paddle. The wave flume is 16×1×1 *m* (length× width× depth) with fitted glass panels throughout its length, providing convenient observations and filming. The MLBB experimental model consists of four stone classes inspired by the Sirevåg breakwater in Norway. Figure 4 shows the typical cross-section of the breakwater placed at the end of the flume.

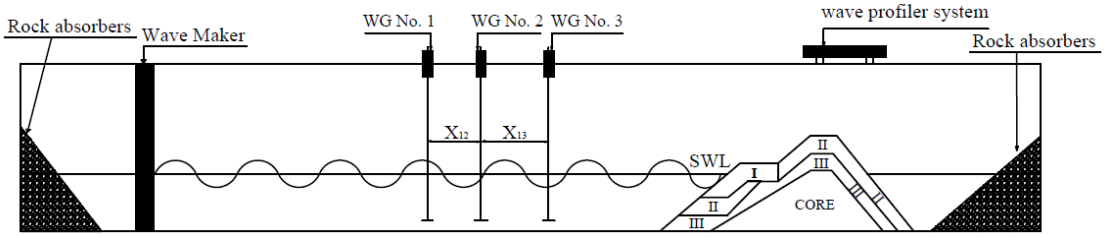

Figure 3. Longitudinal section of the model set-up

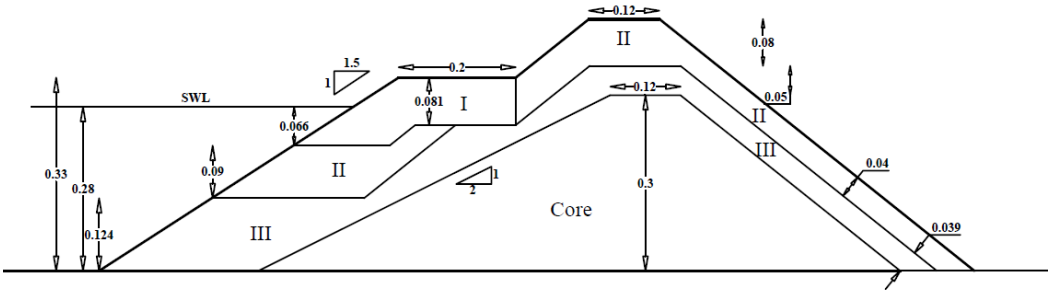

Figure 4. Typical initial cross section of the MLBB

The literature review on reflection analysis reveals that in order to separate incident and reflected wave height, the known methods such as Goda and Suzuki [28] and Mansard and Funke [29] methods are exploited. Goda and Suzuki [28] method employs two wave probes at fixed positions to measure wave heights from both probes and the phase shifts between the two probes. This method fails when the spacing between the two wave probes is equal to an irregular number of half wave-length. In order to reduce the probes spacing problem and the sensitivity to noise, Mansard and Funke [29] proposed a method involving three gauges, which is based on a least-squares technique. In fact, the least-squares method overcomes the limitations of the two-point method, which was initially proposed by Mansard and Funke [29] for irregular waves. In this method, wave heights are measured from three probes aligned parallel to the wave propagation direction, and two groups of phase shifts among these gauges with certain distances apart are also measured. The main references showed that two-point method has limitations, such as limited frequency range, critical gauge positions causing singularity, and sensitivity errors. A least square method (e.g., Mansard and Funke's [29] method) minimizes the squares of errors between measured and theoretical signals. It is less sensitive to these phenomena, and practically there is no limitation in its application range of frequency (or wave-length). Thus, it seems that Mansard and Funke's [29] method indicates greater accuracy and range encompasses your mentioned restriction, and thereby it has been widely hired in many studies pertinent to irregular waves. In the present research, water level fluctuations were recorded with three wave gauges based on Mansard and Funke's [29] pattern by which the incident waves and reflective waves are commonly separated. Wave gauges are a capacitive type with the frequency of 10 *Hz* and the precision of 1 *mm*, recording the water level fluctuations at every 100 milliseconds. As recommended by Mansard and Funke [29] the distance between wave gauges must satisfy the following limits:

$$X_{12} = L/10,\ L/6 \le X_{13} \le L/3,\ X_{13} \ne L/5, 3L/10 \qquad (8)$$

where X_{12} is the distance between the first wave gauge (wavemaker side) and the middle wave gauge, X_{13} is the distance between the first wave gauge and the third wave gauge (breakwater side). A code was written in

MATLAB, separating both reflective and incident waves according to Mansard and Funke's method [29] soon after each test came to an end. Moreover, the main assumption underlying the analysis of reflection in an irregular sea state is that the irregular waves can be described as a linear superposition of an infinite number of discrete components each with their own frequency, amplitude, and phase. The given assumption has been widely accepted as a common fact in studying irregular waves. Due to this fact, these assumptions and Mansard and Funke's [29] method have been used in the present research.

In order to ensure the accuracy of the constructed structure, it was properly recorded using a vertical point gauge in five distinct sections at distances of 0.02 m. The middle section is located in the middle of the flume, and the side sections are located at a distance of 0.15 m from each other. Moreover, throughout choosing the sections, in order to control the effect of walls on test results, the allowable distance from the sections to flume walls has been taken into account. Finally, the average of all five sections is considered as the initial and reshaped profile for further calculations. Table 1 lists the material properties, including the density of the armor, stone nominal diameter, and stone gradation in different layers for all tests. Figure 5 displays a view of the tested MLBB.

Table 1. Material properties at different classes.

	Class I	Class II	Class III	Core
D_{n50} **(m)**	0.027	0.02	0.012	0.005
$f_g=D_{n85}/D_{n15}$	1.2	1.5	1.5	
ρ **(kg/m^3)**	2650	2650	2650	2650

3. Range of dimensional and dimensionless parameters

The present experiments are designed to investigate a variety of parameters such as wave height, wave period, water depth, and berm elevation. The range of dimensional and non-dimensional parameters are given in tables 2 and 3. In this research, a wide range of variations for the dimensionless parameters such as Reynolds number, wave steepness, and surf similarity parameter are considered. For all the conducted tests, as the stability number varied within the range of 1.3-2.3, the structure performed as a partly/hardly reshaping berm breakwater.

Figure 5. A view of the MLBB model

Table 2. Range of dimensional parameters in present experimental

Variable	Range of parameter
Incident significant wave height (H_s)	0.059 to 0.103 (m)
Peak wave period (T_p)	1 to 1.54 (s)
Water depth (d)	0.24 to 0.28 (m)
Berm elevation (h_{br})	0.03 to 0.07 (m)
Berm width (B)	0.2 (m)

Table 3. Range of non-dimensional parameters

Parameter	Range of parameter
N	3000
S_{op}	0.016 to 0.065
$cot\alpha$	1.5
L_o/d	5.57 to 15.4
h_{br}/H_s	0.1 to 1.18
ξ	1.97 to 6.33
R_e	1.82×10^4 to 3.0×10^4

Dai and Kamel [30], Thomsen et al. [31], Broderick and Ahrens [32], Jensen and Klinting [33], Burcharth and Frigaard [34], Van der Meer [26], and Wolters et al. [35] conducted some experimental research on the scale effects, in which the Reynolds number was employed as the following equation to evaluate viscous scale effect in the experimental models of rubble mound breakwaters.

$$R_e = \frac{\sqrt{gH_s}D_{n50}}{\upsilon} \quad (9)$$

where $\sqrt{gH_s}$ is the characteristic velocity, D_{n50} is the characteristic length, and υ is the kinematic viscosity. The viscous scale effect could be neglected since the minimum Reynolds number for current tests is 2×10^4, which is greater than $(1\text{-}4)\times10^4$ recommended by Van der Meer [26].

4. Non-dimensional analysis

Generally, to take the preliminary steps in simulating modelling a physical phenomenon, the decisive factors must be truly recognized. Since the physical

quantities can be defined in terms of dimensions, it is perfectly efficient to utilize a method creating dimensionless parameters with physical principles. One of the initial agents in experimental studying is dimensional analysis. This method would decrease the complexity and number of effective experimental parameters in a physical phenomenon using a compounding technic and therefore propose the dimensionless relations and relevant experimental results. The Buckingham Pi theorem is used as one of the comprehensive theories in dimensional analysis, to determine the dimensionless parameters. Afterwards, by changing the variables during the tests, we can check out their effects on the wave reflection of MLBBs and eventually derive appropriate formulae. Variables describing the sea state, armor units, and the structure geometry are illustrated in Eq. (10).

$$F(H_r, H_i, T_p, d, N, \rho_w, \mu, g, h_{br}, \alpha, B, R_c, G_c) = 0 \quad (10)$$

where ρ_w is the density of water, μ is the dynamic viscosity of the fluid. Supposing a non-overtopped structure, the height of the crest above the mean sea level, R_c, and the width of the crown of the breakwater, G_c, are not important. Also, the front slope angle (α), the berm width (B) and the number of waves (N) are all remained constant in all tests. Hence, Eq. (10) can be reduced as follows:

$$F(H_r, H_s, T_p, d, \rho_w, \mu, g, h_{br}) = 0 \quad (11)$$

Eight variables remained in Eq. (11). By using the Buckingham Pi theorem and compounding method, 5 (=8 − 3) independent dimensionless parameters are obtained as the following equation:

$$\mathrm{X}\left(\frac{H_r}{H_s}, \frac{\rho_w \sqrt{g H_s} H_s}{\mu}, S_o, \frac{L_o}{d}, \frac{h_{br}}{H_s}\right) = 0 \quad (12)$$

The second parameter is the Reynolds number (R_e), which has negligible influence based on the aforementioned discussion, so it is eliminated from Eq. (12). Thus, Eq. (13) can be written as follow:

$$C_r = \Psi\left(S_o, \frac{L_o}{d}, \frac{h_{br}}{H_s}\right) \quad (13)$$

Eq. (13) conveys the fact describing the wave reflection from an MLBB for considered wave conditions and structure's variables.

5. Results and Discussion

As stated earlier, one of the critical issues in studying the functional behaviors of the rubble mound structures is the wave reflection of the breakwaters. In the following section, at first, the effect of different parameters on the MLBB's wave reflection is discussed in accordance with present experimental tests. Afterwards, by analyzing the test results, a new practical formula to estimate the wave reflection is derived for the MLBB. Note that the structure is considered as a non-overtopped breakwater all through the tests.

5.1. Effect of wave height on the wave reflection

In the current study, the effect of wave height on wave reflection for four disparate wave heights (H_s = 0.059, 0.0745, 0.09, and 0.103 *m*) is investigated. As a point to note, the water depth, the berm elevation, and the wave number are constant values of 0.28 m, 0.05 m, and 3000 waves, respectively. Figure 6 indicates the influence of wave height on wave reflection in four disparate wave periods.

Figure 6 pinpoints the marginal effect of wave height on wave reflection coefficient. The observed smooth decrease in the wave reflection coefficient could be attributed to an increase in some of the given data wave height. As a reason for the mentioned behavior, Postma [15] stated that energy dissipation along the slope is due to the existing drag forces. These forces are directly increased with the square of the local wave-particle velocities, which in turn increase as wave height increase. As another pertinent study to this case, Muttray et al. [18] expressed the effect of wave breaking and permeability, which are respectively defined by a decrease and an increase in wave reflection coefficient in the presence of raised wave height, are approximately balanced. Thus, the reflection coefficient is approximately independent of wave height.

5.2. Effect of wave period on the wave reflection

Throughout this section, the influence of the wave period on the wave reflection of the MLBB is investigated in four different wave periods (T_p=1, 1.18, 1.36, and 1.54 s) with the same heights. The water depth (d= 0.28 m), the berm elevation (h_{br}= 0.05 m), and the wave number (N= 3000) are constant during all wave periods tests. Figure 7 plots the wave reflection coefficient versus the wave period for several values of wave heights. Figure 7 highlights the supreme importance of the wave period, owing to a remarkable increase in wave reflection coefficient. This result has also been concluded by other researchers such as Scheffer and Kohlhass [36].

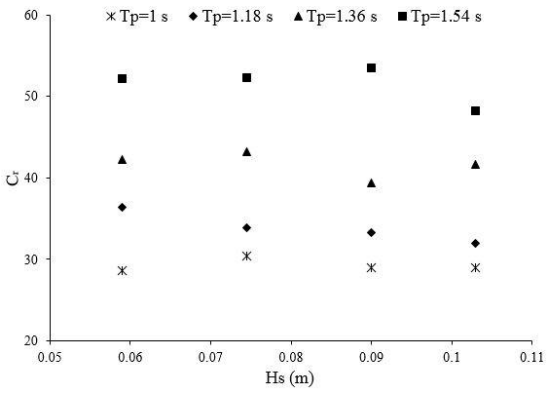

Figure 6. Influence of wave height on wave reflection coefficient for disparate wave periods

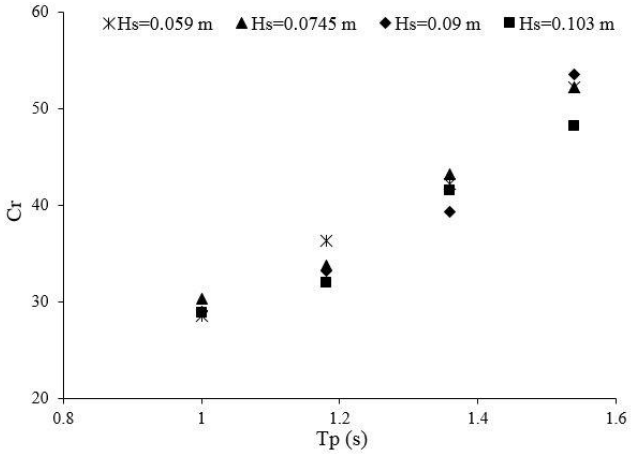

Figure 7. Influence of wave period on wave reflection coefficient for different wave heights

5.3. Effect of berm elevation on the wave reflection

A glance through the recent research on wave reflection discloses that nearly several studies were exclusively aimed at the conventional rubble mound structures, in which berm structural parameters such as the berm elevation were not considered. However, in this paper, 12 tests were carried out to investigate the effect of the berm elevation on the wave reflection of an MLBB constructed with three different berm elevations (h_{br}= 0.03, 0.05, and 0.07 *m*) for different wave combinations. It is noteworthy to state that all through the tests probing into the effect of berm elevation on MLBBs' wave reflection, other effective parameters such as water depth, the height of class I must be constant, while the berm elevation from the structure's toe is changed from the lower levels by adding or removing stone classes II or III [37].

Figure 8 depicts the influence of berm elevation on the wave reflection coefficient for different wave combinations. As it is shown, by increasing the berm elevation, the value of the wave reflection coefficient will rise. It can be concluded from observations that at the SWL close to the berm level, the waves in the process of run-up were distributed widely on the porous berm and even the upper slope of the berm resulting in higher wave energy dissipation. Consequently, by increasing dissipation, the wave reflection of the structure will be reduced. However, in the higher berm elevation from SWL, the berm performs inefficiently in wave energy dissipation. In the case in fact, the MLBB acts as a porous obstacle against the wave attack similar to conventional rubble mound breakwaters and leads to a higher wave reflection. Ehsani et al. [38] meticulously investigated the case of how the berm elevation can affect the wave energy dissipation in MLBBs.

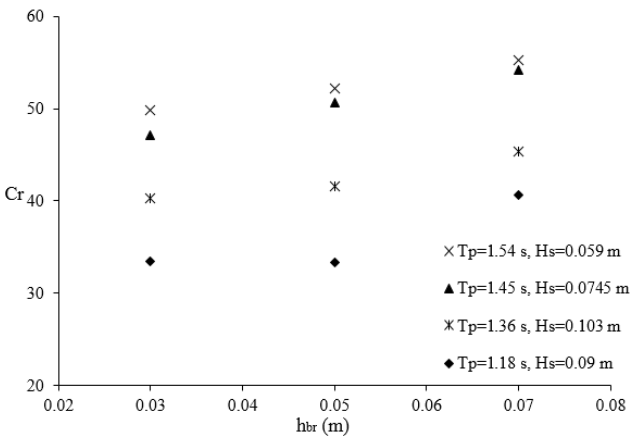

Figure 8. Influence of berm elevation on wave reflection coefficient for different wave combinations

5.4. Effect of water depth on the wave reflection

Reviewing the literature concerns the effect of water depth on the wave reflection of the rubble mound breakwaters depicts that this parameter affects the structure's wave reflection. In order to obtain reasonable and accurate results in an experimental study of water depth in berm breakwaters, two particular points must be noted:

1- In the case of maximum water depth at the toe of the structure, the breakwater should behave as a non-overtopped structure.
2- The height of stone class I and berm elevation from still water level must be kept constant as the water depth changes.

Over this investigation, the effect of water depth on the wave reflection of the MLBB has been examined at three different water depths (*d*= 0.24, 0.26 and 0.28 *m*). Pre-tests were also conducted to control the breakwater performing as a non-overtopping structure. It is worth to note that in order to examine the effect of the water depth, the berm elevation from SWL must be maintained constant (i.e. h_{br} =0.05 *m*). It is apparent from Figure 9 -illustrating the influence of the water depth on the wave reflection coefficient- that an increase in water depth corresponds to the decrease in the wave reflection coefficient.

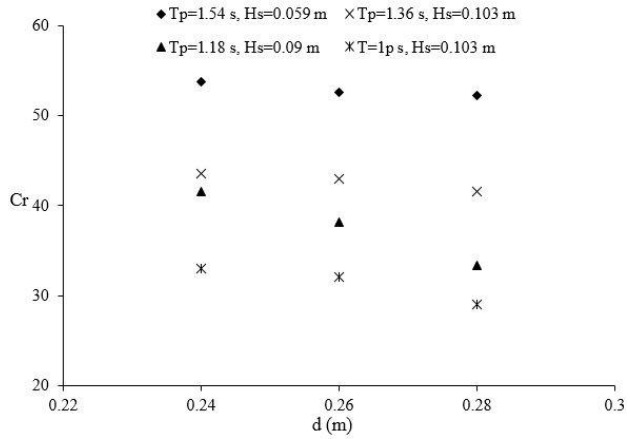

Figure 9. Influence of water depth on wave reflection coefficient for different wave combinations

6. The formula derivation methodology

So far, many reflection formulae have been proposed as a function of the Iribarren number. If the front slope is assumed as a constant parameter in the Iribarren number, the wave steepness can be defined as an effective parameter. Figure 10 displays the effect of the wave steepness against the wave reflection coefficient.

Figure 10 denotes a fairly high scattering in the data set, and the trend reveals that an increase in the wave steepness causes a decrease in the wave reflection coefficient. Based on the aforementioned discussion, an independent wave height approach should be utilized, in which the following dispersion equation is firstly taken into account:

$$\sigma^2 = gk\,tgh(kd) \tag{14}$$

where k is the wave number ($K=2\pi/L$), and σ is the angular frequency of the wave. The dispersion equation expresses that the wave number and the angular frequency of the wave are not independent. On the other hand, the dispersion equation justifies the relativity of the wave length, the wave period, and the water depth. According to the stated interpretation, wave reflection can be defined as a function of kd or L_o/d. Moreover, Muttray et al. [18] assumed that wave reflection is a function of T^2/d. Since the dimension of L_o is length, it is highly appropriate to express the effect of wave period by means of a parameter with length dimension such as L_o. Thus, in the present study, L_o/d is used as a non-dimensional parameter. As detailed in Figure 11 illustrating the wave reflection coefficient versus L_o/d, C_r has a considerable reliance on L. In order to scrutinize the effect of L_o/d on the wave reflection, several algebraic functions are employed, and finally, the power function is chosen as follows:

$$C_r = \lambda(L_o/d)^{\eta} \tag{15}$$

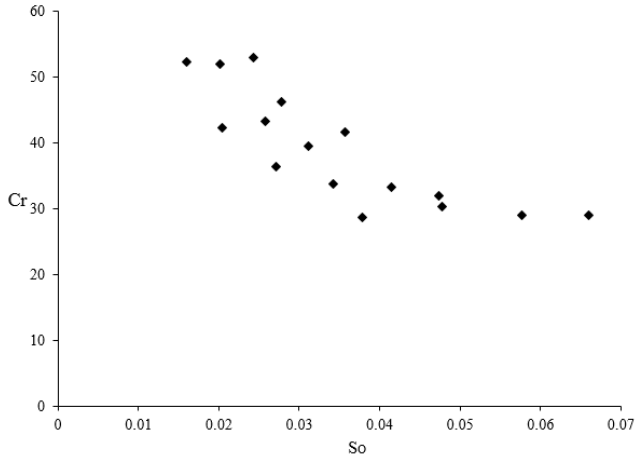

Figure 10. Influence of the wave steepness versus the wave reflection coefficient

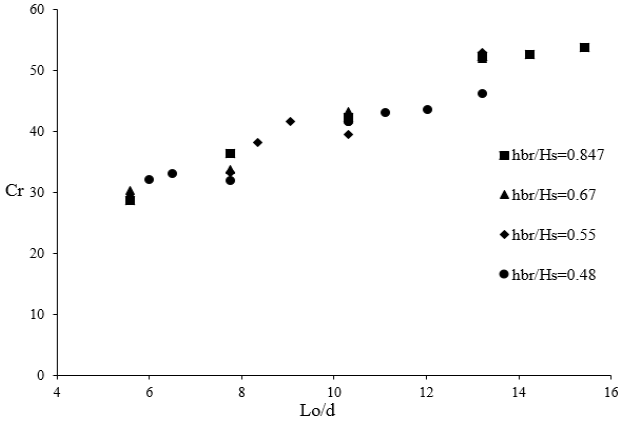

Figure 11. Variation of L_o/d versus C_r

To find the coefficients λ and η - denoting the shape and the curve trend- a nonlinear regression is used for each combination of h_{br}/H_s. Due to the same trend variations of the wave reflection coefficient in discrete h_{br}/H_s, this coefficient has small discrepancies, so an average value of η=0.5 is used in the final equation. Note that the value of λ is a function of h_{br}/H_s. Eventually, a suitable pattern considering the effect of L_o/d on wave reflection coefficient will be used as follows:

$$C_r = \lambda(L_o/d)^{0.6} \qquad \lambda = f(h_{br}/H_s) \tag{16}$$

Trying to predict the value of the variable $f(h_{br}/H_s)$, Eq. (16) is rewritten as the following equation:

$$f(h_{br}/H_s) = \frac{C_r}{(L_o/d)^{0.6}} \tag{17}$$

In order to determine the value of $f(h_{br}/H_s)$, the right side of Eq. (17) against the corresponding h_{br}/H_s is plotted in Figure 12.

To gain a proper estimation function of the variables $f(h_{br}/H_s)$, several algebraic functions are examined. Ultimately, the power function for the present experimental data is proposed as an appropriate model. By employing regression analysis, the new formula can be written to predict the wave reflection coefficient for MLBB as follows:

$$C_r = 11.21(h_{br}/H_s)^{0.12}(L_o/d)^{0.6} \tag{18}$$

Following the present experimental work limitations, the range of measured values are as Eq. (19), and therefore, the new formula is valid for this range.

$$\begin{cases} S_o = 0.016 - 0.065 \\ \xi = 1.97 - 6.33 \\ h_{br}/H_s = 0.29 - 1.18 \\ L_o/d = 5.57 - 15.4 \\ \cot\alpha = 1.5 \end{cases} \tag{19}$$

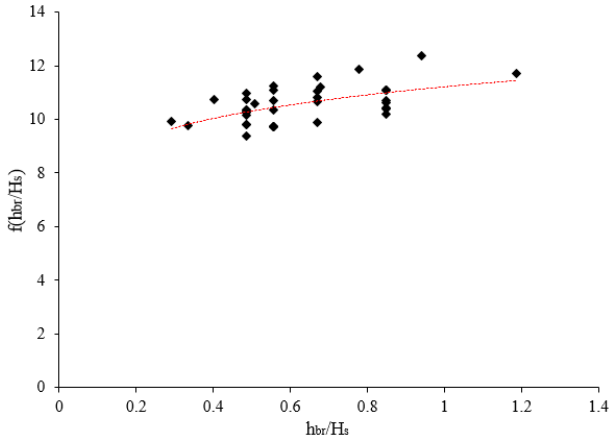

Figure 12. Variation of h_{br}/H_s versus $f(h_{br}/H_s)$ by using the present experimental data

7. Validity assessment of the present formula with other researcher's formula

Statistical validation indices are hired to validate the performance of the new formula and other researcher's formulae. To fulfill this achievement, the present formula is compared to other formulae such as Postma [15] and Hughes and Fowler [16] based on the present experimental data. In order to evaluate the efficiency of various methods, different validation indices such as the square of the correlation factor (R^2), the normalized root mean square error (NRMSE), and Bias are employed as follow:

$$R^2 = 100\left(\frac{N\sum XY - (\sum X)(\sum Y)}{\sqrt{\left[N\sum X^2 - (\sum X)^2\right]\left[N\sum Y^2 - (\sum Y)^2\right]}}\right)^2$$
$$NRMSE = \sqrt{\frac{\sum (Y - X)^2}{\sum (Y - \bar{Y})^2}} \qquad (20)$$
$$BIAS = \bar{X} - \bar{Y}$$

where X is the calculated value, $\bar{X}$ is the average value for the calculated data, Y is the observation data, $\bar{Y}$ is the average value for the observation data, and N is the total data.

On the basis of present experimental data, table 4 tabulates the value of the evaluation indices and demonstrates that the present formula efficiently predicts the wave reflection coefficient rather than the other formulae. It is worth noting that the value of negative Bias in table 4 shows different methods underestimating the wave reflection coefficient.

Table 4. Validation indices for available formulae on wave reflection coefficient with present experimental data

	Postma [15]	Hughes and Fowler [16]	Present formula
R^2 (%)	77.6	89.6	93.7
NRMSE	0.71	0.8	0.25
Bias	-4.26	-3.4	-0.1

Furthermore, it could be drawn that the other researcher's formulae show a relatively high scattering, which could be attributed to disregarding some effective parameters such as the water depth at structure's toe. In addition to the given regard, it is worth mentioning that the methods extended by Hughes and Fowler [16] were only unique to statically straight slopes without a berm. However, as we mentioned earlier, the berm elevation from SWL is known as a remarkably effective parameter on the wave reflection.

More details on validation are given in this section by using the rest of the present experimental data to provide an efficient comparison between the proposed equation and existing ones, such as Postma [15] and Hughes and Fowler [16]. It is remarkable to note that to make a fair comparison, the mentioned experimental data is not exploited in the new formula (Eq. (18)) derivation. Figure 14 depicts the comparison of measured and predicted wave reflection coefficient based on the aforementioned methods. It is easily observed that the proposed wave reflection formula matches perfectly with the current data and illustrates less error in contrast with other formulae results. Thus, considering some parameters such as berm elevation and water depth would obviously explain why there has been less error in the proposed formula, which performs independently from the wave height. It is necessary to point out that Postma [15] and Hughes and Fowler [16] methods investigated conventional rubble mound breakwaters. Thereby, the low accuracy of the other researcher's formulae could be justified by some effective parameters that were disregarded in their formulae. To estimate the capability of the new formula in contrast with the existing ones, the verification indices for the given formulae are evaluated. Table 5 shows the validation indices for different formulae.

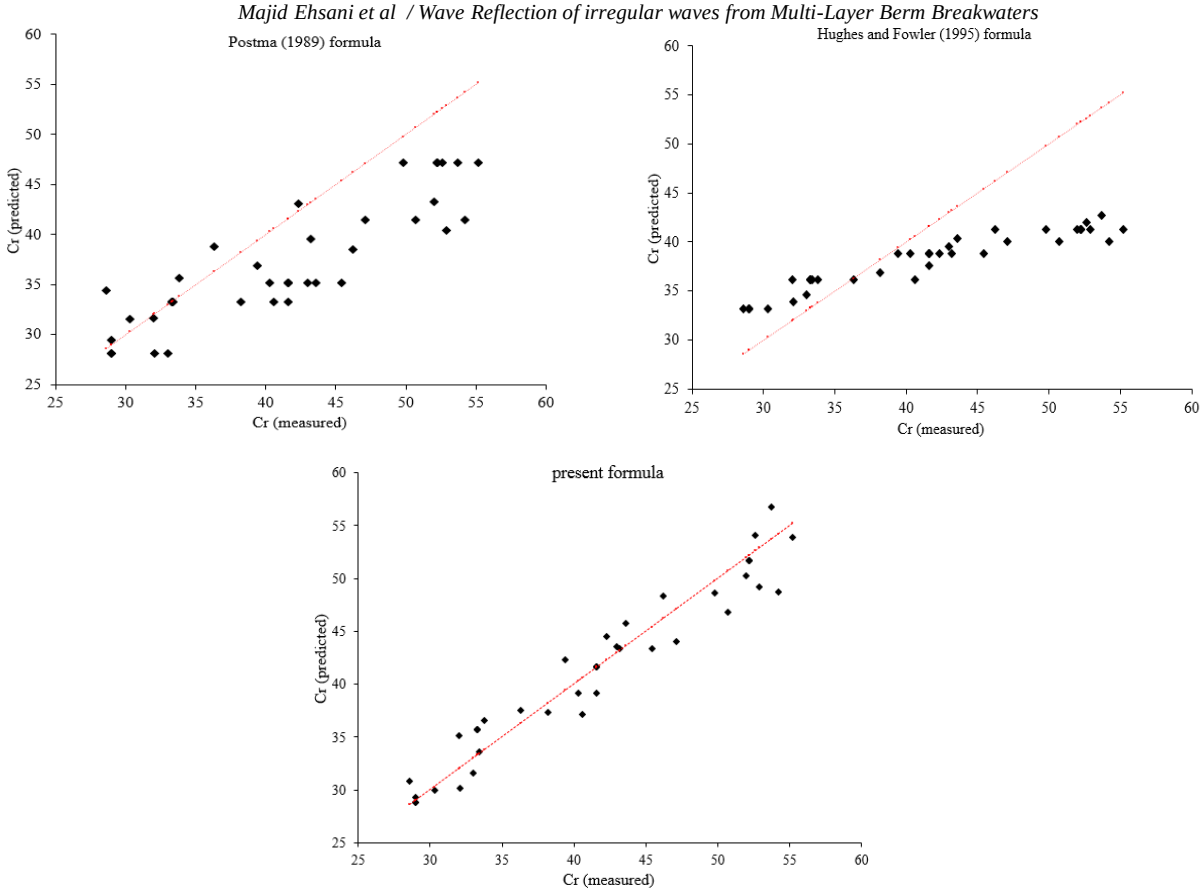

Figure 13. Comparison of measured and calculated wave reflection coefficient for present data for various formulae

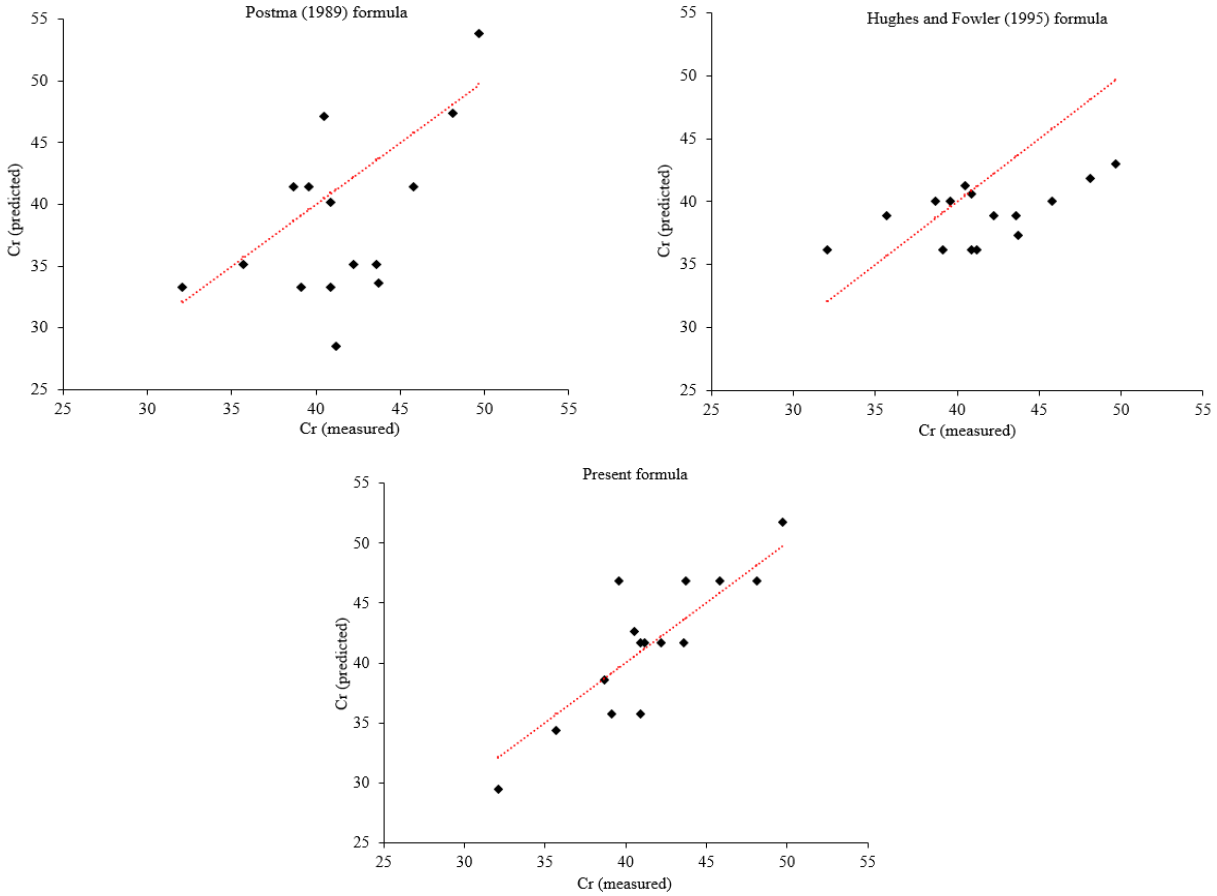

Figure 14. Comparison of measured and predicted wave reflection coefficient based on MLBB data for various formulae

Table 5. Validation indices for available formulae on wave reflection coefficient with MLBB experimental data

	Postma [15]	Hughes and Fowler [16]	Present formula
R^2 (%)	31.4	33.2	75.9
NRMSE	1.42	0.99	0.67
Bias	-2.76	-2.42	0.04

In the following, the given formula estimating the wave reflection coefficient and other existing ones have been evaluated using Sveinbjörnsson's [39] data set for a multi-layer structure. It is worthy to note that Sveinbjörnsson's [39] study was conducted under 3000 number of waves and an armor slope of 1:1.5. Table 6 provides a comparison between the statistical evaluation of indexes in estimating wave reflection for Sveinbjörnsson's [39] data set regarding our outcomes using Eq. (18) and other existing formulae. Moreover, as given in Fig. 15, the measured and calculated values of the wave reflection coefficient using the present formula have been compared to other researcher's formula for Sveinbjörnsson's [39] data set. One can conclude from the outcomes that our formula performs more appropriately than other proposed formulae. It should be noted here that all other proposed formulae are unique to homogenous armored rubble mound breakwaters, while the present formula estimates the wave reflection for multi-layer armored breakwaters. As one can observe from the BIAS index, in comparison with average measured values, the calculated values using other researcher's formula are overestimated. For instance, the BIAS parameter from Eq. (4) is equal to (6.16), and through the use of Eq. (5), it would be (4.69).

Table 6. Validation indices for available formulae on wave reflection coefficient with Sveinbjörnsson's (39) data set for a multi-layer structure

	Postma [14]	Hughes and Fowler [15]	Present formula
R^2 (%)	13.6	37	82.5
NRMSE	2.47	3.91	0.49
Bias	6.16	4.69	-0.61

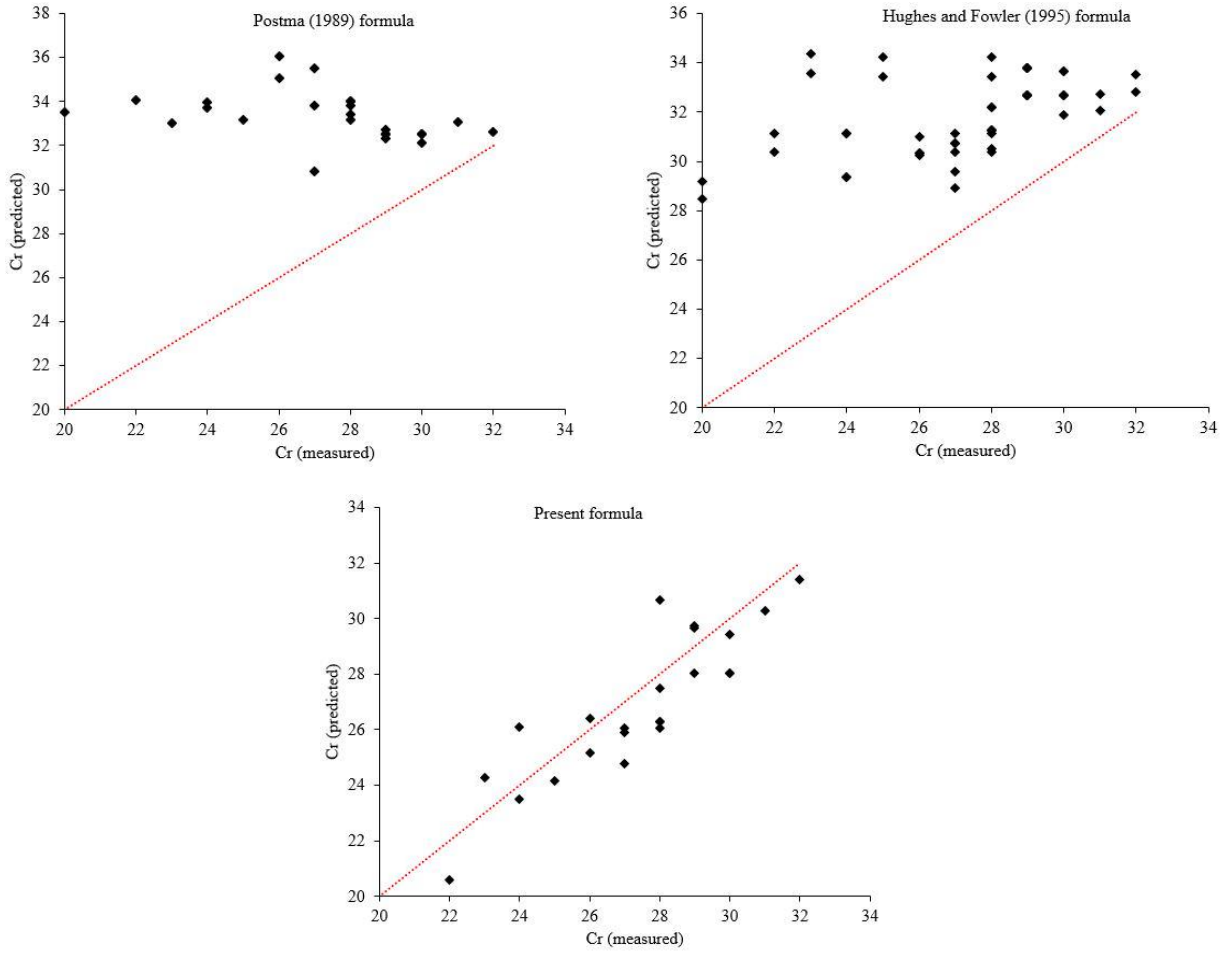

Figure 15. Comparison of measured and predicted wave reflection coefficient based on Sveinbjörnsson's (2008) data set for various formulae

8. Conclusions

This paper has sought to investigate the wave reflection of the MLBBs based on an experimental study and also examined the influence of different parameters including wave height, wave period, water depth, and berm elevation. Our work has led us to draw the given conclusion:

1- It has been noticed that there is no significant difference in the wave reflection coefficient with respect to different wave heights.
2- Variations in the wave period have a principal effect on the wave reflection coefficient so that as the wave period increases, the wave reflection coefficient would be considerably increased.
3- A novel formula (Eq. (18)) encompassing a wide range of non-dimensional parameters is derived to estimate the wave reflection coefficient of MLBBs.
4- The overwhelming advantage of the new equation compared to the other existing methods has been found to be due to its derivation on the basis of an independent wave height approach.

It should be highlighted that since the effect of water depth and berm elevation are both included in the present formula, it would perform more appropriately compared to other existing ones, at least for hardly/partly reshaping breakwaters. The conclusions from this equation indicate a more precise estimation rather than the other formula for predicting the wave reflection coefficient, at least for the MLBBs experimental data.

Acknowledgements

The authors wish to express their sincere gratitude to Iran National Science Foundation (INSF) and Isfahan University of Technology, who contributed financially to the project and the Tarbiat Modares University in Iran for providing experimental facilities.

9. References

1- Moghim, M.N. and Lykke Andersen, T., (2015), *Armor stability of hardly (or partly) reshaping berm breakwaters*, Coastal Engineering, Vol. 104, p.1-12.
2- Ehsani, M., Moghim, M.N. and Shafieefar, M., (2017), *The latest researches and accomplishments in the design rules of Icelandic berm breakwaters*, 16th Iranian Hydraulic Conference, Ardabil, Iran. (In Persian)
3- Lykke Andersen, T., (2006), *Hydraulic Response of Rubble Mound Breakwaters. Scale Effects – Berm Breakwaters*. PhD Thesis, Aalborg University.
4- Tørum, A., Moghim, M.N., Westeng, K., Hidayati, N. and Arntsen, Ø.A., (2012). *On Berm Breakwaters: Recession, Crown Wall Wave Forces, Reliability*, Coastal Engineering. Vol. 60, p.299–318.
5- Sigurdarson, S., Viggosson, G., Benediktsson, S. and Smarason, O.B., (1996), *Berm breakwaters, tailor-made size graded structures*, 11th International Harbour Congress, Antwerp, Belgium.
6- Van der Meer, J.W., (1995), *Conceptual design of rubble mound breakwaters*, In Advances in Coastal and Ocean Engineering, Vol. 1, p.221-315.
7- Chang, H.K. and Hsu, T.W., (2003), *A two-point method for estimating wave reflection over a sloping beach*. Ocean engineering, Vol. 30(14), p.1833-1847.
8- Davidson, M.A., Bird, P.A.D., Bullock, G.N. and Huntley, D.A., (1996), *A new non-dimensional number for the analysis of wave reflection from rubble mound breakwaters*. Coastal Engineering, Vol. 28, p.93–120.
9- Zanuttigh, B., Van der Meer, J.W., Lykke Andersen, T., Lara, J.L. and Losada, I.J., (2008), *Analysis of wave reflection from structures with berms through an extensive database and 2DV numerical modelling*. Coastal Engineering ICCE, Hamburg, Germany.
10- Zanuttigh, B. and Lykke Andersen, T., (2010), *Wave reflection in 3D conditions*, Coastal Engineering, Vol. 57, p.531–538.
11- Miche, R., (1951), *Le pouvoir réphléchissant des ouvrages maritimes exposés à l'action de la houle. Annales de Ponts et Chaussées*, 121è Année, p.285–319. (In French)
12- Battjes, J. A., (1974), *Surf Similarity*, 14th International Conference on Coastal Engineering, Copenhagen, Denmark.
13- Losada, M.A. and Gimenez-Curto, L.A., (1979), *The joint effect of the wave height and period on the stability of rubble mound breakwaters using Iribarren's number*, Coastal Engineering, Vol. 3, p.77–96.
14- Seelig, W.N. and Ahrens, J.P., (1981), *Estimation of wave reflection and energy dissipation coefficients for beaches, revetments and breakwaters*, Coastal Engineering Research Center Fort Belvoir VA, (No. CERC-TP-81-1).
15- Postma, G.M., (1989), *Wave reflection from rock slopes under random wave attacks*, Master Thesis. Delft University of Technology.
16- Hughes, S.A. and Fowler, J.E., (1995), *Estimating wave-induced kinematics at sloping structures*, Journal of waterway, port, coastal, and ocean engineering, Vol.121(4), p.209–215.
17- Chegini, V., Aghtouman, P. and Saghri, N., (2000), *Wave Reflection from Rubble-Mound Breakwaters*. 4th International conference on coasts, ports and marine structures, Tehran.
18- Muttray, M., Oumeraci, H. and Ten Oever, E., (2006), *Wave reflection and wave run-up at rubble mound breakwaters*, Coastal Engineering, ICCE, San Diego, California.
19- Zanuttigh, B. and Van der Meer, J.W., (2006), *Wave reflection from coastal structures*, Coastal Engineering ICCE, San Diego.

20- Zanuttigh, B. and Van der Meer, J.W., (2008), *Wave reflection from coastal structures in design conditions*, Coastal Engineering, Vol.55, p.771–779.
21- Calabrese, M., Di Pace, P. and Buccino, M., (2008), *Wave Reflection at Low Crested Breakwaters Ranging from Submerged to Exposed*, 31th International Conference on Coastal Engineering, Hamburg, Germany.
22- Park, O.Y., Dodaran, A.A., Bagheri, P., Kang, K.U. and Park, S.K., (2013), *Reflection and Transmission Coefficients for Rubble Mound Breakwaters in Busan Yacht Harbor*. Journal of Ocean Engineering and Technology, Vol. 27(6), p.90-94.
23- Van der Meer, J.W. and Sigurdarson, S., (2016), *Design and Construction of Berm Breakwaters*, World Scientific Publishing Co. Pte. Ltd.
24- Mahmoudi, A., Hakimzadeh, H., Ketabdari, M.J., Cartwright, N. and Vaghefi, M., (2017), *Experimental Study on Wave Transmission and Reflection at Impermeable Submerged Breakwaters*. International Journal of Coastal and Offshore Engineering, Vol. 1(3), p.19-27.
25- Buccino, M., D'Anna, M. and Calabrese, M., (2018), *A study of wave reflection based on the maximum wave momentum flux approach*, Coastal Engineering Journal, Vol. 60, p.1-21.
26- Van der Meer, J.W., (1988), *Rock slopes and gravel beaches under wave attack*, PhD Thesis. Delft University of Technology.
27- Melby, J.A. and Hughes, S.A., (2003), *Armor stability based on wave momentum flux*, Coastal Structures Conference, ASCE, New York.
28- Goda, Y. and Yasumasa, S., (1976). *Estimation of Incident and Reflected Waves in Random Wave Experiments*, 15th Coastal Engineering Conference, Honolulu, Hawaii.
29- Mansard, E.P.D. and Funke, E.R., (1980), *The measurement of incident and reflected spectra using a least squares method*, 17th Coastal Engineering Conference, Sydney, Australia.
30- Dai, Y.B. and Kamel, A.M., (1969), *Scale Effect Tests for Rubble Mound Breakwaters*, U. S. Army Engineer Waterway Experiment Station, Corps of Engineers, Vicksburg, Mississippi, Research Report H-69-2.
31- Thomsen, A.L., Wohlt, P.E. and Harrison, A.S., (1972), *Riprap Stability on Earth Embankments Tested in Large-and Small-Scale Wave Tanks*, CERC Technical Memorandum No. 37, U.S. Army Corps of Engineers.
32- Broderick, L.L. and Ahrens, J.P., (1982), *Riprap Stability Scale Effects*, CERC Technical Paper 82-3, U.S. Army Corps of Engineers.
33- Jensen, O.J. and Klinting, P., (1983), *Evaluation of scale effects in hydraulic models by analysis of laminar and turbulent flow*, Coastal Engineering, Vol.7, p.319–329.
34- Burcharth, H.F. and Frigaard, P., (1987), *On the Stability of Berm Breakwater Roundheads and Trunk Erosion in Oblique Waves, In Berm Breakwaters*, workshop at NRC, Canada, Ottawa, ASCE.
35- Wolters, G., van Gent, M., Allsop, W., Hamm, L. and Muhlestein, D., (2010), *HYDRALAB III: Guidelines for physical, model testing of rubble mound breakwaters*, 9th international conference organized by the Institution of Civil Engineers and held in Edinburgh.
36- Scheffer, H.J. and Kohlhase, S., (1986), *Reflection of irregular waves at partially reflective structures including oblique wave approach*, 20th Conference on Coastal Engineering, Taipei, Taiwan.
37- Ehsani, M., Moghim, M.N., and Shafieefar, M., (2019), *The effect of stone class I characteristics on hydraulic stability of multilayer berm breakwaters*, Journal of Marine Engineering, Vol. 15(30), p.53-67.
38- Ehsani, M., Moghim, M.N., and Shafieefar, M., (2020), *An experimental study on the hydraulic stability of Icelandic-type berm breakwaters*, Coastal Engineering, Vol.156, 103599.
39- Sveinbjörnsson, P.I., (2008), *Stability of Icelandic type berm breakwaters*, Master Thesis. Delft University of Technology.

INTERNATIONAL JOURNAL OF
COASTAL & OFFSHORE ENGINEERING
IJCOE Vol.5/No. 1/Spring 2020 (25-30)

Available online at: www. Ijcoe.org

Field data measurement in confluence of the Arvand and the Karun Rivers focusing on sediment, tidal and CTD study

Rouhollah Amirabadi[1], Ahmad Rezaee Mazyak[2], Ali Ghasemi[3*], Mohammadreza Khosravi[4]

[1]*Assistant Professor, Civil Engineering Department, Faculty of Engineering, University of Qom;* r.amirabadi@qom.ac.ir
[2]*Ph.D. student, Faculty of Civil and Environmental Engineering, TMU;* a.rezaeemazyak@modares.ac.ir
[3*] *PhD Student, Marine Structure Group, Faculty of Engineering, University of Qom;* ghasemi.ali89@gmail.com
[4] *MSc in Coastal, Harbor and Marine Structure, Pars Geometry Consultant;* mohammad.r.khosravi@gmail.com

ARTICLE INFO

Article History:
Received: 31 May. 2020
Accepted: 21 Oct. 2020

Keywords:
The Arvand River
The Karun River
CTD
Tidal Current
Sediment, Field data

ABSTRACT

The Karun River is considered to be the longest Iranian river with 855 km length. The river is divided into two branches, 4 km away from the Arvand River, which is a branch of the Bahmanshir River in the north of Abadan, and another branch of the Namkarun River (the Azodi Channel) that flows into the Arvand River. The intersection of the Karun River and the Arvand River is important. Also, measuring and investigating of hydrodynamic phenomena have a vital role in recognizing and prediction the hydrodynamic changes in the region. Therefore, CTD and hydrographic studies were carried out for the Azodi Channel, which is the intersection of the Karun River and the Arvand River. These studies include measurements of marine phenomena such as tidal observations, water level changes, hydrography, topography, CTD and sedimentation. Studies have shown that floods of the Karun River have caused significant changes in the intersection of the rivers Karun and Arvand. Also, the sediment of the study area is fine-grained, but at the intersection of the rivers Arvand and Karun, it is coarse-grained. Sediment concentration is increased in depth, and the lowest and highest sediment concentrations are related to Karun station and Arvand Karun intersection respectively. Regarding the alignment survey, it was found that the current of the study area is mixed current, but mostly meridian. The flow of the Karun River is one of the parameters affecting the water level. So that if the current of the river is noticeable, it will prevent the tidal wave from spreading into the river.

1. Introduction

Karun, which is the longest river in Iran with a length of 855 km, is 180 km long from Khorramshahr to Ahvaz and is called Karun Sofla. This river is divided into two branches. One of them is Bahmanshir branch in the north of Abadan which runs parallel to Arvand and joins the Persian Gulf, and the other branch is Azodi canal which flows in the south of Khorramshahr and flows into Arvand. The Arvand River forms part of the Iran-Iraq border, joining the Tigris and Euphrates rivers in Iraq and joining the Karun River. The intersection of the Karun and Arvand rivers is of special strategic, economic, commercial and political importance due to the existence of various ports and shipbuilding complexes, as well as being located at the border point.

Investigating and studying coastal changes under the influence of hydrodynamic phenomena such as tides, sediment transportation, and salinity changes requires a deep understanding of these phenomena. Predicting and carefully examining the changes in these phenomena will play a significant role in reducing the costs and sustainability of the constructed structures. According to the importance of the study area, some researches have been done which mention below. Ajabpour examined the changes in direction and flow velocity at the confluence of the Arvand River and Karun. In this study, quantities such as water level changes, flow velocity, temperature, salinity, and water depth during a complete tidal period were measured. Studies show that the average flow of water in neap-spring period is towards the sea [1]. Sarvestani and Sadri Nasab studied the structure of a plum at the

entrance to the Arvand River in the Persian Gulf, which is an inverted estuary. In this study four tidal components including H2, S2, K1, and O1 used. The results showed that Plum went to the left at the entrance of the Arvand River and turned to the right due to Coriolis force, creating an anticyclone rotation in the northwestern part of the Gulf and a floating coastal current around Qatar and Saudi Arabia [2]. Etemad Shahidi et al. examined the influence of saltwater due to the increase in seawater level in Bahmanshir. The results showed that sea levels increased from 30 to 90 cm in 2100, and the duration of salinity infiltration increased inversely with discharge and directly with increasing sea level [3]. Khosravi et al. presented the results of Karun river field measurements during one month in spring, 2013. The results indicated that the maximum measured current by a current-meter was 70.6 cm/s, in a seaward direction, and unexpectedly corresponded with the neap tide. The high river discharges concurrently with the neap tide, cause this maximum velocity [4].

As studies have shown, the confluence of the Karun and Arvand rivers is important. Also, the measuring and study of hydrodynamic phenomena will play a very important role in recognizing and predicting hydrodynamic changes in the region. Therefore, measuring the flow parameters and hydrography survey was performed for the Azodi Canal. Studies include measuring marine phenomena such as one-month tidal observations, water level changes, hydrography, flow metering, and sedimentation granulation. In this paper, the parameters measured in the connection range of Karun and Arvand rivers are presented.

2. Methodology and Measuring

Parameters such as salinity, temperature, flow velocity, and water level changes were measured at four stations (1 station on the Karun River and 3 stations on the Arvand River) for four days. The location of the measurement stations shows in Figure 1 and descriptions of measuring present in Table 1.

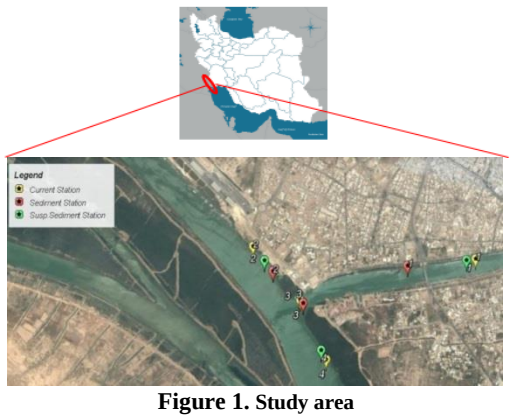

Figure 1. Study area

Table 1. Descriptions of measuring stations

Type of Station	No. Station	Location X	Location Y	Me. conditions	Me. Parameters
Current	1	229295.78	3370041.1	Measuring of parameters 13h/day, 4 days, from depth 0.1, 0.5 and 0.9	Salinity, Temperature, Velocity etc.
	2	227160.38	3369906.5		
	3	227667.17	3369471.6		
	4	227972.13	3368974.9		
Sediment	1	228654	3369903	The weight of samples is 5 Kg	Grading of samples
	2	227378	3369702		
	3	227699	3369448		
	4	227858			
Suspended Sediment	1	229209	3370018	Sampling from depths of 0.1, 0.5 and 0.9 meters	Weight of suspended sediment
	2	227285	3369789		
	3	227653	3369489		
	4	227917	3369050		

The specifications of the measuring devices are given in Table 2.

Table 2. Specifications of the measuring devices

Row	Equipment	Model	Measurement parameters
1	Tide Gage	RBR	Tide
2	Echo sounder/built on DGPS	CEEDUCER/Hemisphere	Positioning Echo sounding
3	Current Meter	Sea & Sun	Speed & Direction Current
4	GPS Dual frequency	Boif M85	Positioning
5	Grap	Metal	Sea bed
6	Water Sampler	Neskin	Water
7	Lap Top	HP	Hypack
8	Handy GPS	Garmin	Positioning
9	Theodolite	Nikon	Vertical Datum
10	CTD	EC Meter	Salinity, Temperature, Conductivity

3. Results and Discussion

In this section, the measured data analyzed. Hydrographic analysis, sediment sampling, water level changes, and flow velocity are the most important results of this section. Analysis and explanation of the field data provide an overview of the physical processes.

3.1. Hydrography

Examining the depth changes in different parts of the study area can determine the approximate pattern of the dominant flow. Therefore, in the first step, hydrography has been studied in the study area. A very deep area has developed at the confluence of the Arvand and Karun rivers. These hydrographic changes show flood currents in Karun that act like water jets. It due to the Om al-Rasas Island is located in front of the exit jet from the mouth of Karun; this island will be like

a compression plate in front of the exit stream and will cause the formation of a wall jet.

Previous studies in the area have shown the process of river formation at the confluence of rivers, leading to drastic morphological changes in the area. Gohari and Amraei showed that sedimentation will occur in the flow separation area and erosion within the maximum current velocity [5]. This is in line with the sedimentation pattern at the confluence of the Arvand and Karun rivers. Therefore, one of the issues that should be considered in the analysis of this area is the flood currents of Karun, which can cause significant changes in the bed of the intersection of Karun and Arvand rivers.

3.2. Sediment Sampling

Sediment sampling includes sampling of riverbeds and suspended sediments. Table 3 and Figure 2 show the results of bed sediment sampling. Most of the sediments in the study area are fine-grained. Therefore the grading of sediments has been done with laser. Evaluation of the results shows that the volume of sand materials at stations in the Karun and the Arvand Rivers is about 10 per cent, and at the intersection of these rivers, about 30 per cent. Due to the drastic changes in depth at the intersection, the relative size of the materials has not been unexpected.

Also, the concentration of suspended sediments obtained at different depths from the water surface is shown in Figure 3. As it is known, sediments become denser with increasing depth. The concentration of sediment at Karun station has the lowest, and the station located at the intersection of the Arvand and the Karun Rivers shows the highest concentration of suspended sediments. The results show that the sediments of the region are fine-grained and the complexity of the flow in the confluence of the Arvand and the Karun is very significant.

Table 3. Results of bed sediment sampling

No. Station	Location of Station	Results of Grading	
		Bigger than 40μ (sand)	Smaller than 40μ (fine-grained)
1	Karun	4%	96%
2	North of Arvand	12%	88%
3	Confluence of Rivers	30%	70%
4	South of Arvand	12%	88%

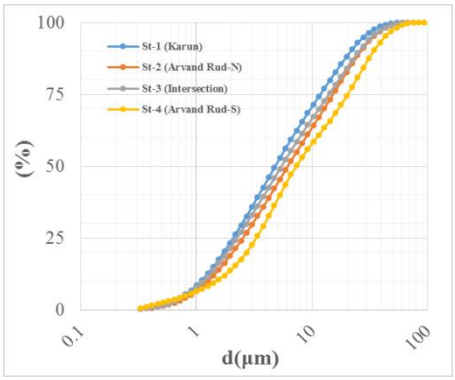

Figure 2. Results of bed sediment sampling

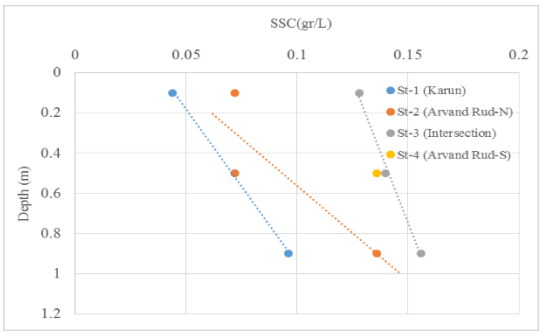

Figure 3. The concentration of suspended sediments obtained at different depths

3.3. Tide

In this section by considering the level measurement in the study area, the tide has been analyzed. Figure 4 shows the measured data of water level changes. As shown in Figure 5, there are significant changes in the water level at the beginning of the data that need to be considered.

The first step in analyzing tidal data is to find the appropriate amplitude and phase of the component with the least squares. IOS Tidal Package has been used to differentiate between water level changes caused by tides and other factors [6]. The range of tidal level changes compared to the measured levels in Figure 5 and the range and phase values of tidal components are presented in Table 4.

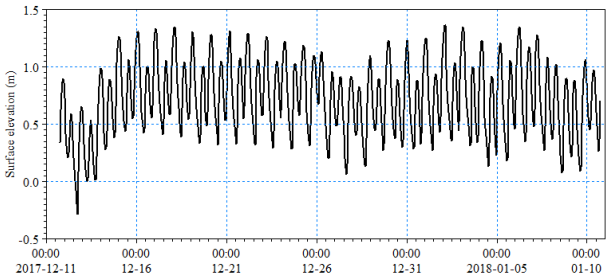

Figure 4. Changes in the water level in the area of Shahid Mousavi Shipbuilding Complex

Table 4. The amplitude and phase of tidal components based on the analysis of water level changes

O1		K1		S2		M2		Z0	
Amp.	Phase	Amp.	Phase	Amp.	Phase	Amp.	Phase	Amp.	Phase
0.02	0.0606	0.2077	20.77	0.0551	146.45	0.3086	73.51	-	0.72

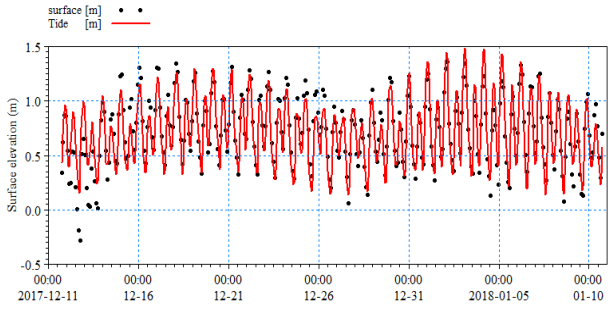

Figure 5. Changes in the water level in the area of Shahid Mousavi Shipbuilding Complex

The value of F is approximately equal to 0.74, which indicates that the tide type is mixed but is mostly semi-diurnal. Therefore, it is expected that two peaks and two bottoms with different intensities will be observed every day [7].

$$F = \frac{K_1+O_1}{M_2+S_2} = \frac{0.2077+0.0606}{0.3086+0.0551} \approx 0.74 \quad (1)$$

Another parameter that is considered is the difference between measured values and tidal values, which shows the effect of environmental factors such as wind set-up, interaction of tidal components, flow phase difference in two different environments, and upstream river flow. Figure 7 shows the residual value of the water level and its positive and negative values. By considering the geographical location of the study area, one of the impressive parameters in the water level is the Karun River which seems to prevent the spread of tides inside the river whenever the flow rate is significant. Considering that the measurements were made in the winter, a sharp difference in the initial range could be the result of a significant flow in the Karun River. However, due to the construction of a dam upstream of the river, the amount of dam overflow reduced so can cause the significant influence of tide and salty water in the river, the remaining positive value confirms this.

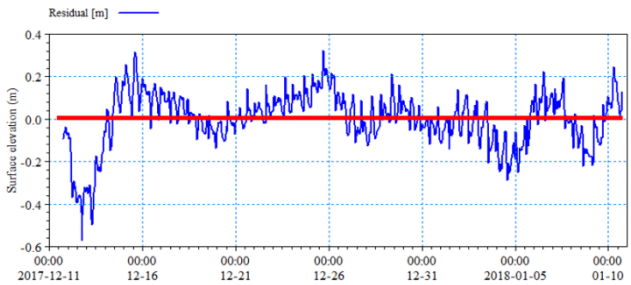

Figure 6. The difference between the level changes of the measured water level and the tidal values

3.4. CTD

In this part of study examined the result of measurements. The components of flow velocity in x and y direction, salinity, heat, and salinity are measured in three depths. Water level changes have also been measured at the same time as some of these measurements. Figure 8 shows the time interval of the measurements. As is clear, measurements were made in two periods, minimum and maximum tides.

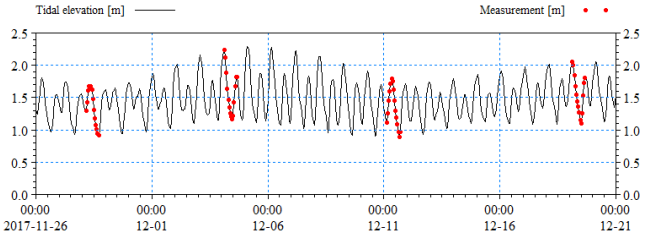

Figure 7. Measurement period (red dots)

3.4.1 Flow pattern examination

The velocity pattern in measured stations 1 to 4 is shown in Figure 8. It shows the flow velocity in different positions with the red line. Measurements made in Karun show that the prevailing flow rate in this area is towards Arvand, and the Arvand tide can only reduce the flow rate of this river locally. The direction of the flow at the station is to the north, which, considering its location, indicates the canalization of the tidal current in this area. At the intersection of the Arvand and Karun rivers, the flow is affected by the speed of the Karun Rivers. At Station No. 4, which is located south of the area, the direction of north-south flow and the amount of flow velocity are diffused, indicating that the impact of the Karun River in this area is decreasing and the tidal effect is visible.

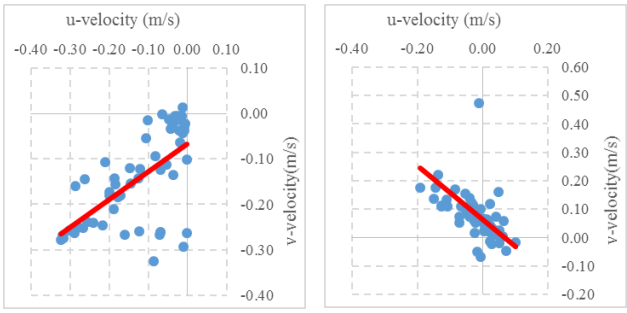

Station No. 1 (Karun) Station No. 2 (North of Arvand)

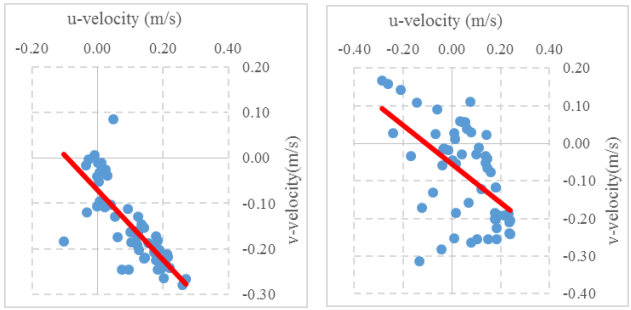

Station No. 3 (Intersection) Station No. 4 (South of Arvand)

Figure 8. Current velocity at measuring station

3.4.2 Determination salinity and temperature pattern

The salinity and heat patterns can be examined in two ways. The first is to examine the pattern of salinity and temperature changes at a station and at different time intervals. Accordingly, the trend of salinity and temperature changes at Station 1 shows that the salinity rate at this station increased during the measurement period while the temperature decreased. In the first period, we see a decrease in the measured salinity at Station 1, which indicates that the inflow of low-salinity water source (Figure 9 and Figure 10). The sources of low-salinity water are typically rivers, lakes or aquifers associated with meteoric water.

The second way to check the salinity and temperature pattern is to compare the results of different stations over a period of time. According to this issue, the study of salinity pattern in the first period shows that the changes in this parameter in station 1 are different from stations 2 and 4, so that in station 1 the salinity decreases with increasing water level, but in Stations No. 2 and 4 increases in salinity. Examination of temperature changes shows that the process of change of this component in three stations is close to each other, so that increasing the water level increases the temperature in all three stations (Figure 11).

In the second period, the trend of salinity changes in the three stations is very close to each other (correlation coefficient between the result of station 4 and 2 is 0.81, and between station 2 and 1 is 0.93), so that in all three stations, the salinity decreases with increasing water level. Also, temperature changes in the three stations are very similar to each other (correlation coefficient between the result of station 4 and 2 is 0.93, and between station 2 and 1 is 0.88), so that with increasing water level, the temperature decreases (Figure 12).

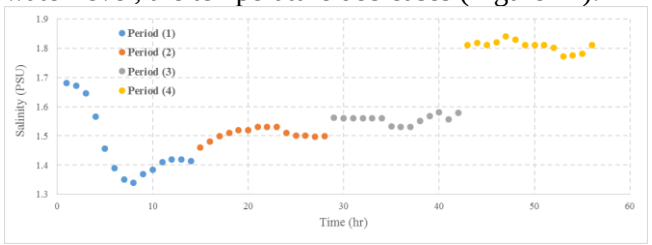

Figure 9. Salinity changes at Station 1 (Karun) at different periods

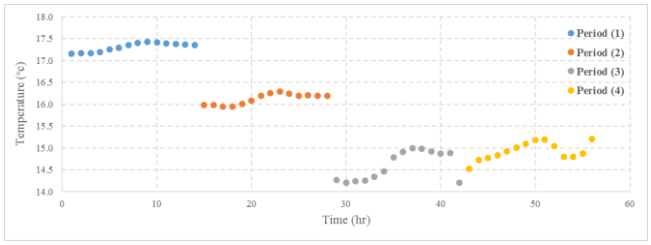

Figure 10. Water temperature changes at Station 1 (Karun) at different periods

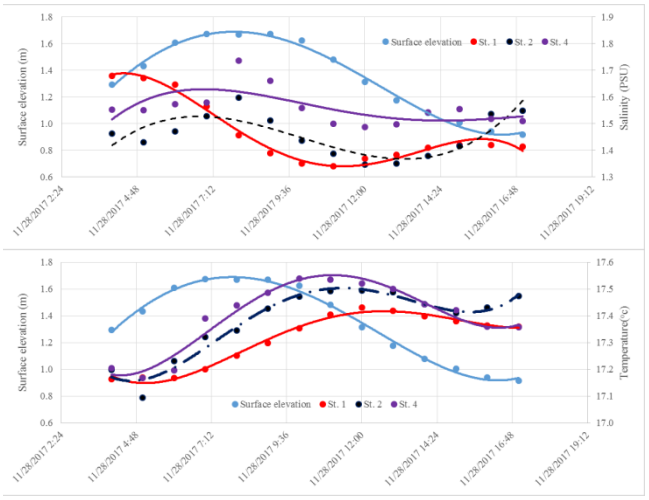

Figure 11. Changes in salinity and temperatures in different stations compared to changes in water level (tide) in the period 11/28/2017

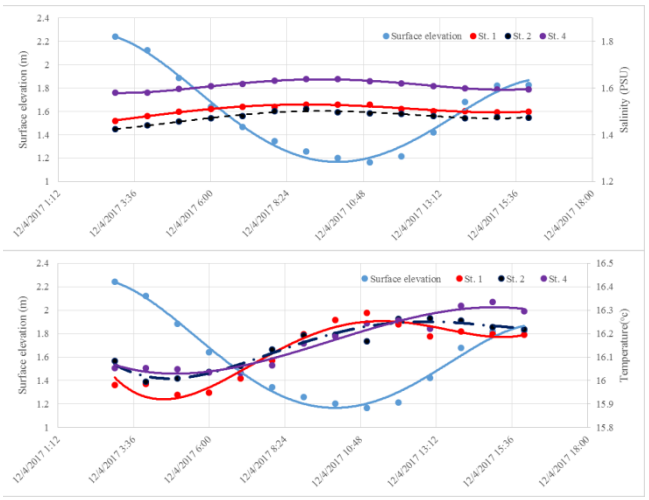

Figure 12. Changes in salinity and temperatures in different stations compared to changes in water level (tide) in the period 04/12/2017

4. Conclusions

In this study, a month-long analysis of the measured data of marine phenomena at the collision of Karun and Arvand rivers has been analyzed. These studies include tides, changes in water level, hydrography, and granulation, sedimentation and flow. Studies show that Karun flood currents have caused significant changes in the bed of the intersection of Karun and Arvand rivers, and most of the sediments in the study area are fine-grained, and at the intersection of Arvand and Karun rivers due to drastic changes. Depth of sediment

is greater than that of other coarse-grained areas, and the concentration of sediment increases with depth of motion, and the lowest and highest sediment concentrations are related to Karun stations and Arvand Karun intersection, respectively. According to the measurement, it was determined that the flow regime is mixed but mostly half daily and two peaks and two depths with different intensities are expected to be observed daily and Karun river flow is one of the influential parameters in the water level. So that whenever the river flow is significant, it will prevent the tidal wave from spreading inside the river. The construction of a dam at the top of the river and the reduction of the dam's headwaters into the river cause a significant infiltration of tides and salinization of river water.

5. References

[1] Ajab pour, A., 2015. *Investigating the flow of water at the intersection of Arvand River and Karun through the influx of tidal waves*. The first national environmental conference,.

[2] Shafiee sarvestani, R., Sadrinasab, M., *Plum modeling at the mouth of the Arvand River*, 7th ICOPMAS, Tehran, Iran, 2006

[3] Etemad-Shahidi.A , et al,. 2015. *Effect of sea level rise on the salinity of Bahmanshir estuary*, Int. J. Environ. Sci. Technol., Vol.12, pp. 3329–3340.

[4] Khosravi.M, et al,. 2017,. *Observation of currrents in Karun River*, Research in Marine Sciences, pp. 50-58.

[5] Gohari, S., Amraei, M., *Study of the effect of connection angle on current characteristics in cross-channels*, Water and Soil Science, 2014, Vol. 24, pp. 243-257.

[6] Foreman, M.G., 1996. *Manual for Tidal Heights Analysis and prediction*. Pacific Marine Science Report 77-10, Institute of ocean science, Canada.

[7] Boon, J.D. 2011. *Secrets of the Tide and Tidal Current Analysis and Applications, Storm Surges and Sea Level Trends*. Woodhead Publishing,.

INTERNATIONAL JOURNAL OF
COASTAL & OFFSHORE ENGINEERING IJCOE Vol.5/No. 1/Spring 2020 (31-43)

Available online at www. ijcoe.org

Seismic Design of Subsea Jumper per ISO:

Part I- Preliminaries

Sirous F. Yasseri

Brunel University London; Sirous.Yasseri@Brunel.ac.uk;

ARTICLE INFO

Article History:
Received: 28 Aug. 2020
Accepted: 14 Nov. 2020

Keywords:
Subsea Spools
Soil- spool interaction
ISO 19901
ISO 19902
Geohazard
ALE and ELE

ABSTRACT

Subsea rigid steel spools (spool) are used to connect subsea equipment using diver-less connectors. Spools must meet functional requirements such as pressure, temperature, thermal expansion, environmental load, installation loads, lack of fit (misalignments), etc., yielding numerous loading conditions. The installation accuracy that the installation contractor can achieve is another issue. Thus, it is inevitable that numerous geometries to be investigated and perform several iterations in search of a suitable configuration. The no-burst concept, in conjunction with a High Integrity Pressure Protection (HIPP) system, leads to heavier spool wall thickness, hence less structural flexibility which in turn increases reactions on the subsea connectors, which in turn is transferred to the adjoining equipment. Add to this complexity, the seismic qualification requirement if a jumper is in an earthquake-prone area.

This is the first part of a three-part paper that discusses experiences gained in designing spools in 500m of water. The primary focus of the paper is on seismic design, but other issues are discussed including loading & load combinations, increasing the structural flexibility without lowering the natural frequencies; limitation imposed by the subsea connectors, the neighboring equipment loads, and tolerances. Generally, the capacity envelope of connectors will govern most of the time.

These papers build on the existing literature and liberally draws from them. The objective is to summarise and bring together existing research data needed to design subsea rigid spools.

1. Introduction

Deepwater pipelines are connected to manifolds/trees/FTA/ITA by utilizing diver-less mechanical connectors and rigid spools. Deepwater rigid spools must accommodate expansion displacement due to high product temperatures, possible soil's low strength, and other phenomena such as pipe walking and debris flows. Spools must also accommodate fabrication and installation tolerances. These requirements, and others, derive the spool geometry and can lead to complex configurations that cause installation difficulties.

An issue requiring investigation is the selection of vertical or horizontal orientation of the connection system (Figure 1). The geometry of the field and installation vessel may also be determining factors. Each orientation exhibits several advantages and disadvantages. However, both systems have been proven as an acceptable solution

There are 2 main types of connectors used in deep-water applications. Figure 2 shows typical horizontal and vertical connectors as well as one type of flanged connections.

The structure of these three interlinked papers are as follows:

Part 1: deal with the background data

Part 2: Describes ISO requirements and derivation of earthquake time histories

Part3: Describe the design of subsea spools with a focus on the seismic design.

(a): Horizontal Spool

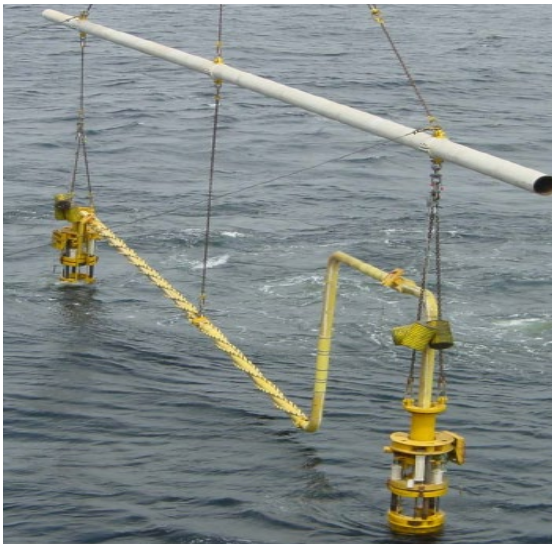

(b): Vertical Spool

(c): a complex Spool

Figure 1. Three types of geometry (courtesy of JP Kenny)

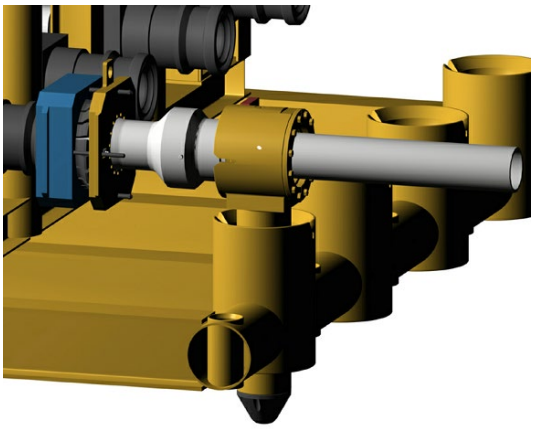

(a): Horizontal Connector

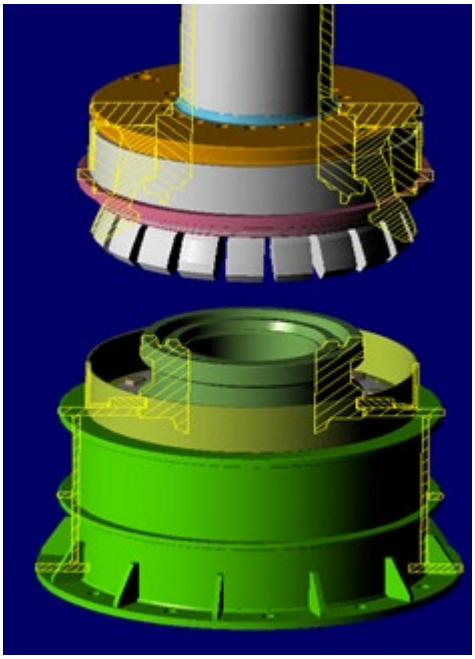

(b): Vertical Connector

(C) Typical flanged connection (diver assisted)

Figure 2. Typical Horizontal and Vertical Connectors (courtesy of JP Kenny)

Typical connector loads (Bending Moment) could be approaching the limits of the pipe on the spool piece assembly. The connector supplier needs to be aware of this and shall be able to offer a suitable pup-piece design (e.g. forged) as required. Connector loading capacity shall be confirmed by the connector supplier during Request for the information by spool designers. Figure 3 shows spools with a very complex geometry if a rigid spool is used.

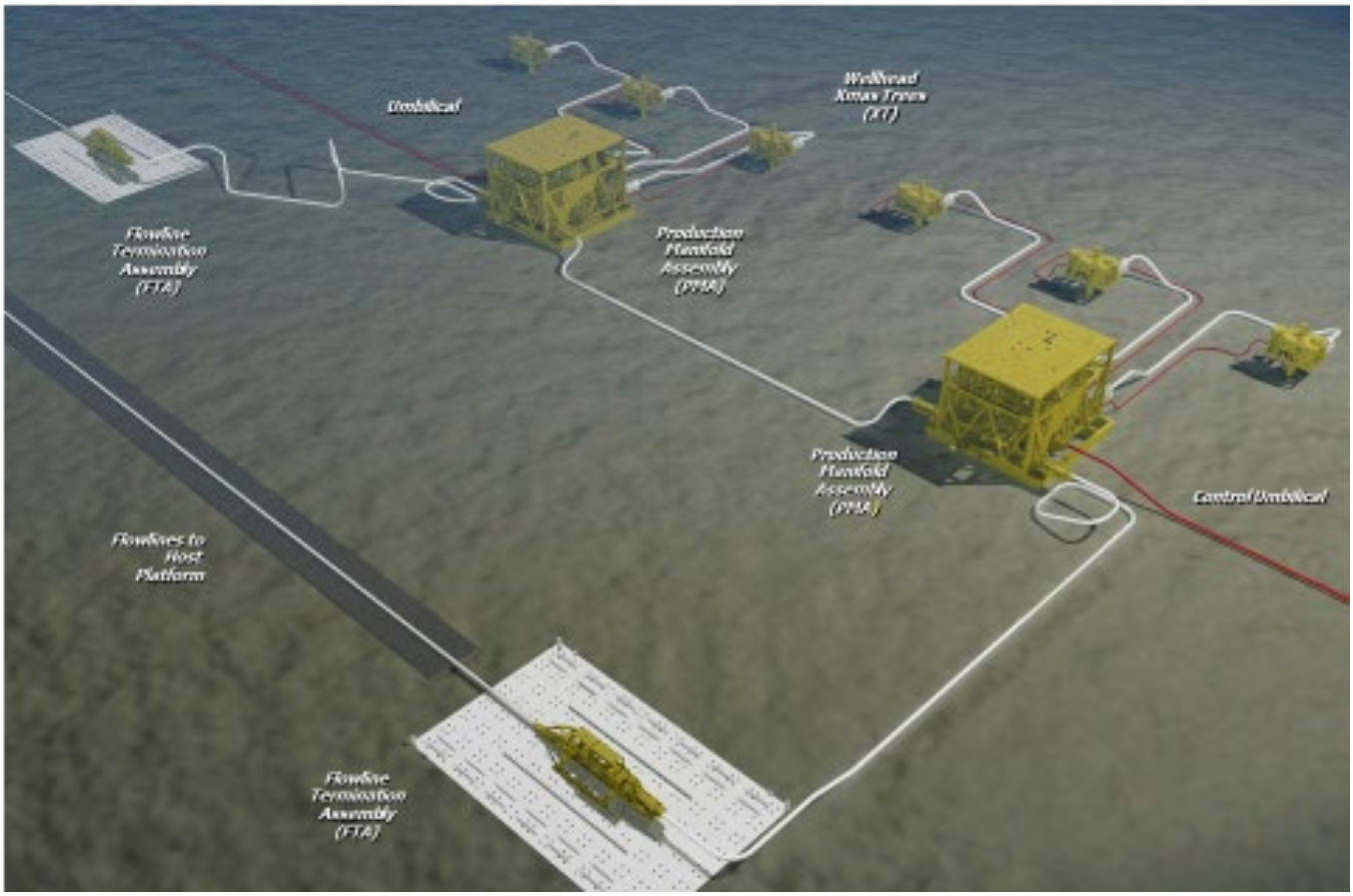

Figure 3. A cluster-type subsea architecture consisting of two manifold each connected to three X-trees.

Most often than not, deep-water spools are stretched to fit into the subsea connectors' receptacles, which creates substantial stresses in a thick-walled rigid spool. Operational loads (pressure and temperature), installation tolerances, and lack of fit aggravate this situation. High pressure requires heavier wall thickness which reduces the much-needed flexibility. If the region happens to be moderately seismically active, then the design is more demanding. In general, the capacity of a jumper is almost exhausted before the application of the seismic load. Adding more flexibility would alleviate his problem but could create another problem, which is making the spool prone to flow-induced vibrations. Thus, obtaining an optimal solution requires a lot of searching in the solution space. Though dealing with seismic load is the focus of this paper, other loads that a spool is expected to withstand must be borne in mind since their severity determines how much margin is left for the seismic loading. There are cases where using a rigid spool is almost impossible and flexible pipes are used instead.

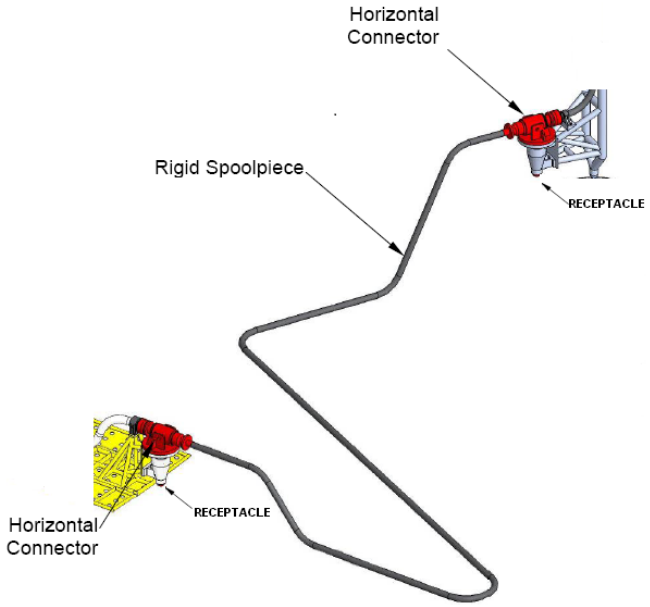

Figure 4. Once the subsea structures have been installed the distance between the connectors and the angular alignment of the hubs will be established by the survey.

2. Tolerances

Spool pieces are designed to accommodate installation errors, which put a heavy demand on them. However, there is a limit to what can be achieved, hence some tolerances must be imposed on all possible errors (Figure 4).

Tolerances that need to be considered are:

• Structure Installation Tolerances

• Metrology & Fabrication (tolerance between metrology reference e.g. stab receptacle on the lower structure, and inboard hub)

• Connector system tolerances

• Installation Tolerances

2.1. Tolerance for the structure (Typical installation

Based on the industry practice tolerances for wellhead guide bases, manifolds, Flowline termination assembly, and in-line tees are given below:

Wellhead Guide-bases: Verticality ± 2 deg

Azimuth ± 15 deg

Manifolds Verticality ± 3 deg

Azimuth ± 5 deg

FTAs/in-line tees Verticality ± 5 deg

Distance between pairs of Christmas tree (x-tree) connection tie-in points:

25 ± 10 meters

Distance between production manifold and flowline connection:

35 ± 5 meters

The spool configuration must possess adequate length, and angular capacity to accommodate these tolerances. If pre-fabricated spool elements are used they must have sufficient green material for cutting to size.

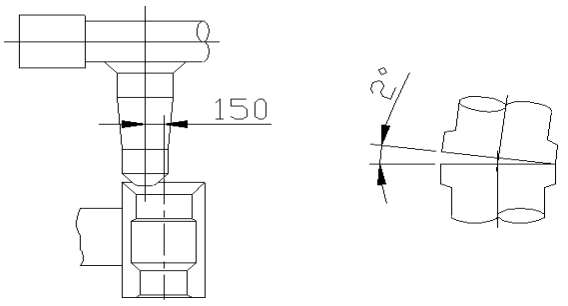

Figure 5. Connector's system Tolerances (courtesy of JP Kenney)

2.2. Metrology and Fabrication Tolerances

Once the subsea structures have been installed the distance between the connectors and the angular alignment of the hubs will be established by the survey (Figure 5).

These sizes are used to fabricate the spools to fit.

Typical metrology and fabrication tolerances are:

± 150mm in any three axes

± 2 degrees in any three axes

2.3. Connector's system Tolerances

Hub to connector tolerances arises from several sources including fabrication tolerances for the inboard structures, stack-up tolerances for two-part structures, and also the requirement that production spool shall be re-usable after tree interventions.

These followings are considered in the stress analyses of spools.

- Combinations of Extreme Tolerance and Misalignments

The angular & linear tolerances due to metrology & spool fabrication and misalignments could all be forced on the spool system during the installation and stroking connection. The spool shall be designed to accommodate all the possible combinations of angular & linear tolerances and misalignments.

- Connector Stroking (Figure 6)

Stroking length shall be considered in the stress analysis; it should be noted that where possible the local architecture has been adjusted so that stroking reduces maximum stresses.

2.4. Installation Tolerances

A distinction should be made between the installation tolerances, which will be quantified during offshore metrology, and the other 'residual' tolerances

The offshore installation tolerance shall be accommodated within the design of prefabricated spool kits that will have angular and length adjustment on 'closing' welds during spool fabrication.

The other tolerances shall be accommodated in the design flexibility of the spools.

The angular & linear tolerances due to metrology & spool fabrication and misalignments could all be forced on the spool system during the installation and stroking connection. The spool shall be designed to accommodate all the possible combinations of angular & linear tolerances and misalignments.

Metrology and spool fabrication have their tolerances which could cause misalignment at the connector hub face. Consequently, additional loads could arise from spool deformation because of induced forces during installation to match-up the connector faces.

The magnitude of these additional loads is dependent on the stiffness of the system near the connectors.

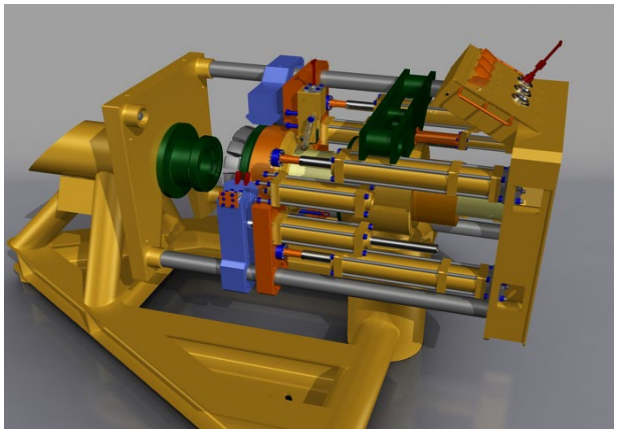

(a): Before stroking

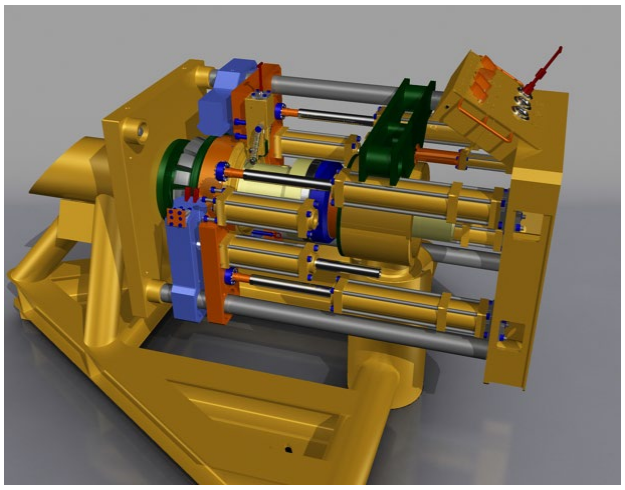

(b): After Stroking

Figure 6. Connectors' stroking

The following are a few consideration to mitigate the loading:

- The stiffness of the path through which the load travels from the connector into the inboard hub to the mounting structure as well as the steelwork of the inboard structures must be considered, which would allow for flexibility, hence reduction in connector loads
- Modeling the misalignments tolerances with kinematics constraints, this would provide certain flexibilities within the system, hence lower the localized bending moments at the connector supporting system.

3. Spool Installation Issues

A reasonable installation assessment that should be considered during the engineering design should be based on the following criteria:

• Installation is feasible with appropriate engineering input on 60-meter accumulative length (the pipe length) and 45-meter envelope (distance between connector to connector).

• Spool installation complexity and increased risks are introduced when the spool length is the 70-meter accumulative length and 50-meter distance between connector to connector.

• the spool width must be kept to the minimum.

• The center of gravity of the spool should be kept close to the main axis of the spool.

• The center of gravity, weight, geometry, flexibility, and the torsional stiffness of the spools are such that the complexity size and weight of the spreader bar and rigging are minimized.

• The lift capacity of the vessel crane at the required offset should be adequate.

• The lift capacity of the vessel crane is adequate given the crane radius and the appropriate dynamic amplification factor, skew loads, weight, and center of gravity of the spool uncertainty factors.

•For installation of rigid spools commonly they are lifted off the deck of the installation vessel or barge/supply vessel and lowered using the vessel's crane and either directly installed or abandoned and recovered by the winch.

4. Spool -soil interaction

When a spool that is resting on the seabed is subjected to transient loads, it interacts with the soil such that a continuous transfer of energy takes place between them. The effect of interaction on the dynamic behavior of a Spool is determined by the mechanical properties of spool and soil and the interaction mechanism and the type of dynamic loading (Ghannad et al [14], Ghannad et al [15], and Jafarieh and Ghannad [17]). The kind and intensity of the interaction depend on the physical processes that occur at the interfaces between them (see e.g. Gazetas and Dobry [11 and 12] and Gazetas [9 and 10]).

Analysis of spool–soil interaction for the design purpose requires a simplified, but a conservative, method, since it is not practical to model the entire soil-spool systems, to be modeled in great detail. The size of the overall system is so large that it's exact modeling by finite element methods is computationally expensive. Engineers are mainly interested in the response of the spool, and the soil to the extent it affects the spool, thus accurate modeling is only needed for the spool. Therefore, the overall system can be subdivided into subsystems with a suitable interface and imposed boundaries.

The far-field is not bounded and thus has an important effect on the wave dynamics. Waves that re traveling in the unbounded direction, cannot reflect as there are no hard boundaries. Because waves transport energy and in a real situation they won't return, we obtain a mechanism which irreversibly transfers energy from the near field to the far-field. This mechanism is called radiation damping which extracts energy from the near field (Lysmer & Kuhlmeyer, [16]). The effect is not dissimilar to that of viscous damping where some of the

energy is irreversibly converted into heat. The response of the structure will be very much reduced. For this kind of problem, the accurate modeling of radiation damping becomes a central issue (El Naggar & Bentley [5]). This is exactly the case for spools interacting with the seabed.

The method of implementing this radiation damping is also an issue. For practical reasons, the finite element model must be of a reasonable size. One approach is to model a finite portion of the soil using solid elements with defined soil behavior and properties. Then layers of elements are added around this model and allow them to absorb energy. This boundary layer is known as the silent boundary, the quiet boundary, the absorbing boundary, or transmitting boundaries. Most software packages have implemented the Lysmer & Kuhlmeyer [16] formulation. The element type is known as the infinite element with viscous damping capability. Abaqus element library includes such elements. Infinite elements take care of both far-field displacement and non-reflective boundary. An approximation would be to attach dashpots and springs to the model boundary to model the far-field stiffness and prevent reflection of the wave at the boundary. There are other variations of representing the far-field effect.

In addition to the radiation damping, internal friction in the soil also dissipates the seismic energy (Hardin & Drnevich[13]). In all cases, the soil material damping is assigned in the material definition, as the soil is explicitly represented in this type of modeling.

Given the number of cases to run for the design of spools, the above approach is only practical for the confirmatory final run. For design purposes, a simplified approach is used which is known as a beam on the Winkler foundation, where a spool is assumed to rest on a bed of springs (linear or no-linear). This simple approach gives very good results for the spools which is the focus of the attention here while providing no information for the soil strains and displacement. There is a variety of ways to implement the idea of Bean on Non-linear Winkler Foundation (BNWF); see for example Vesic [32], El Naggar [6], El Naggar et al [7], or Boulanger et al [4].

Beams on the nonlinear Winkler foundation (BNWF) method has been used extensively to model the soil-pipe interaction when both inelastic behavior and dynamic effects are present. BNWF models can account for various complex conditions. Among others, Matlock et al.[24], Novak [26], Nogami et al [25], Makris and Gazetas [23], and El Naggar and Bentley [5] used BNWF models for piles subjected to lateral dynamic loads.

Boulanger et al. [5] developed a BNWF model utilizing springs in series, with dashpots representing radiation damping. El Naggar and Bentley[5] introduced dynamic *p–y* curves for dynamic lateral response analysis of piles. El Naggar et al[7] proposed a new combination of free-field ground motion analysis and BNWF for nonlinear dynamic response analysis of offshore piles. They used commercial software to verify their proposed BNWF model against the published centrifuge test data on seismic response of piles and they reported a very good fit. Some of these models include the effect of gaping between pile and soil.

In the BNWF method, the spool is represented as a series of discrete beam-column elements resting on a series of springs and dashpots representing the nonlinear dynamic behavior of the soil. To determine the kinematic response, the “free-field” ground motion time histories are calculated in a site response analysis. This idea of a non-linear Winkler foundation can easily be implemented in Abaqus, by defining the seabed as a plane surface with defined flexibility in the vertical direction. The lateral and axial non-linear behavior is defined by frictional characteristics seabed allowing the spool to slip when the shearing force at the interface exceeds the capacity.

Spools on a non-linear Winkler foundation are much simpler than pile-soil interaction; since pile encounter various layers of soil, spools are resting only on one layer for its entire length. This simplifies the representation of the soil in the analysis of the spools. The resistance of the seabed to the axial and lateral movements are modeled with friction at the interface of the spool and the seabed, which resembles an elastic-plastic spring. The slope of the elastic section is controlled by defining a break-out (or sliding) displacement, generally about 1mm. The axial and lateral friction is defined as lower and upper bounds. The upper bound is designed to account for resistance to break out due to probable embedment.

Applying damping to such a model poses some difficulties. Since only the spool material is modeled, applying the steel material damping is straightforward. Generally, Rayleigh damping is used in the time domain direct interaction analysis for the implementation of damping. Damping at the interface for the axial and lateral direction is taken care of by the defined friction at the interface. One could use the contact damping facility to address this interface issue. However, determining the damping coefficient is problematic. Damping in the vertical direction depends on the break-out resistance and velocity of the returning pipe impacting the seabed as well as the soil properties to allow its rebound. This damping is ignored in the current work.

Two other sources of damping are soil hysteretic damping and radiation damping, which are major sources of energy dissipation. These can be implemented by dashpots. In some DNV publications, it is implied that soil hysteretic and radiation damping

may be added to the steel damping and apply these composite damping using the Rayleigh method. An "effective damping" can be introduced using some combination of all damping, but the effective damping depends on soil structure dynamic properties.

In a non-linear time-domain analysis Rayleigh approach is used to implement damping (Spears and Jensen [29]). The problem with the Raleigh method is that its parameters are calibrated using natural frequencies of the system in the linear range; as the natural frequencies change due to complex non-linearity in soil-spool iteration, the Rayleigh effect is unknown. While DNV algebraically adds all damping ratio, Wolf [34 and 35] provides an expression for adding various damping using the natural frequencies of various components in the interacting system. This expression is a function of the soil stiffness and the participating mass which are not easily determined. There is no need for Wolf's simplification [35] as it is quite straightforward to use viscous damping for the soil radiation as well as hysteretic damping in the Abaqus analyses. Later sections discuss how to determine the damping coefficients.

5. Soil Dynamic Properties

Inputs for seismic analysis of soil-spool include stiffness and material damping of the soil; Makris & Gazetas, [23]. Soil stiffness can be expressed in terms of the shear wave velocity or the shear modulus. Small-strain shear-wave velocity,V_s, is directly related to small-strain shear modulus G_{max} by [28]:

$$G_{max} = \rho V_s^2 \qquad (1)$$

where ρ =mass density of soil. The soil's secant shear modulus may be used to represent the average soil stiffness at high to moderate strains. The relationship betweenG_{max}, G, shear strain γ, and shear stress $\tau$is illustrated in Figure 7. Also illustrated in this figure is the relationship between the stress-strain hysteresis loop for one cycle of loading and the material damping ratio.

the soil's material damping, D is an indicator of the energy dissipation capacity of the soil. The source of material damping is the strain rate effect, friction between soil particles, and nonlinear soil behavior. The hysteretic damping ratio may be determined by

$$D = W_D/(4\pi W_s) \qquad (2)$$

where W_D=energy dissipated in one cycle of loading, and W_s =maximum strain energy stored during the cycle. As noted in Figure 7, the area inside the hysteresis loop is W_D, and the area of the triangle is W_S. Theoretically, there should be no dissipation of energy in the linear elastic range for the hysteretic damping model defined by Equation 2. At relatively low strain levels, energy dissipation is measured using laboratory specimens.

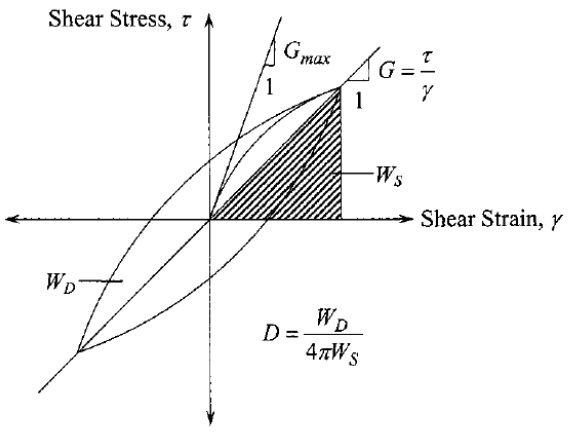

Figure 7. Hysteretic loo for one cycle of Loading Showing G_{max} , G and D

Note that the damping ratio at very low strain is a constant quantity and is known as the small-strain damping ratio D_{min} . At higher strains, nonlinearity in the stress-strain relationship causes the material damping ratio to increase with increasing strain amplitude.

The current state of practice for determining G and D for ground response analysis involves estimating or measuringV_s, in the field and estimating or measuring the variation of G and D with g primarily in the laboratory. It is common practice to normalize G by dividing by G_{max} .

Many studies have been conducted to characterize the factors that influence G/G_{max} and D - See for example; Seed and Idriss [27]; Hardin and Drnevich [13]; Ishibashi and Zhang [22]; Seed et al. [27]; Idriss and Sun et al. [21]; Vucetic and Dobry [33]; Stokoe et al. [30]; Darendeli [31]. This paper primarily uses Idriss and his co-workers' studies.

The most important factors that affect G/Gmax include g, mean effective confining stress, soil type, and plasticity index (PI). Other factors that affect G/G_{max}, but appear to be less important, include (according to Darendeli [31]): frequency of loading, number of loading cycles, over-consolidation ratio, void ratio, degree of saturation, and grain characteristics. The most important factors that affect D are g, mean effective stress, soil type, and PI (plasticity Index), frequency of loading, and several loading cycles.

As noted earlier, the dynamic soil properties are defined by the damping ratio and shear modulus degradation curves. These curves were determined for different soil t; e.g. Seed and Idriss [27], and Seed and Sun [21] proposed curves for clay and sand. Seed and Idriss [27] give three curves for the lower bound, the upper bound, and the average values. These curves are shown in Figure 8. The damping curves for sand with the same range of shear strain are shown in Figure 9. Note that lower bound sand refers to less stiff sand with

less damping ratio compared with the upper bound sand at the same shear strain.

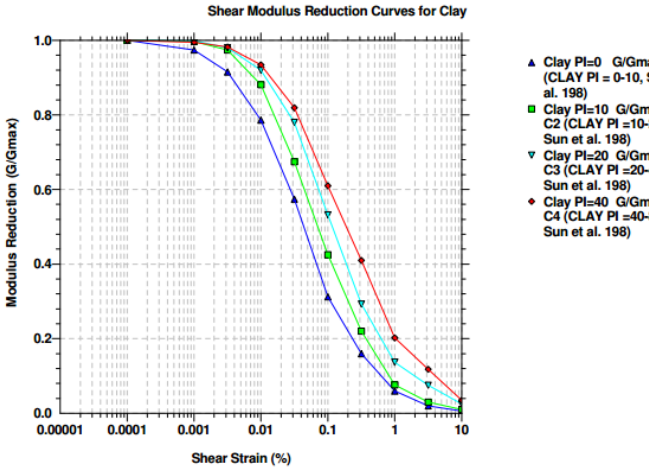

Figure 8. Shear modulus degradation curve for clay-from [27]

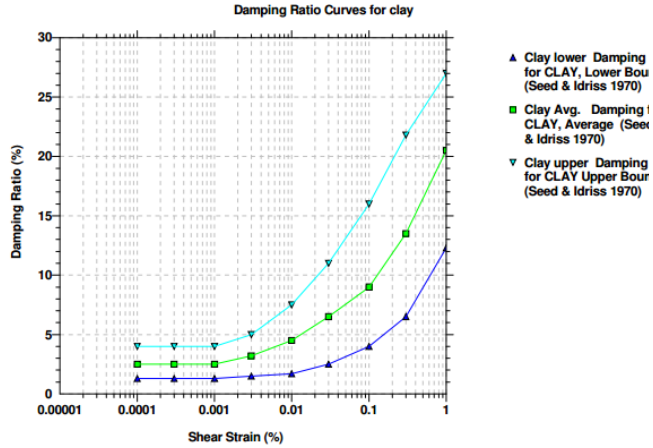

Figure 9. Damping curves for clay- from [27]

The shear modulus degradation curves for sand (Figure 9) and the damping ratio curves for san (Figure 10) can be found in Seed and Sun[21]. In the literature, these curves can be found for different levels of the plastic index for clay and different confining pressures for sand.

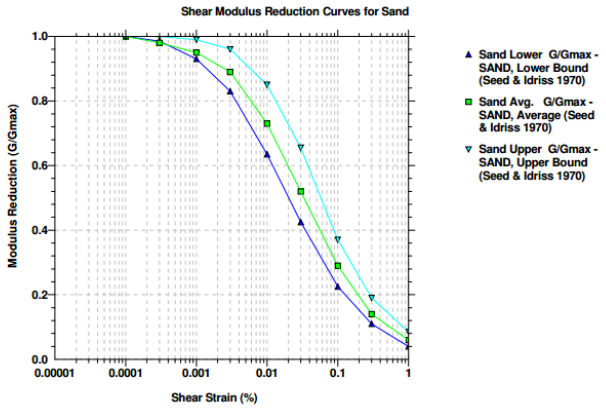

Figure 10. Shear modulus degradation curve for sand [21]

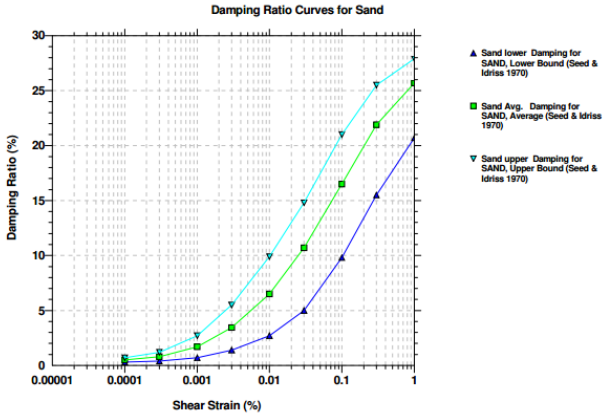

Figure 11. Damping curves for sand with the same range of shear as in Figure 9 [21]

6. Sources Energy Dissipation

Various frequency-dependent and frequency independent sources of damping that are important for seismic design are:

- Frequency-dependent:
  - Structural material damping
  - Damping resulting locally from strongly nonlinear soil behavior adjacent to the spool
  - Soil material damping of permeable saturated permeable soils (from pore fluid moving relative to the soil skeleton)
  - Energy transport through the soil to the far-field namely the soil Soil radiation damping
  - Hydrodynamic damping, namely the velocity-dependent drag forces acting on the pile
- Frequency independent:
  - Structural friction damping (frictional damping in e.g. bolted connections)
  - Soil material damping for dry and impermeable soils (friction of soil grains moving to each other)

Including all different damping contributions in a mathematical model for earthquake response analysis should conceptually result in the most accurate estimate of the actual response of the structure, but this is quite uncommon in practice. Instead, an equivalent Rayleigh critical viscous damping percentage is often defined to approximate the effects of various damping mechanisms that are present in the real structure. However, the following problems can be named:

- Actual damping resulting from hysteretic behavior often is a nonlinear function of motion amplitude. Consequently, it is not easy to properly include damping in the Rayleigh formulation for dynamic analysis when the motion amplitudes vary strongly.
- By definition Rayleigh viscous damping is frequency-dependent, but the actual damping sources not necessarily are frequency-dependent, for instance,

hysteresis loops due to nonlinearities are frequency independent.

Computational advantages of using linear equivalent viscous Rayleigh damping traditionally were considered to outweigh whatever compromises are necessary for the viscous damping approximation. However, currently, it is believed that in nonlinear dynamic analysis a better approximation of actual damping is obtained when hysteresis behavior (by nonlinearities) and some additional Rayleigh damping are combined. For the low-level responses, the Rayleigh damping portion would govern the total damping, where it becomes negligible compared to the hysteretic energy dissipation for high-level responses.

The sources of damping are explained below:

Structural material damping- Structural damping results from micro-scale material straining (material damping) and friction between surfaces moving relative to each other. The former is related to heat production in materials due to vibrations, which is clearly, depends on the properties. The latter is provided by work done by friction in e.g. connections or other structural slipping surfaces. In practice, material and friction damping of the structure are lumped together into a single equivalent viscous damping parameter. Eurocode 8 [8] recommendations provide an equivalent viscous damping ratio of 5% critical to be included in seismic analysis. ISO 19901-2 and 19902. ISO [18, 19, and 20] recommendations provide maximum modal damping ratios of 5% for fixed steel offshore structures for the ELE events, but additional damping, e.g. hydrodynamic or soil damping, must be substantiated. For fixed steel offshore structures under ALE events where inelastic behavior of both structure and damping is likely, damping values varying up to 10% critical may be applicable. Some codes of practice allow maximum damping values of 5% critical to simulate damping originating from structural joint and hydrodynamic energy dissipation for seismic analysis of fixed concrete offshore structures. Any higher values according to these codes shall be justified by special studies.

Soil radiation damping: Radiation damping is the transport of structural vibration energy to the far-field, and sometimes referred to as geometric damping or attenuation.

Soil material damping: Soil material damping results from frictional forces between soil grains when the soil is vibrating. This friction induces a type of damping that is generally believed to be frequency independent (Hardin and Drenvich [13]) and is characterized by hysteresis soil behavior. For saturated permeable soils, the damping however is characterized better as viscous frequency-dependent damping, since it is governed by pore fluid motion through the soil skeleton generating heat energy. In the past, the soil damping was assumed to be frequency-independent because of convenience. Essentially an equivalent viscosity is defined as $\eta = 2G\zeta/\omega$ resulting in a constant damping ratio. Critical damping percentages can be estimated based on soil shear strain levels, plasticity index, and confining pressure according to Vucetic & Dobry [33]; Ishibashi & Zhang, [22]. In Eurocode 8 [8] an approximation of strain-dependent soil stiffness and damping parameters based on ground accelerations is given. This code allows high-level earthquakes damping ratios exceeding 0.10.

Damping at the soil-structure interface: Increased damping in the soil region surrounding the spool is important. Due to the relatively high deformation levels, extreme hysteresis behavior is locally present, resulting from high local soil strain levels and plastic shearing at the soil-spool interface. Other effects such as scour for clays may contribute to higher damping. The representative damping value strongly dependent on the displacement amplitude. As a consequence of highly plastic local soil behavior adjacent to the spool, radiation damping is reduced by this zone. In this paper, the effect of high strain on the degrading of shear modulus, hence reducing the radiation damping and increasing the soil material damping, is considered by using Idriss's curve (Figures 8 to 11).

Hydrodynamic damping*:* Spools are surrounded by water. During an earthquake the relative velocities of the pipe and the water are nonzero, drag and inertia forces will result according to Morrison's equation. The drag force varies linearly with the relative velocity of the spool and the surrounding water. Thereby, it forms additional viscous damping. The dependence on the relative velocity of the spool and the water makes the amount of damping difficult to determine during seismic events since the motion of the water itself is an uncertain input parameter. Thus it is uncertain if the hydrodynamic forces damp structure's response continuously or sometimes amplify it. In this paper, the hydrodynamic damping for the earthquake loading is assumed to be zero.

7. Soil Radiation Damping for Spools (soil-structure interface)

In dynamic seismic soil-structure interaction, soil damping must be included in the numerical analysis to match numerical and experimental results. However, damping tends to increase for increasing loading rates and frequency. Various researchers (Gazetas & Dobry [12]; Nogami, Otani, Konagai, & Chen, [25]; Makris & Gazetas, [23]; proposed to include a viscous damper parallel to the spring element representing the soil stiffness.

Other researchers (Berger [3], El Naggar [6],; El Naggar & Bentley, [5]) have proposed to define separately the interface, near- and far-field contributions for both linear springs and dashpots.

Both methods have resulted in relatively accurate predictions of dynamic pile response. El Naggar et al [7] compared numerical results with experiments and reported a good fit. The difference between these two approaches is the definition of soil stiffness. Since this stiffness is used to determine the soil damping, hence the amount of damping is different (by about a factor 2). The other difference between them is the first approach includes all six degrees of freedom, while the second method ignores rotational degrees of freedom.

In this work a modified version of the second approach (Berger's approach [3] will be used as described below

ATC-40 [2] has adopted Gazetas formulae. ASCE4-16 [1] uses Lysmer's equation [16] which is a predecessor of Gazeta equations. Eurocode 8 [8] also use a variation of Gazetas formulae for soil-foundation interaction (Table 1).

In this paper, we use a slightly different form for the radiation damping which gives about one-quarter of Gazaetas' values.

Table 1 Gazetas equations for the shallow foundation as summarised in Applied Technology Council (ATC) (1996). "Seismic Evaluation and Retrofit of Concrete Buildings ATC-40." Volume 1 and 2 November.

Stiffness Parameter	Equation
	Surface Stiffnesses
Vertical Translation	$K_z' = \frac{GL}{1-\nu}\left[0.73+1.54\left(\frac{B}{L}\right)^{0.75}\right]$
Horizontal Translation (toward long side)	$K_y' = \frac{GL}{2-\nu}\left[2+2.5\left(\frac{B}{L}\right)^{0.85}\right]$
Horizontal Translation (toward short side)	$K_x' = \frac{GL}{2-\nu}\left[2+2.5\left(\frac{B}{L}\right)^{0.85}\right]+\frac{GL}{0.75-\nu}\left[0.1\left(1-\frac{B}{L}\right)\right]$
Rotation about x-axis	$K_{\alpha x}' = \frac{G}{1-\nu} I_x^{0.75}\left(\frac{L}{B}\right)^{0.25}\left(2.4+0.5\frac{B}{L}\right)$
Rotation about y-axis	$K_{\alpha y}' = \frac{G}{1-\nu} I_y^{0.75}\left[3\left(\frac{L}{B}\right)^{0.15}\right]$
	Stiffness Embedment Factors
Embedment Factor, Vertical Translation	$e_z = \left[1+0.095\frac{D}{B}\left(1+1.3\frac{B}{L}\right)\right]\left[1+0.2\left(\frac{2L+2B}{LB}d\right)^{0.67}\right]$
Embedment Factor, Horizontal Translation (toward long side)	$e_y = \left[1+0.15\left(\frac{2D}{B}\right)^{0.5}\right]\left\{1+0.52\left[\frac{\left(D-\frac{d}{2}\right)16(L+B)d}{BL^2}\right]^{0.4}\right\}$
Embedment Factor, Horizontal Translation (toward short side)	$e_x = \left[1+0.15\left(\frac{2D}{L}\right)^{0.5}\right]\left\{1+0.52\left[\frac{\left(D-\frac{d}{2}\right)16(L+B)d}{LB^2}\right]^{0.4}\right\}$
Embedment Factor, Rotation about x axis	$e_{\alpha x} = 1+2.52\frac{d}{B}\left(1+\frac{2d}{B}\left(\frac{d}{D}\right)^{-0.2}\left(\frac{B}{L}\right)^{0.5}\right)$
Embedment Factor, Rotation about y axis	$e_{\alpha y} = 1+0.92\left(\frac{2d}{L}\right)^{0.60}\left(1.5+\left(\frac{2d}{L}\right)^{1.9}\left(\frac{d}{D}\right)^{-0.60}\right)$

Equations to calculate the dashpot constant to account for the soil's energy dissipation are proposed by several researchers. The common practice is to add separate contributions for both hysteretic material damping and radiation damping as:

$$C_{dashpot} = C_r + C_m \quad (3)$$

The material damping is related to the soil's average shear strain amplitude which in turn related to local lateral pile displacement by:

$$\gamma_{avg} = \left(\frac{1+\vartheta}{2.5D}\right) \times (Horizontal\ deformtion\ of\ the\ soil\ layer) \quad (4)$$

The soil horizontal deformation (as a function of depth) is often obtained from simplified dynamic analysis or can be found by an iterative procedure. A damping ratio related to the average shear strain amplitude can be defined, and the dashpot constant then calculated as:

$$c_m = 2k_{secant}\frac{\zeta}{\omega} \quad (5)$$

Berger [3] was among the first to present expressions for the radiation damping. Berger [3] uses the analogy with 1D wave radiation in a rod and accounts for radiation of energy in both the direction of vibration (compression waves) as well as in the transverse direction (shear waves). Berger proposed [3] a dashpot coefficient equal to:

$$c_r = 2D\rho v_s\left(1+\frac{v_p}{v_s}\right) \quad (6)$$

Where v_p and v_s are related through the soil Poisson's ratio $\vartheta$when linear elastic material behavior is assumed:

$$v_p = v_s\sqrt{\frac{2(1-\vartheta)}{1-2\vartheta}} \quad (7)$$

Consequently, v_p tends to infinity if Poisson's ratio approaches 0.5 (un-drained soil material behavior), which is not realistic. According to Gazetas and Dobry [11] v_p maybe better estimated as:

$$v_p = \frac{3.4v_s}{\pi(1-\vartheta)} \approx 2v_s \quad (8)$$

Where they used Lysmer's [16] analog wave velocity, derived for surface foundations subjected to vertical oscillations. In their study, Gazetas and Dobry [12] also proposed an alternative expression that is based on assuming radiating waves in four quarter-planes (shear waves for two quarter-planes and compression waves for two quarter-planes) and assume a vertical plane-strain situation. Adding total energies that are radiated away will then yield the following expression for the dashpot coefficient:

$$c_r = 2D\rho_s v_s\left[1+\left(\frac{3.4}{\pi(1-\vartheta)}\right)\right]^{3/4}\left(\frac{\pi}{4}\right)a_0^{-1/4} \quad (9)$$

Where $a_0 = \pi fD/v_s$

In the design of spools, Equation3 will be used to introduce dashpots into the model. The radiation damping given by Equation 6 should be separated into two parts

$$C_r = 2D\rho V_s + 2D\rho V_p = 2D\rho V_s + 4D\rho V_s \quad (10)$$

In the axial and transverse direction, the dashpot constant is assumed to be

$$C_{rx} = C_{ry} = D\rho v_x \quad (11)$$

And for the vertical direction

$$C_{rz} = D\rho V_s\ . \quad (12)$$

Here, D is the spool diameter. The effect of embedment, (which enhances damping (Gazetas 1991)), is ignored due to its uncertain nature as well as it is accounted for when determining the seabed friction coefficient. In the horizontal direction, the damping coefficient is half of Berger's equation [3], since in the analyses dashpot acts both in tension and compression, hence half. The reduction of radiation damping in the vertical direction by a factor of 4 is to acknowledge that the soil is a half-space (reduction by a factor 2) and spools tendency to lift (no damping in tension). Though the recommended values are half as much as researchers for which reported good fit between analysis and experiment (see El-Naggar and Bentley, [5]), and less than 1/8 of allowed by ASCE4-98, it is believed to be a good approximation to reflect the direction as the contact of spools with the seabed is not certain.

In this work damping related to the rotational degrees of freedom is neglected as per the Berger approach [3].

Most spools do not rest on the surface of the soil but are partly embedded. Embedment is known to increase both stiffness and damping of the foundation system, but the increase in damping is more significant (Novak, [26]). The effect of embedment on the soil damping will be ignored.

Table 2 Average soil damping and average reduction factors (+- one standard deviation) for shear wave velocityv_s and shear modulus G within 20m depth (Table 4.1 of Euro Code 8 [8]).

Ground acceleraions ratio, α·S	Damping ratio	$\frac{V_S}{V_{S,\max}}$	$\frac{G}{G_{\max}}$
0.10	0.03	0.90 (±0.07)	0.80 (±0.10)
0.20	0.06	0.70 (±0.15)	0.50 (±0.20)
0.30	0.10	0.60 (±0.15)	0.36 (±0.20)

Shear modulus and damping parameters must be measured by laboratory or field tests. Average reduction factors are given in Table 4.1 of Eurocode [8] and are reproduced in this study in Table 2. The peak ground acceptation, in conjunction with Table 2, will be used to determine the degradation of the shear modulus. It is suggested to ignore the soil hysteric damping in this design. However, if it is included, then no higher than 0.1 for the shear strain must be assumed;

i.e. the damping ratio should not exceed 10%, except by special studies.

8. Implementing Structural Damping

Non-linear time-domain analysis with direct time integration is used to address geometric or material nonlinearities in seismic analysis of the spool-soil system. One method of implementing material damping in a non-linear dynamic analysis is Rayleigh damping. Material damping for steel is specified in codes of practice as a percentage of critical damping. Since damping is not constant for all frequencies, assuming the same damping for all modes will over damp the system. Rayleigh damping approach allows calibrating its constant for two or more modes. A reasonable approach would be to enforce a Rayleigh damping curve that matches prescribed modal damping for the first and (say) tenth mode. There are other suggestions in the literature on how to calibrate the Rayleigh damping.

The damping of the structure is assumed to be viscous type and frequency dependant for the sake of convenience in the analysis. The proportional damping, or Rayleigh damping, also known as the classical damping expresses damping as a linear combination of the mass and stiffness matrices, that is,

$$C = \alpha M + \beta K \qquad (13)$$

Whereα andβ are real scalars with 1/sec and sec units respectively. The real normal modes are preserved in classically damped systems. However, the accuracy of response may be questionable because this approach is formulated for the linear response of the structure which may not be the available situation for all cases (i.e. structures with nonlinearities).

8. Concluding Remark

This part of a three parts paper [36 and 37] summarises data needed for the design of rigid subsea spools and where the background information can be found. The aim is to provide the designers of the subsea spool enough background data for their work. In summarising research papers the focus was on the modeling of the rigid subsea spool with a reasonable computational cost. The question of spool installation tolerances, soil, and structural damping, are discussed in this part.

The second part [36] focus is on the requirements of ISO for the aseismic design of rigid spool. The third part deals with the design of rigid spools.

9. References

1. ASCE4-16, (2016), *Seismic Analysis of Safety-Related Nuclear Structures*. Published by ASCE to replace ASCE4-98 Seismic Analysis of Safety-Related Nuclear Structures and Commentary
2. Applied Technology Council (ATC) (1996), *Seismic Evaluation and Retrofit of Concrete Buildings ATC-40,* Volume 1 and 2 November.
3. Berger, B. S. (1977), *Vibrations of An Infinite Orthotropic Layered Cylindrical Viscoelastic Shell in An Acoustic Medium*, Mechanical Engineering, 99, 105.
4. Boulanger, R. W., Curras, C. J., Kutter, B. L., Wilson, D. W., & Abghari, A., (1999), *Seismic soil-pile-structure interaction experiments and analyses,* Journal of Geotechnical and Geoenvironmental Engineering*, 125,* 750-759.
5. El Naggar, M. H., and Bentley, K. J. (2000), *Dynamic analysis for laterally loaded piles and dynamic p-y curves,* Canadian Geotechnical Journal, 37, 1166-1183.
6. El Naggar, M. H. (1996), *Nonlinear analysis for dynamic lateral pile response*, Soil Dynamics and Earthquake Engineering, 15, 233-244.
7. *El Naggar, M., Shayanfar, M.A., Kimiaei, M., Aghakouchak, A.A.,*(2005), *Simplified BNWF model for nonlinear seismic response analysis of offshore piles with nonlinear input ground motion analysis,* Canadian Geotechnical Journal, 42, 2, pp. 365-380.
8. Eurocode 8: (2004) *Design of structures for earthquake resistance*.
9. Gazetas, G., (2012), *Nonlinear Soil-Foundation-Structure Interaction*, Proc.2nd International Conference on Performance-Based Design in Earthquake Geotechnical Engineering.
10. Gazetas, G. (1991), *Formulas and Charts for Impedances of Surface and Embedded Foundations*, Journal of Geotechnical Engineering 117, 1363-1381.
11. Gazetas, G. & Dobry, R. (1984a), *Horizontal Response of Piles in Layered Soils*. Journal of Geotechnical Engineering-ASCE*, 110,* 20-40.
12. Gazetas, G. & Dobry, R. (1984b), *Simple Radiation Damping Model for Piles and Footings,* Journal of Engineering Mechanics-ASCE, 110, 937-956.
13. Hardin, B. O., and Drnevich, V. P., (1972), *Shear Modulus and damping in soils*, Proc.ASCE: Journal of the Soil Mechanics and Foundations Division, 95(SM6), 1531-1537.
14. Ghannad, A.M., and Jahankha, (2004), *Strength Reduction Factors Considering Soil-Structure Interaction*, 13th World Conference on Earthquake Engineering Vancouver, B.C., Canada August 1-6, 2004 Paper No. 2331
15. Ghannad M.A., Fukuwa N. and Nishizaka R. (1998), *A Study on Frequency and Damping of Soil-structure Systems Using Simplified Model*, Journal of Structural Engineering (AIJ), 1998; 44B, 85-93.

16. Lysmer, J. and Kuhlmeyer R.L. (1969), *Finite Dynamic Model for Infinite Media*, Journal of Engineering and Mechanical Division, 859-877.
17. Jafarieh, A.H., and M. A. Ghannad M. A. (2014), *The Effect of Foundation Uplift on Elastic Response of Soil-Structure Systems*, International Journal of Civil Engineering, Vol. 12, No. 2, pp 244-256.
18. ISO 19902:2007, (2007), Petroleum and natural gas industries — Fixed steel offshore structures, Seismic Design Procedures, and Criteria.
19. ISO 19901-2, (2004), Petroleum and Natural Gas Industries – Specific Requirements for Offshore Structures – *Part 2: International Organization for Standardization: Seismic Design Procedures and Criteria.*
20. ISO 19901-4, (2002), Petroleum and Natural Gas Industries – Specific Requirements for Offshore Structures – *Part 4: International Organization for Standardization: Geotechnical and Foundation Design Considerations.*
21. Idriss, I. M., and Sun, J. I. (1992), *SHAKE91— A computer program for conducting equivalent linear seismic response analyses of horizontally layered soil deposits*, User manual, Univ. of California at Davis, Davis, Calif.
22. Ishibashi, I., and Zhang, X. J. (1993), *Unified dynamic shear moduli and damping ratios of sand and clay,* Soils Found., 33(1), 182–191.
23. Makris, N. & Gazetas, G. (1992), *Dynamic Pile Soil Pile Interaction- Lateral and Seismic Response*, Earthquake Engineering & Structural Dynamics, 21, 145-162.
24. Matlock, H., (1970), *Correlations for the design of laterally loaded piles in soft clay*, Preprints Second Annual Offshore Technology Conference, 1, 577-588.
25. Nogami, T., Otani, J., Konagai, K., & Chen, H. L., (1992), *Nonlinear Soil-Pile Interaction-Model for Dynamic Lateral Motion*, Journal of Geotechnical Engineering-ASCE, 118, 89-106.
26. Novak, M., (1974), *Dynamic stiffness and damping of piles*, Canadian Geotechnical Journal, 11, 574- 598
27. Seed, H. B., and Idriss, I. M. (1970), *Soil moduli and damping factors for dynamic response analysis*, *Rep. No. EERC 70-10*, Earthquake Engineering Research Center, Berkeley, Calif.
28. Seed, H. B., Wong, R. T., Idriss, I. M., and Tokimatsu, K., (1986), *Moduli and damping factors for dynamic analysis of cohesionless soils*, *J. Geotech. Eng.*, 112~111, 1016–1032.
29. Spears, R.E. and S. R. Jensen (2009), *Approach for Selection of Rayleigh Damping Parameters Used for Time History Analysis*, 2009 ASME Pressure Vessel and Piping Division Conference, PVP2009-77257, Prague
30. Stokoe, K. H., II, Darendeli, M. B., Andrus, R. D., and Brown, L. T. (1999), *Dynamic soil properties: Laboratory, field, and correlation studies,* Proc., 2nd Int. Conf. on Earthquake Geotechnical Engineering, Vol. 3, Lisbon, Portugal, 811–845.
31. Darendeli, M. B., and Lee, N. J. (1995), *Correlation study of nonlinear dynamic soils properties,* Final Rep. to Westinghouse Savannah River Company,
32. Vesic, M., (1961), *Beam on the elastic subgrade and the Winkler hypothesis,* Proc. International Conference Soil Mechanics and Foundation Engineering, Paris*, 1,* 845-850.
33. Vucetic, M. and Dobry, R., (1991*), Effect of Soil Plasticity on Cyclic Response,* Journal of Geotechnical Engineering-ASCE, 117, 89-107.
34. Wolf J.P., (1994), *Foundation vibration analysis using simple physical models*, Prentice-Hall Englewood Cliffs, N.J. The USA.
35. Wolf, J. P. & Deeks, A. J. (2004), *Foundation Vibration Analysis: A Strength-of-Materials Approach*. Elsevier, Oxford, U.K.
36. Yasseri, S, (2020), *Seismic Design of Subsea Spools per ISO: Part II- Seismic requirements*, IJCOE, Vol.4, No.2 , Summer 2020.
37. Yasseri, S., (2020), *Seismic Design of Subsea Spools per ISO: Part III- Analysis & Design*, IJCOE

Table of abbreviations

Abbreviation/ Acronym	Description
CDT	Cool Down Time
CPT	Cone Penetrometer Test
CRA	Corrosion Resistant Alloy
CMS	Corrosion Monitoring Spool
DEH	Direct Electrical Heating
ECA	Engineering Critically Assessment
FE	Finite Elements
FTA	Flowline Termination Assembly
ID	Inside Diameter
LB	Lower Bound
MEG	Mono Ethylene Glycol
MCM	Manifold Control Module
OD	Outside Diameter
PMA	Production Manifold Assembly
SIWHP	Shut-in Well-head Pressure
SMLS	Seamless
UB	Upper Bound

INTERNATIONAL JOURNAL OF
COASTAL & OFFSHORE ENGINEERING
IJCOE Vol.5/No. 1/Spring 2020 (45-54)

Available online at: www. Ijcoe.org

Investigation of Iranian Ports Performance in Oil Exchanges Using Data Envelopment Analysis

Ehsan Sarhadizadeh [1*], Mehrnaz Farzingohar [2], Niusha Mostoli [3]

[1] PhD Student, Faculty of Marine Science and Technology, University of Hormozgan; sarhadi@gmail.com*
[2] Assistant Professor, Faculty of Marine Science and Technology, University of Hormozgan; mfgohar@yahoo.com
[3] PhD, Faculty of Mathematics, Science and Research Branch, Islamic Azad University; mostoly@gmail.com

ARTICLE INFO

Article History:
Received: 11 Oct. 2020
Accepted: 18 Nov. 2020

Keywords:
Data Envelopment Analysis
Port Efficiency
Output Oriented CCR model

ABSTRACT

In this study, the performance and efficiency of 12 ports in the Persian Gulf, Oman and Caspian seas in Iran is evaluated using data envelopment analysis (DEA) method. DEA allows comparing the efficiency in revenue generation of ports with different economies. Two different modeling approaches were presented in this study; based on relating earnings to port operational capability and activity, and based on land indicators, infrastructure, and equipment. The results of this study showed that most of the ports in the Persian Gulf region had a relative efficiency in the field of petroleum products. On the other hand, a significant difference was observed between the nominal capacity of acceptance of petroleum products of ports and the volume of oil product exchanges.

1. Introduction

The near- and off-shore industrial facilities and their fleets threaten the marine ecosystem's health in the coastal areas. The pollutions caused by operations of these facilities gradually spread off to beaches and islands leading to fatal diseases and irreversible genetic disorders on humans. Iran's economy heavily relies on the oil industry, particularly through the naval fleets in the Persian Gulf and the Oman Sea in the South and the Caspian Sea in the North where major oil extraction facilities and export ports are located. For example, there are 34 oil fields with more than 800 wells (Fig. 1) and about 20,000 to 30,000 tankers per year (Fig. 2) in the Persian Gulf [18]. Therefore, there is a high risk of environmental hazards caused by these operations [8]. About 100 to 160 thousand tons of oil and petroleum products are shipped in the Persian Gulf annually, and the rate of oil contamination in the region is 47 times higher than the world average [17].

On the other hand, rich oil and gas resources in the Caspian Sea have attracted a flood of foreign investors since the mid-1990s, thereby strengthening the energy development platform in the region. These developments increased extraction of oil, gas and other industrial products in petrochemical plants and oil refineries significantly which lead to the spread of pollution in the Caspian Sea region [15]. Severe contamination of carbonic acid and petroleum products resulting from oil extraction and the construction of oil pipelines has caused the contamination of about 30,000 hectares of the region and environment hazards [3] (Fig. 3). According to the Department of Energy's Energy Information Agency (EIA), the Caspian Sea region has oil reserves of more than 17 to 33 billion barrels and oil production in the region was around 2.1 million barrels per day in 2005 and up to 3.8 million barrels per day in 2010 [2].

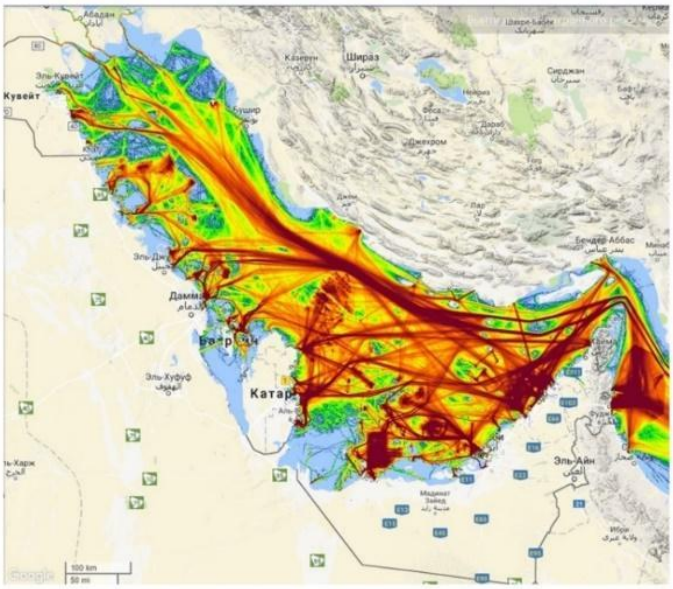

Fig. 1. Density map of ship traffic in the Persian Gulf in 2016, © marinetraffic.com

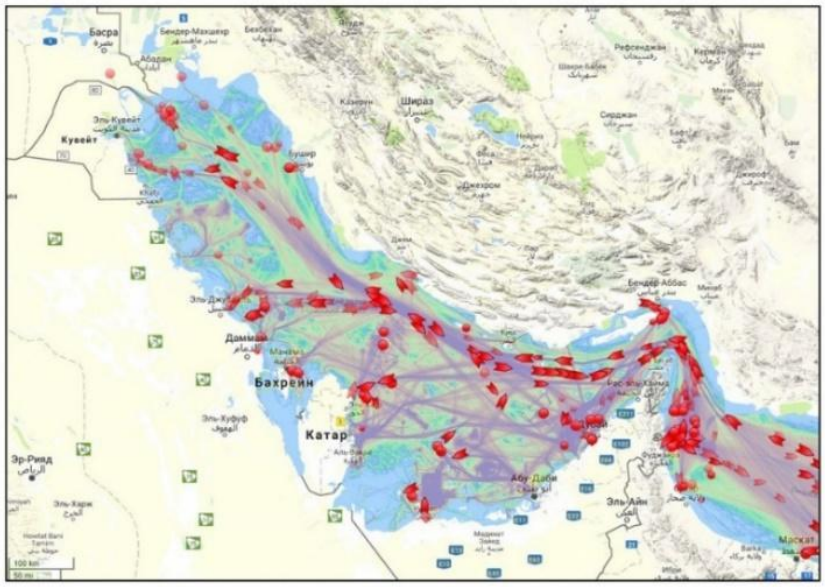

Fig. 2. The position of oil tankers in the Persian Gulf in 2018, © marinetraffic.com

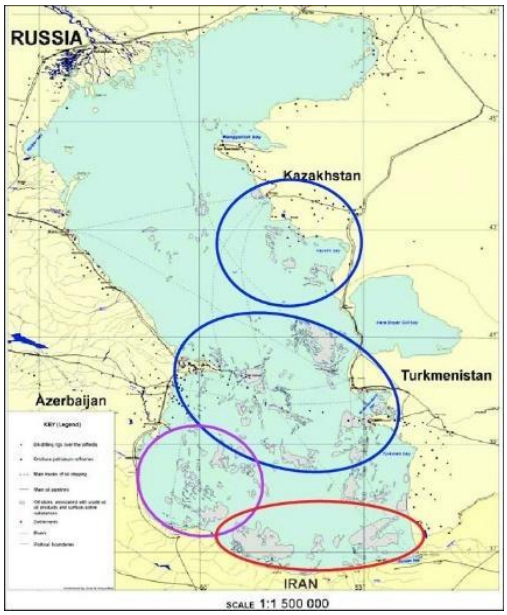

Fig. 3. Map of oil spills accumulation in the Caspian Sea areas related to crude oil in 1996, Ellipses show areas of oil slick accumulations over the oil production fields (blue), bottom seepages (violet) and river run-off (red), [10].

Oil spills and contaminations mainly occur in the main and secondary routes of vessels, tankers operation zones, as well as in ports or berthing regions (Fig. 4). Therefore, prevention and reduction of marine environment hazards are critical in the ports' operation. For addressing these issues, the Kuwait Regional Convention for Cooperation on the Protection of the Marine Environment from Pollution was held in Kuwait in 1978 with the participation of Iran, Saudi Arabia, Bahrain, the United Arab Emirates, and Oman (Kuwait Convention).

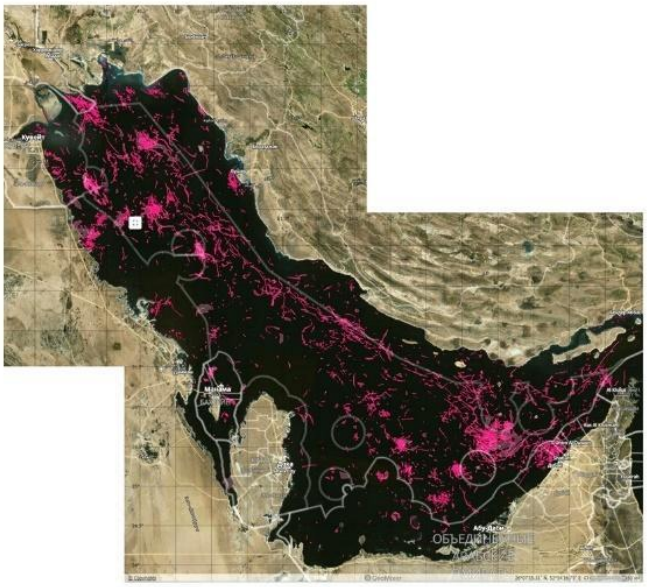

Fig. 4. Summary map of all oil spills detected in the Persian Gulf in 2017 on the Sentinel-1A and Sentinel-1B SAR images, © scanex.ru

Furthermore, due to the high operational cost of ports, the authorities should demonstrate to their investors and clients, their capabilities for the efficient operation of the equipment and traffic navigation.
Over the past decade, various models have been proposed to deal with efficiency such as Stochastic Frontier Analysis (SFA), Analytic Hierarchy Process (AHP), Analytic Network Process (ANP), Multiple-Criteria Decision Analysis (MCDA), Technique for Order of Preference by Similarity to Ideal Solution (TOPSIS), Fuzzy logic and Data Envelopment Analysis (DEA) which is based on weighted ratio of outputs to input and is useful for multi-criteria benchmarking studies. In this study, we evaluated and analyzed the efficiency in revenue generation of ports using Data Envelopment Analysis from two different modeling approaches; based on relating earnings to port operational capability and activity and based on land indicators, infrastructure, and equipment.

2. Data Envelopment Analysis Method

Data Envelopment Analysis (DEA) includes techniques and methods for assessing efficiency or measuring the productivity of decision-making units. The DEA is, in fact, the extension of Farrell's work in devising the first non-parametric method which measures productivity by considering a system of inputs and outputs. Using the inputs and outputs of the decision-making units and the principles governing them, Farrell [7] introduced a set called Production Possibility set and presented a part of its frontier as a production function. This frontier is also called the efficient frontier, and the decision-making units located on the frontier are considered efficient. But Farrell's method did not attract much attention until Charnes, Cooper, and Rhodes [5] established a method based on linear algebra.
The DEA offers many opportunities for collaboration between analysts and decision-makers. These collaborations can be efficient in selecting inputs and outputs of the units under evaluation, and functioning and modeling relative to the frontier. Efficiency means that each unit performs well under the influence of in-organizational indicators, expressed as the ratio of output to input (Fig. 5). In the case of multiple inputs and outputs for the decision-making unit, the ratio of the total weighted output to the total weighted input for the efficiency of that unit is measured [16].

$$Efficiency = \frac{\sum Output}{\sum Input} = \frac{u_1 y_1 + \cdots + u_s y_s}{v_1 x_1 + \cdots + v_m x_m}$$

The used notations can be described as follows:
x and y are the input and output vectors, respectively. u_s output weight and v_m input weight.

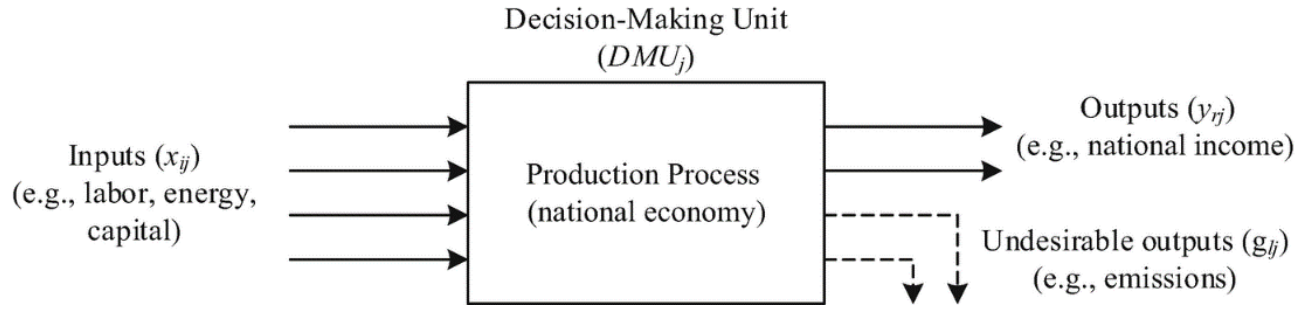

Fig. 5. The production process in a national economy, [9].

CCR (Charnes, Cooper and Rhodes) is the first DEA model to measure the efficiency of decision-making units presented by Charnes, Cooper and Rhodes in 1978. The number of data envelopment analysis models is increasing and is becoming more specialized [11]. But the basis of all DEA models are models with returns to the CCR constant scale and returns to the BCC (Bander, Charnes, Cooper) variable scale [13]. The DEA model can be divided in terms of being input- or output-oriented. Therefore, there are four general categories of DEA models:

- Constant returns to scale (CRS): Input-oriented & output-oriented
- Variable returns to scale (VRS): Input-oriented & output-oriented

In this study, the output-oriented CCR model is used to evaluate the efficiency of ports in terms of oil exchange and efficient units are ranked by AP method (Anderson, Peterson).

3. Output-Oriented CCR model

The name of this model is derived from the first letters of three scholars creating it, Charles, Copper and Rhodes. This model has a Constant Returns to Scale. Output-oriented models seek to increase or maximize outputs without increasing inputs or incremental resources. This model is shown in the following relation:

$$Max\ \varphi$$

$$\sum_{j=1}^{n} \gamma_j x_{ij} \le x_{io}, i = 1, \dots, n$$

$$\sum_{j=1}^{n} \gamma_j y_{rj} \ge \varphi y_{ro}, r = 1, \dots, s$$

$$\gamma_j \ge 0, j = 1, \dots, m$$

The used notations can be described as follows:
φ: Efficiency of the under investigated DMU in period p, m: Index of DMUs, n: Index of inputs, s: Index of outputs, p: Index of time periods, x: ith input of the jth DMU in period p, y: rth output of the jth DMU in period p, γ: Benchmark for the jth inefficient DMU in period p.
Using this model of DEA to calculate efficiency and rank units, more than one unit may obtain the highest efficiency coefficient i.e. 1 and become efficient. In this case, it is not possible to compare and rank these units in relation to each other and the AP method can be used for ranking.

4. Results and Discussion

The Anderson-Peterson model or the super efficiency method was proposed by Anderson and Peterson [1] makes it possible to determine the most efficient unit to rank efficient units. In this method, the score of efficient units can be greater than 1 and thus the efficient units will be ranked just like inefficient units. The methodology is to remove the DMU from the production possibility set and apply the model to other DMUs. The larger the unit coefficient, the more efficient it will be. If the model is output-oriented, the goal is to drive an inefficient unit to the efficiency frontier by keeping the output constant and reducing input. The Min function type is used in this study.

$$Min\ \theta$$

$$\theta x_{ip} \ge \sum_{j=1, j\neq p}^{n} \gamma_j\ x_{ij}\ , i = 1 \dots n$$

$$y_{rp}\ \le \sum_{j=1, j\neq p}^{n} \gamma_j x_{rj}\ , r = 1 \dots s$$

$$\gamma_j \ge 0, j = 1, \dots, m, j \neq p$$

The used notations can be described as follows:
θ: DEA efficiency, , m: Index of DMUs, n: Index of inputs, s: Index of outputs, p: Index of time periods, x: ith input of the jth DMU in period p, y: rth output of the jth DMU in period p, γ: Benchmark for the jth inefficient DMU in period p.

5. Literature Review

Chang [4] examined the efficiency of South Korean ports in terms of the environment. Using the Slacks Based Measure (SBM) and analysis of carbon dioxide data, he investigated the effect of reducing CO2 emissions on port efficiency.
Lee et al., [12], addressed the environmental efficiency of port cities affected by air pollution. By applying the SBM method and considering the Gross Regional Domestic Product (GRDP) as the model output, they investigated the role of air pollutants in the economic productivity of the port cities like Singapore, Busan, Rotterdam, Kaohsiung, Antwerp, and New York.
Cheon et al., [6] analyzed the relationship between environmental and economic efficiency of 10 important ports of the United States using data envelopment analysis and found a close link between environmental efficiency and port economic productivity.
Zahran et al., [19] analyzed the efficiency of port authorities in terms of monetization mechanism using two different modeling approaches, activity and infrastructure.
Grigoroudis and Petridis [9] used DEA method to estimate countries' environmental efficiency using slack-based model under the consideration of constant returns to scale and variable returns to scale method.
Mahmoudi and Emrouznejad [14] presented a literature review and classification of the applications of DEA in transportation systems by classifying 40 papers from 2007 to 2018. In this paper the origins of DEA in transportation problems have been reviewed and development of DEA applications have been presented.

6. Data and Variables

In this study, the efficiency of 12 ports in the Persian Gulf, Oman and Caspian seas (Fig. 6) from 2016 to 2018 are examined using DEA. Each of the ports is considered to be a decision-making unit that generates output by consuming inputs.

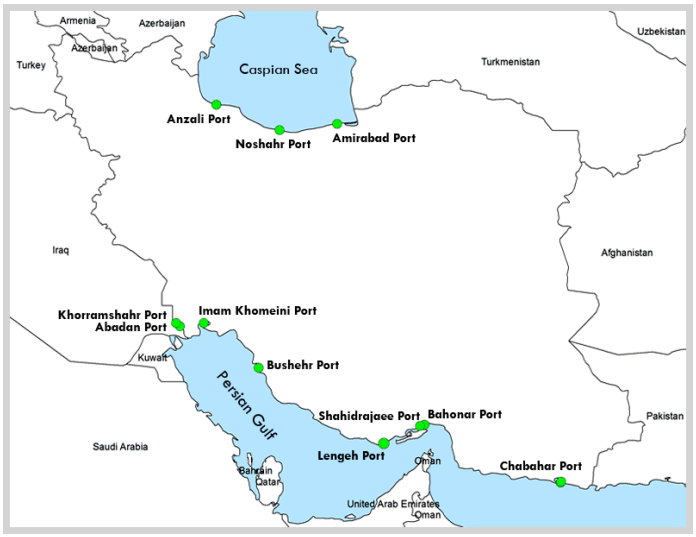

Fig. 6: Iranian ports, © pmo.ir

In this study, the most important and effective inputs and outputs for measuring the efficiency of oil ports are selected as shown in Table 1. A total of six input variables and one output variable is considered. The collected data shown in Tables 2-4 are gathered from the Ports and Maritime Organization of Ministry of Roads and Urban Development. It should be noted that the ports areas are modeled without considering the area of pack stations and roofed warehouses. It is noted that since the input and output indices of the model have different units the data is first descaled by dividing the values for each index by the sum of its values to obtain the weight ratio of each index.

Table 1. Input and output variables

Inputs	Outputs
Port and Hinterland Area (ha)	Import/Export of Petroleum Products (ton)
Number of Oil Jetties (posts)	
Total Length of Oil Jetties (m)	
Basin Depth (m)	
Capacity of Oil Jetties (ton)	
Number of Tugboats	

Table 2. Ports input and output data in 2016

Ports	Inputs						Outputs
	Area	**Jetties**	**Length**	**Depth**	**Capacity**	**Tugboats**	**Loading**
Abadan	6	1	136	5	5000	1	641
AmirAbad	1060	2	430	6	12000	5	41749
Anzali	132	1	183	5.5	5000	6	80231
Bushehr	27	1	250	11	25000	7	781680
Chabahar	270	1	265	14	80000	4	1055540
FereydunKenar	69	1	90	5	5000	1	38821
ImamKhomeini	1100	5	910	14	186000	11	18544165
Khorramshahr	182	1	30	5	1000	5	32
Lengeh	20	1	240	5.5	3000	1	1652
Qeshm	25	1	260	18	100000	2	100365
ShahidBahonar	15	2	335	10	10000	2	544346
ShahidRajaee	2400	9	520	12	150000	9	26116329
Total	**5306**	**26**	**3649**	**111**	**582000**	**54**	**47305551**

Table 3. Ports input and output data in 2017

Ports	Inputs						Outputs
	Area	**Jetties**	**Length**	**Depth**	**Capacity**	**Tugboats**	**Loading**
Abadan	7	1	136	5	5000	1	72
AmirAbad	1060	2	430	6	12000	5	38845
Anzali	132	1	183	5.5	5000	6	99498
Bushehr	27	1	250	11	25000	7	453435
Chabahar	270	1	265	14	80000	4	756811
FereydunKenar	69	1	90	5	5000	1	71705
ImamKhomeini	1100	5	910	14	186000	6	17771763
Khorramshahr	182	1	30	5	1000	4	120
Lengeh	20	1	240	5.5	3000	1	981
Qeshm	25	1	260	18	100000	2	108680
ShahidBahonar	16	2	335	10	10000	2	473783
ShahidRajaee	2400	9	520	12	150000	7	27139552
Total	**5308**	**26**	**3649**	**111**	**582000**	**46**	**46915245**

Table 4. Ports input and output data in 2018

Ports	Inputs						Outputs
	Area	**Jetties**	**Length**	**Depth**	**Capacity**	**Tugboats**	**Loading**
Abadan	7	1	136	5	5000	1	308
AmirAbad	1060	2	430	6	12000	5	26834
Anzali	132	1	183	5.5	5000	6	35113
Bushehr	27	1	250	11	25000	8	755899
Chabahar	270	1	265	14	80000	4	1098737
FereydunKenar	69	1	90	5	5000	1	29143
ImamKhomeini	1100	5	910	14	186000	6	16725342
Khorramshahr	230	1	30	5	1000	4	271
Lengeh	20	1	240	5.5	3000	1	811
Qeshm	25	1	260	18	100000	2	121577
ShahidBahonar	16	2	335	10	10000	2	461089
ShahidRajaee	3260	9	520	12	150000	12	25051546
Total	**6216**	**26**	**3649**	**111**	**582000**	**52**	**44306670**

Tables 5-7 provide a summary of descriptive statistics of variables. in this study. The average Port and Hinterland Area was 442 (ha) ranging between 6 and 2400 (ha). The average values of Basin Depth and Number of Oil Jetties (posts) were 9 (m) and 2 (Post), respectively. The ports Jetties handled 48500 vessel tons on average, whereas they have 4.5 tugboats. As for the output variable, the Import/Export of Petroleum Products was averaged at 3942129 (ton) with the maximum being 26116329 (ton) and minimum 32 (ton).

Table 5. Descriptive statistics of input and output variables in 2016

Variables	Units	Average	Maximum	Minimum	Standard Deviation
Port and Hinterland Area	Hectare	442.166	2400	6	730.982
Number of Oil Jetties	Post	2.166	9	1	2.443
Total Length of Oil Jetties	Meter	304.083	910	30	234.508
Basin Depth	Meter	9.25	18	5	4.530
Capacity of Oil Jetties	Ton	48500	186000	1000	64823.536
Number of Tugboats	Vessels	4.5	11	1	3.3166
Import/Export of Oil	Ton	3942129.25	26116329	32	8746455.71

Table 6. Descriptive statistics of input and output variables in 2017

Variables	Units	Average	Maximum	Minimum	Standard Deviation
Port and Hinterland Area	Hectare	442.333	2400	7	730.875
Number of Oil Jetties	Post	2.166	9	1	2.443
Total Length of Oil Jetties	Meter	304.083	910	30	234.508
Basin Depth	Meter	9.25	18	5	4.530
Capacity of Oil Jetties	Ton	48500	186000	1000	64823.536
Number of Tugboats	Vessels	3.833	7	1	2.367
Import/Export of Oil	Ton	3909603.75	27139552	72	8893317.32

Table 7. Descriptive statistics of input and output variables in 2018

Variables	Units	Average	Maximum	Minimum	Standard Deviation
Port and Hinterland Area	Hectare	518	3260	7	948.269
Number of Oil Jetties	Post	2.166	9	1	2.443
Total Length of Oil Jetties	Meter	304.083	910	30	234.508
Basin Depth	Meter	9.25	18	5	4.530
Capacity of Oil Jetties	Ton	48500	186000	1000	64823.536
Number of Tugboats	Vessels	4.333	12	1	3.339
Import/Export of Oil	Ton	3692222.5	25051546	271	8233720.75

7. Model Implementation

The Open Source DEA Project (© opensourcedea.org) is used to solve the data envelopment analysis model. As mentioned earlier, the Output-Oriented, Technical Efficiency and Constant Returns to Scale (RTS) method is used in this study (CCR_O). Technical Efficiency can be eliminated without changing the proportions between inputs and outputs. But Mix Efficiency can only be omitted by changing the proportion between inputs and outputs.

This DEA model attributes a virtual weight to each of input and output. Then the DMU performance is calculated using a linear optimization process which maximize each ratio by finding the best set of weight. The optimization process is imposed by existing data so that each dataset is compared against the best observed efficiency. The ports productivity assessment results for each year are shown in Table 8.

Table 8. Port Efficiency Factor

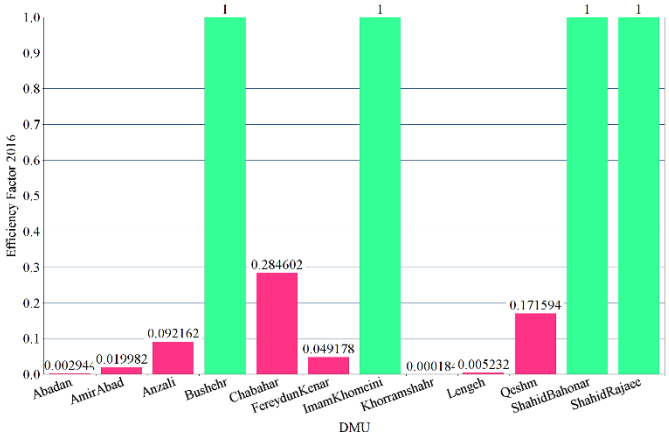

DMU Names	Objective Value	Efficient
Abadan	0.003	
AmirAbad	0.02	
Anzali	0.092	
Bushehr	1	Yes
Chabahar	0.285	
FereydunKenar	0.049	
ImamKhomeini	1	Yes
Khorramshahr	0.0	
Lengeh	0.005	
Qeshm	0.172	
ShahidBahonar	1	Yes
ShahidRajaee	1	Yes

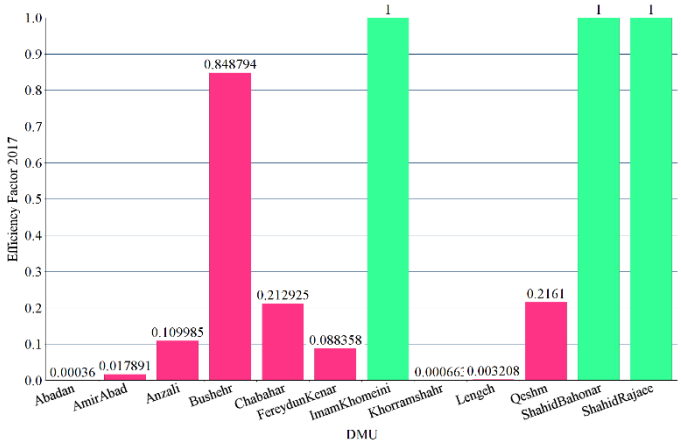

DMU Names	Objective Value	Efficient
Abadan	0.0	
AmirAbad	0.018	
Anzali	0.11	
Bushehr	0.849	
Chabahar	0.213	
FereydunKenar	0.088	
ImamKhomeini	1	Yes
Khorramshahr	0.001	
Lengeh	0.003	
Qeshm	0.216	
ShahidBahonar	1	Yes
ShahidRajaee	1	Yes

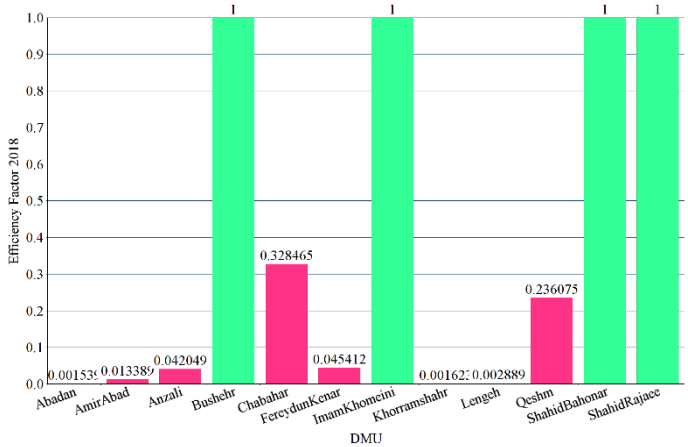

DMU Names	Objective Value	Efficient
Abadan	0.002	
AmirAbad	0.013	
Anzali	0.042	
Bushehr	1	Yes
Chabahar	0.328	
FereydunKenar	0.045	
ImamKhomeini	1	Yes
Khorramshahr	0.002	
Lengeh	0.003	
Qeshm	0.236	
ShahidBahonar	1	Yes
ShahidRajaee	1	Yes

The Table 8 yields the following conclusions:
During 2016, 2017, and 2018, four Shahid Rajaee, Imam Khomeini, Shahid Bahonar and Bushehr ports had relatively better use of their resources than the rest, thus achieving better results and considered to be efficient (as shown by the green bars in Table 8).
Also, according to the super efficiency method, Shahid Rajaee and Imam Khomeini were identified as the most efficient ports, respectively.
On the other hand, Abadan inefficient port has had the least efficiency in 2016. In addition, Khorramshahr's inefficient port has been improved over these 3 years. On the contrary, Lengeh's inefficient port had a declining trend over the study period and had become more inefficient (as shown by the red bars in Table 8).

8. Conclusion

In this paper, the port productivity as a unit has been analyzed by comparing the amount of output produced in comparison to the amount of input using Data Envelopment Analysis from two different points of view; based on relating earnings to port operational capability and activity and based on land indicators, infrastructures, and equipment.
The proposed method to evaluate the performance can rank the ports with the same efficiency. The results of

this study showed that most of the ports in the Persian Gulf region had a relative efficiency in the field of petroleum products. On the other hand, a significant difference could be seen between the nominal capacity of acceptance of petroleum products of ports and the volume of oil product exchanges over the study period which could be attributed to the lack of competitive environment due to oil sanctions imposed on Iran's petrochemical industry.

On the other hand, the efficiency of the ports reflected the proper use and adherence of the country's maritime organizations to guidelines and conventions under the supervision of the International Maritime Organization (IMO) and the conduct of practical programs and regional maneuvers, as well as planning for dealing with contingency and emergency cases.

Subsequent studies can use more parameters as inputs and outputs to handle different combinations of evaluation factors, such as Proficiency of Operators and Personnel, Port Navigation Safety Information, Vessel Traffic Service (VTS), Hydrographic Surveys equipment and Nautical Charts, Port Accident Risk Assessment and so on.

9. References

[1] Andersen P., Petersen N. C. (1993). *A Procedure for Ranking Efficient Units in Data Envelopment Analysis*. Management Science, Volume 39, Issue 10, pp 1261-1264.

[2]. Asian Development Bank (2010). *Central Asia Atlas of Natural Resources*. © Asian Development Bank. https://think-asia.org/handle/11540/155. License: CC BY 3.0 IGO.

[3]. Bashkin V.N. (2006) *CASPIAN SEA ENVIRONMENTS. In: MODERN BIOGEOCHEMISTRY*: SECOND EDITION. Springer, Dordrecht

[4] Chang, Y.T. (2013). *Environmental efficiency of ports: A Data Envelopment Analysis approach, Maritime Policy & Management*: The flagship journal of international shipping and port research, Volume 40, Issue 5: Ports and the Environment, pp 467-478.

[5] Charnes. A., Cooper. W.W., Rhodes, E. (1978). *Measuring the Efficiency of Decision Making Units*. European Journal of Operational Research, Volume 2, Issue 6, pp 429-444.

[6] Cheon S., Maltz A., Dooley K. (2017). *The link between economic and environmental performance of the top 10 U.S. ports*, Maritime Policy & Management: The flagship journal of international shipping and port research, Volume 44, Issue 2, pp 227-247.

[7] Farrell, M. J. (1957). *The measurement of productive efficiency*. Journal of the Royal Statistical Society. Series A (General), Volume 120, No. 3, pp 253-290.

[8]. Gray W.O. (2012) *Accidental spills from tankers and other vessels*. In: Wardley-Smith J. (eds) The Prevention of Oil Pollution. Springer, Dordrecht.

[9] Grigoroudis E., Petridis K. (2019), *Evaluation of National Environmental Efficiency Under Uncertainty Using Data Envelopment Analysis, Understanding Risks and Uncertainties in Energy and Climate Policy*, Springer, Cham, pp 161-181.

[10] Grimaldi C. S. L., Casciello D., Coviello I., Lacava T., Pergola N. and Tramutoli V., *Satellite oil spill detection and monitoring in the optical range*, 2010 IEEE International Geoscience and Remote Sensing Symposium, Honolulu, HI, 2010, pp. 4487-4490. doi: 10.1109/IGARSS.2010.5651967.

[11]. Hosseinzadeh Lotfi, F., Jahanshahloo, G., Khodabakhshi, M., Rostamy-Malkhalifeh, M., Moghaddas, Z., Vaez-ghasemi, M. (2013). *A Review of Ranking Models in Data Envelopment Analysis*. Journal of Applied Mathematics. Hindawi. https://doi.org/10.1155/2013/492421.

[12]. Lee T., Yeo G.T., Thai V.V., (2014), *Environmental efficiency analysis of port cities: Slacks-based measure data envelopment analysis approach, Transport Policy*, Volume 33, pp 82-88.

[13]. Lai, H.H., Chang, K.H., Lin, C.L. (2019*). A Novel Method for Evaluating Dredging Productivity Using a Data Envelopment Analysis-Based Technique*. Mathematical Problems in Engineering. Hindawi. https://doi.org/10.1155/2019/5130835.

[14]. Mahmoudi, R., Emrouznejad, A., Shetab-Boushehri, S.N., Hejazi, S.R. (2020). *The origins, development and future directions of Data Envelopment Analysis approach in transportation systems*. Socio-Economic Planning Sciences. https://doi.org/10.1016/j.seps.2018.11.009.

[15]. Mottaghi, A. (2016). *Environmental geopolitics of the Caspian basin energy interactions*, Caspian Journal of Environmental Sciences, 14(1), 81-90. magiran.com/p1552452.

[16]. Nikfarjam, H., Rostamy-Malkhalifeh, M., Noura, A, (2018). *A New Robust Dynamic Data Envelopment Analysis Approach for Sustainable Supplier Evaluation*. Advances in Operations Research, Hindawi. https://doi.org/10.1155/2018/7625025.

[17]. Razavi, A. (1997). *Continental shelf delimitation and related maritime issues in the Persian Gulf*. Publications on Ocean Development, v. 29., Martinus Nijhoff Publishers, Boston.

[18]. Shammas, P. (2001). *Iran: Review of Petroleum Developments and Assessments of the Oil and Gas Fields*. Energy Exploration & Exploitation - ENERG EXPLOR EXPLOIT. 19. 207-260. 10.1260/0144598011492552.

[19] Zahran S.Z., Alam J.B., Zahrani A.H., Smirlis Y., Papadimitriou S., Tsioumas V. (2017), *Analysis of port authority efficiency using data envelopment analysis*, Maritime Economics & Logistics, Volume 19, Issue 3, pp 518–537.

INTERNATIONAL JOURNAL OF
COASTAL & OFFSHORE ENGINEERING
IJCOE Vol.5/No. 1/Spring 2020 (55-66)

Available online at: www. Ijcoe.org

A Study on the Structural and Formation of the Low-Level Jet Stream over the Northern Persian Gulf (Case study on sinking the Behbahan cargo vessel)

Mehri Hashemi Devin[1], Abbas Ranjbar*[2], Ebrahim Fattahi[2], Sara Karami[3], Saviz Sehat Kashani[3]

[1] *PhD student, Atmospheric Science and Meteorological Research Center (ASMERC), Tehran, Iran*
[2*] *Associate* Prof. *of Atmospheric Science and Meteorological Research (ASMERC), Tehran, Iran; aranjbar@gmail.com*
[3] *Assistant Professor, Atmospheric Science and Meteorological Research Center (ASMERC), Tehran, Iran*

ARTICLE INFO

Article History:
Received: 04 Nov. 2020
Accepted: 09 Dec. 2020

Keywords:
Low Level Jet
Persian Gulf
speed
Behbahan cargo vessel
WRF-ARW model
wind vertical profile

ABSTRACT

A strong low level jet (LLJ) in the northern region of the Persian Gulf (PG) observed on 5th Jun 2020 that sank the Behbahan cargo vessel. In this article, we have used the WRF-V3 model and reanalysis ERA5 data to study the vertical structure, diurnal variation and intensity of the LLJs. The aimed topography's region, the pressure gradient and the land-sea breeze are the essential key factors in analyzing the diurnal variation of the LLJ over the PG that is known as the Shamal wind. The low terrain height in the northern of the PG and Zagros Mountains channelized the northwest winds and increased the pressure gradient that increased the wind speed. The decreasing friction over the PG during nighttime and the differences in temperature and specific heat capacity between water and land cause an increase in the LLJ intensity. The LLJ's core 22-24 ms^{-1} was located over the study region in 925hPa on 4th and 5th June at 18 and 00 UTC respectively. Thereafter core's wind speed decreased to 10-14 ms^{-1}at 12UTC on 5th June. The mix-down of momentum from the LLJ level to the surface caused an increase in wind speed and wave height over the PG which sank the Behbahan cargo vessel at early morning of 5th June. The LLJ at some regions like Kuwait formed at lower heights (under 950 hPa) and at the other points LLJ formed at levels upper than 950 hPa during nighttime of 4th Jun to afternoon of 5th Jun.

1. Introduction

Low Level Jet Stream (LLJ) is a very strong flow at levels near the surface (in boundary layer) with strong vertical wind shear ($\partial\vec{V}/\partial z$) above and below of the core by wind speed more than 10 ms^{-1}. Some LLJs result from strong baroclinity like fronts and some others are from any specific synoptic system with a weak baroclinity. The LLJ's importance and its effects on turbulence, wind energy production, distribution of pollutants and dust, aviation safety, increasing the height of waves on the sea and ocean have studied (Bonner, 1968; Doyle and Warner., 1993; Whiteman et al., 1997; Colle and Novak., 2010; Rife et al., 2010; Hu et al., 2013; Berg et al., 2015; Vanderwende et al., 2015; Smith et al., 2019). Several mechanisms proposed to describe the occurrence and characteristics of LLJs in some parts of the world in previous studies.
The first theory was proposed by Blackadar (1957), who addressed LLJs which result from an inertial oscillation, and their importance for the development of nighttime inversions. A second theory was developed by Holton (1967), who noted that the development of diurnal wind variations due to the diurnal heating and cooling of sloping terrain could affect the LLJs' intensity, a theory that was later examined and discussed by Bonner and Paegle (1970).
By cooling the surface during nighttime, turbulent mixing stops, and the friction of the surface layer decreases significantly, so the middle and upper layer decouples from the surface. The balance between pressure gradient force and Coriolis force disrupts and this imbalance cause an inertial oscillation in wind and changes the geostrophic balance to super geostrophic wind and also increased wind speed at low level during nighttime (Markowski and Richardson., 2010). LLJ is primarily a thermal phenomenon and reaches heights where the vertical temperature profile forms an

inversion (e.g. Membery, 1983; Rao et al., 2003). Surface winds are mostly weaker or calm during night but upper winds could accelerate to LLJ or nighttime jet that increase to super geostrophic wind speed (Stull, 1988). LLJ over complex terrain in south of Iran is simulated (Liu et al, 2000). The result of the study about LLJ northerly jet on 12-14 Feb 1995 showed that this LLJ mobilized and transported dust from Lut desert to Oman Gulf and decreased visibility. Because of lack of the data and synoptic stations the WRF model is used to simulate the vertical cross section to study the wind of 120 days and dust storm activity over the Sistan basin (Alizadeh et al, 2014). The simulated jet cores in Yerevan are mostly located between 150 and 250 above ground with magnitudes varying from 12 to 21 ms^{-1}(Gevorgyan, 2018). The climatology of the LLJ in Dashte Kavir is studied by using ERA-I reanalysis data during 1979-2017 that the core of jet has been identified at 850 hpa (Vazifeh et al, 2018). There is a strong correlation between northerly wind and meridional pressure gradient in Lut desert which are the important factors. Cold air advection from high latitude and also pressure gradient are important to form the gap wind (Bidokhti et al, 2006). Mobarak.H and Gaffarian (2018) simulated the LLJ by using different boundary layer schemes in WRF-CHEM model and LLJ's effect on the Khuzestan local dust studied. They concluded that LLJ has a key role on dust emission over semi-arid and arid area. Results from some studies (Membery, 1983; Giannakopoulou, 2012) show that LLJs cross of the northern region of the PG that cause strong wind speed over the PG and its ports and also increase the height of the waves so detection LLJ, its intensity and the LLJ structure in our study region are very important. On Friday morning 05 Jun 2020, the strong wind speed over water of the north of the PG near to Iraq, Um-Qasr port, drown the Behbahan vessel with seven person (Fig.1). In this paper, the strong wind over the Persian Gulf and the role of LLJ would be studied.

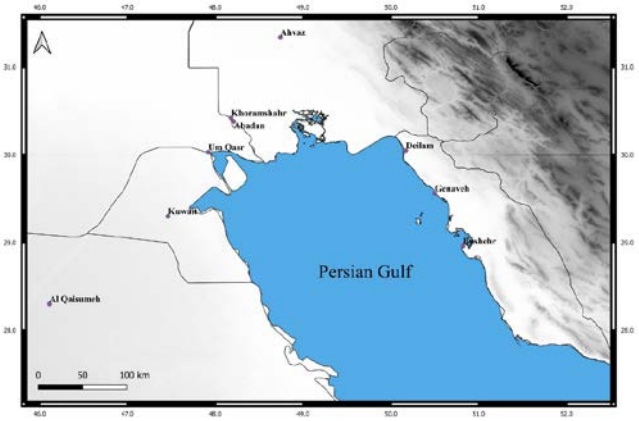

Figure 1. Topography map of the study area (PG)

2. Materials and methods

2.1. Study area

The northern of the PG is near-complex terrain with high and steep mountains, including the Zagros Mountains in Iran to the east (Fig.1), Kuwait in the west, and Khuzestan province in the north. Over the PG's complex terrain, diurnal mountain winds are generated by horizontal pressure differences that develop daily over the heated and cooled sloping terrain. It is thus apparent that the land–sea distribution (strong north-to-south pressure gradient) enhances the geostrophic wind speed that is vital factor. Boundary layer jets (BLJs), which are one type of low level jet, frequently occur next to a large mountain range or in regions with land–sea thermal contrast(Rife et al, 2010; Du et al,2015).

2.2. Materials

Synoptic stations data (temperature, humidity, wind direction, wind speed, etc.) of Khuzestan and Bushehr provinces and Kuwait station data from 3th to 6th Jun 2020 extracted from MCI[1]system. Ahvaz and Al-Qaisumah (the nearest stations to Um Qasr, a port city in southern Iraq) upper air sounding data are used to study instability indexes and wind shear from surface to upper. Kuwait didn't record upper data on 3th to 6th Jun 2020. Because of lack of upper air data and the importance of the study of upper wind to distinguish LLJ in the PG region, we have used the output data of the model to show vertical profile of wind in the study region. The model used for this LLJ event is the WRF (ARW) model, version 3.9. The model performed from 3th to 6th Jun 2020. The 37 sigma levels employed within 1000 to 100hPa. Two-step nesting (one-way) was applied using two model domains centered at 9 and 27 km spatial resolutions (Fig.2).

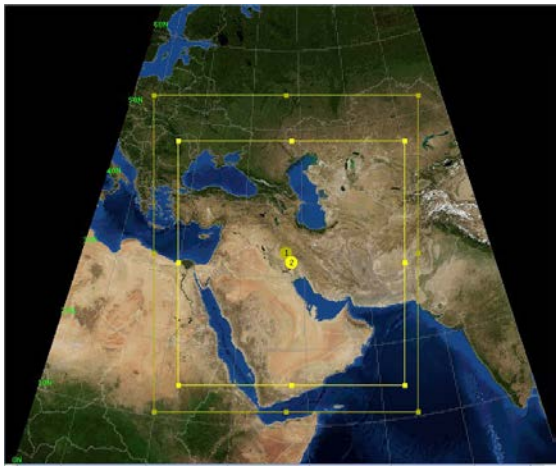

Figure 2. The WRF model domains with 9 and 27 km spatial resolutions (yellow dot indicates the centers of both domains located over the PG)

The selected schemes are widely used within the WRF community and have been shown to perform well over different regions. Like the unified Noah land-surface

[1] Meteorological Communication & Information

model scheme (Chen and Dudhia 2001), other physics was kept constant in the simulation. The WRF Single-Moment 3-Class Microphysics scheme (WSM3), Dudhia shortwave radiation scheme (Dudhia, 1989), Rapid Radiative Transfer Model (RRTM) longwave radiation scheme (Mlawer et al., 1997) have been selected. Mean sea level pressure, geopotential heights and wind fields in different levels were used from the model data and ERA5 data to study wind speed over our study region (PG and Um Qasr). To better identification the place of formation LLJ, some cross section of wind speed and potential temperature used. To identify the intensity and time of the LLJ formation vertical cross section of wind used.

3. Results and Discussion

3.1 Synoptic pressure patterns associated with LLJ

Figure 3 shows the surface pressure map and 10-m wind on 4-5 Jun 2020. The surface pressure pattern shows a low pressure system over the PG that its trough extends to the Khuzestan which form a north and northwesterly wind over the PG and Khuzestan. A upper-latitude thermal high system over the Zagros Mountains increased the lower pressure gradient over east and southeast of Khuzestan and increased the lower troposphere wind speed over northwest of Bushehr on 4th Jun 2020 morning (00UTC) (Fig3.a).
On 4th Jun at 12UTC, the maximum wind is located over north of Bushehr and northeast of the PG.
There is a high pressure system over west of Iraq that extends to the west of Iran. The high pressure system over the Zagros Mountains is stationary that cause a pressure gradient over Bushehr and Khuzestan (Fig.3, a, b). At 00 UTC on 5th Jun a low pressure system intensified as its central pressure reached less than 1004hPa and elongated to high latitudes where it was located over northeast of the PG and some parts of Bushehr. This pressure pattern would cause a northern and northwesterly winds (Fig.3.c).
The maximum 10-m wind speed is located over north of the PG and the wind speed over all northern parts of PG increased to 16 ms^{-1}during morning on 5th Jun. During 5th Jun's afternoon the pressure trough gradually extends to high latitudes over Khuzestan that caused the pressure gradient to decrease in the study area so the wind speed increased over Khuzestan and PG (Fig.3.d).
During afternoon time (12UTC) on 4th Jun at 925hPa level northerly wind speed increased sharply to 20ms^{-1} over most of the PG (Fig.4.a). There is a low pressure system over south of the PG and an upper high over most of Iraq area that causes northerly wind over southwest of Iran (Fig.4.a, b). On the night of 04th Jun (18UTC) the wind speed increased sharply to 26 ms^{-1} and the maximum of wind was located over north of the PG and northwest of Bushehr (Fig.4.c). During local early morning time on 05 Jun (00UTC) the maximum wind speed extended to a more extensive area and during afternoon time the wind speed decreased (Fig.4.d). Figure 5.a, b present the 850 hPa geopotential height and wind speed that are northerly over the study region and during evening local time (12, 18 UTC) the wind speed increased from 14 ms^{-1} to 20 ms^{-1}.

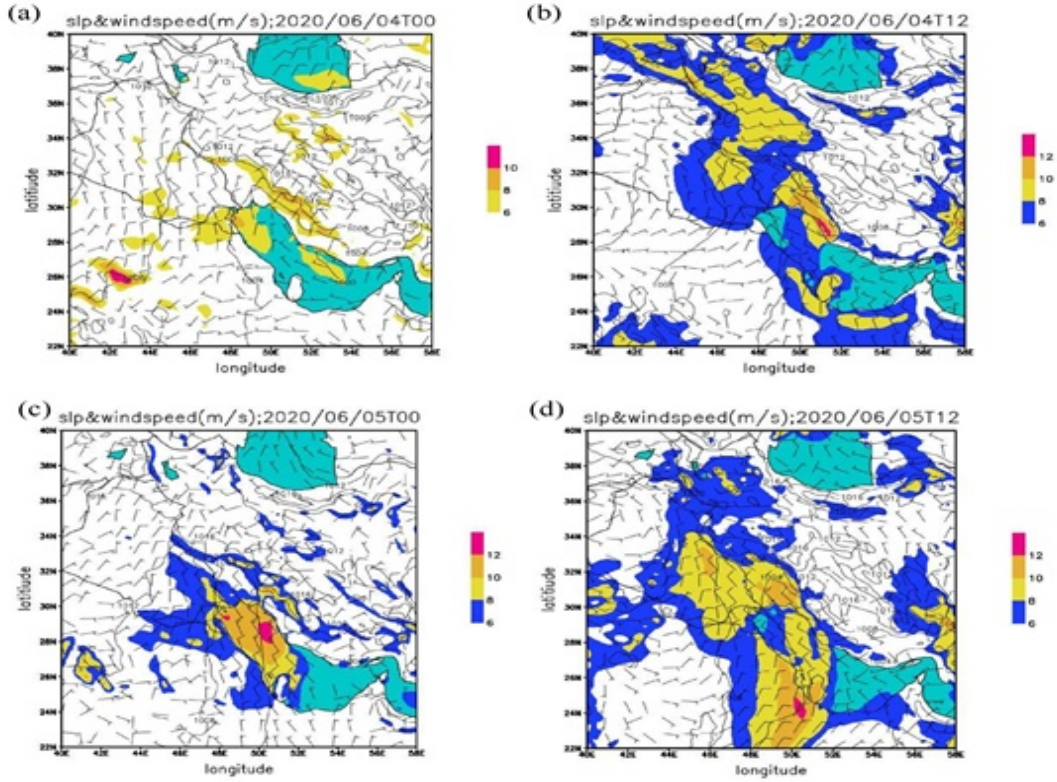

Figure3. Surface pressure and wind speed a) at 00UTC 4th Jun 2020, b) 12UTC 4th Jun 2020, c) 00UTC 5th Jun 2020, d) 12UTC 5th Jun 2020

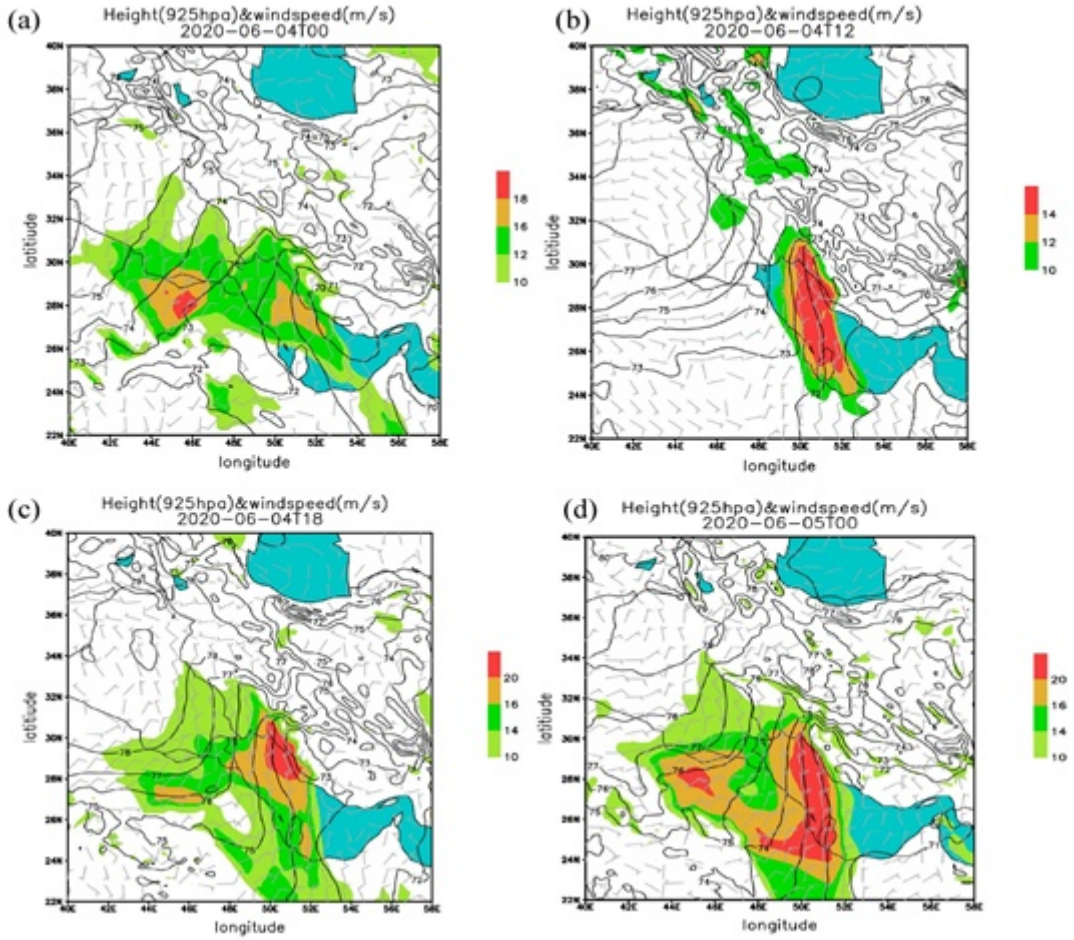

Figure 4. 925-hPa Geopotential height (gpdm) and wind speed (ms^{-1}) at, a) 00UTC 4th Jun 2020, b) 12UTC 4th Jun 2020, c) 18UTC 4th Jun 2020, d) 00UTC 5th Jun 2020

These patterns in comparison with 925 hPa the wind speed was weaker on 850 hPa and extended over the smaller area.

On the 700hPa level at 18 UTC the wind speed increased to 12 ms^{-1} over north of the PG compared to past hours (Fig.6.a b).

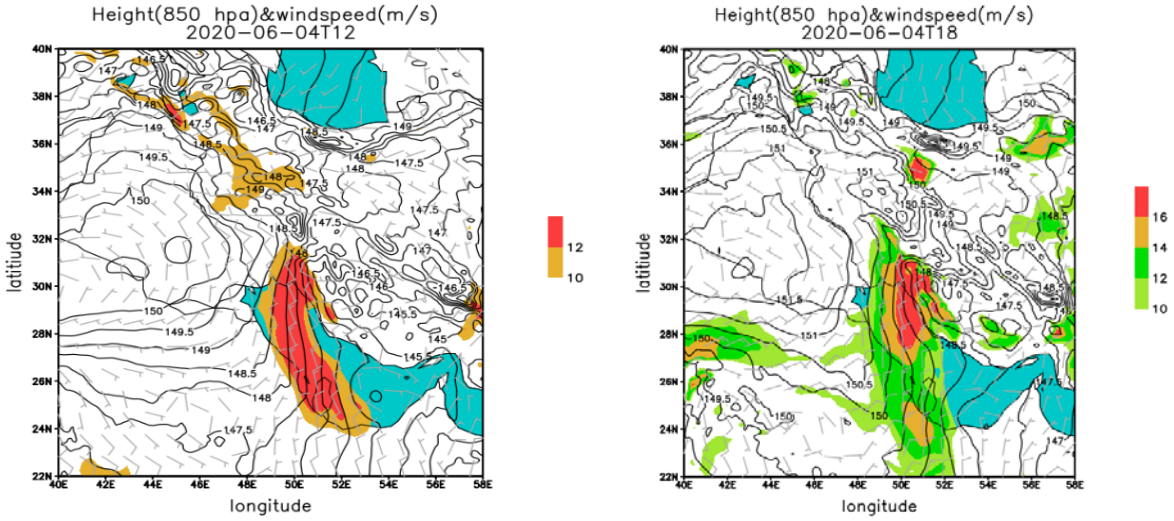

Figure 5. 850-hPa Geopotential height of (gpdm) and wind speed(ms^{-1}) at, a) 00UTC 4th Jun 2020, b) 12UTC 4th Jun 2020, c) 18UTC 4th Jun 2020, d) 00UTC 5th Jun 2020

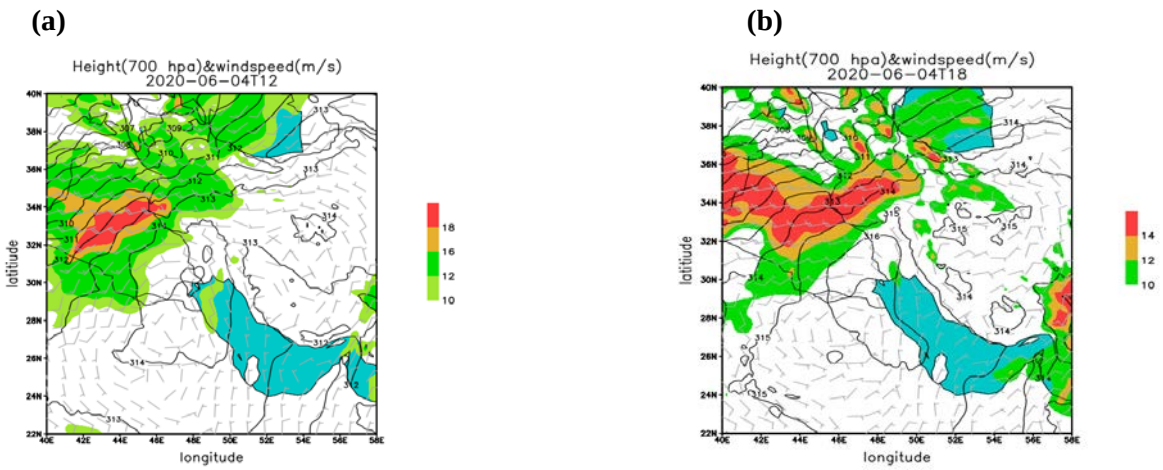

Figure 6.700- hPa Geopotential height (gpdm), wind speed (ms^{-1}) at, a) 12UTC 4th Jun 2020, b) 18UTC 4th Jun 2020

The wind speed decreased on the 700 hPa in comparison with the lower level. From the surface to mid-troposphere, the LLJ was remarkable on the 925 hPa. There was a semi-permanent anticyclone subtropical high over Iran at mid-troposphere levels that cause the southwesterly flow over north of the PG and the western of Iran (Fig.7.a).

In the study area the wind speed at the middle level decreased to 10 ms^{-1} (Fig.7.b). There was a deep trough at upper latitudes over Turkey and North West of Iran, which accompanied by strong wind speed more than 30 ms^{-1} (Fig.7.a, b).

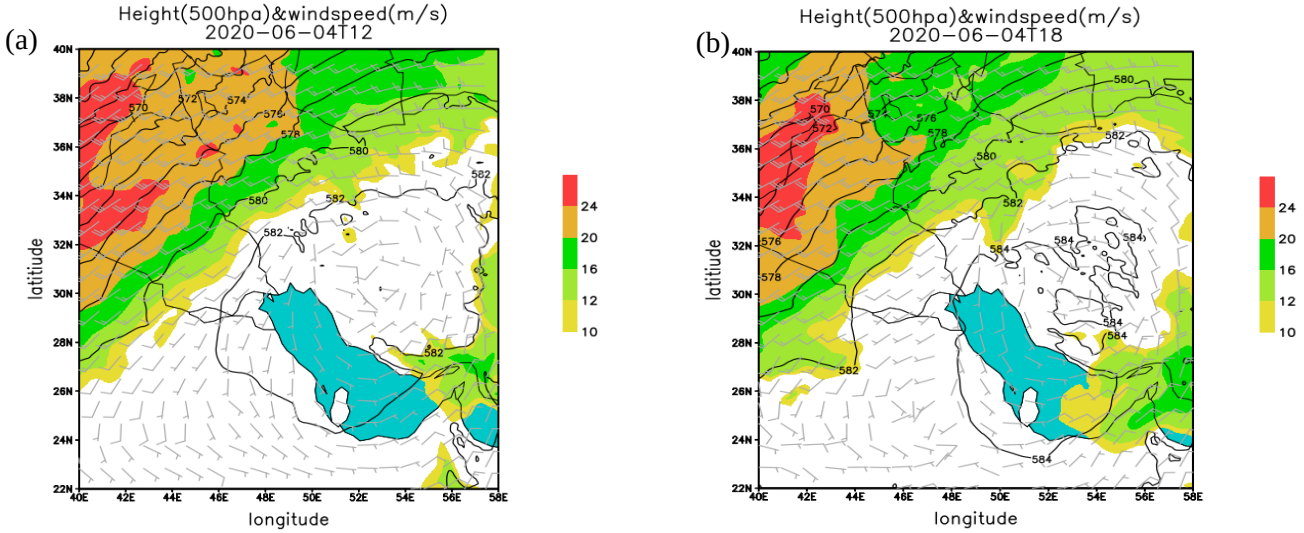

Figure 7. 500-hPa Geopotential height of (gpdm), wind speed (ms^{-1}), a) at 12UTC 4th Jun 2020, b) 18UTC 4th Jun2020

3.2. Vertical wind profile

To study wind speed variations at different levels and identify the level and position of LLJ, firstly upper air data of Ahvaz, Al Qaisumeh and Aldamam (not shown here) of Saudi Arabia studied which are the nearest upper air to the Um Qasr port. Kuwait station has not recorded data during our study period so the vertical wind profile of both stations and the ports near the PG prepared. Thermodynamic instability indices such as CAPE, CIN and KI had minimal value were used to study convective phenomena on 3th to 5th Jun 2020and there was no precipitation during the study period. The value of the CAPE and CIN was zero at both stations during the study period. The KI has increased to the maximum value of 19/9 at Al-Qaisumeh and 17 at Ahvaz station during afternoon on 4th Jun and early morning of 5th Jun.

Ahvaz station has recorded data only during afternoon time (12UTC). The wind (speed and direction) shear at lower level can see very well. Figure 10 shows the wind speed at Al- Qaisumeh increased at the 900 hPa to 800 hPa level and then decreased at the levels upper than 800 hPa during afternoon on 4th Jun and 5th Jun that show the formation of LLJ. The wind direction changed backward in this shallow layer (from 900 hPa to 800 hPa), which indicates cold advection (Fig.8.d).

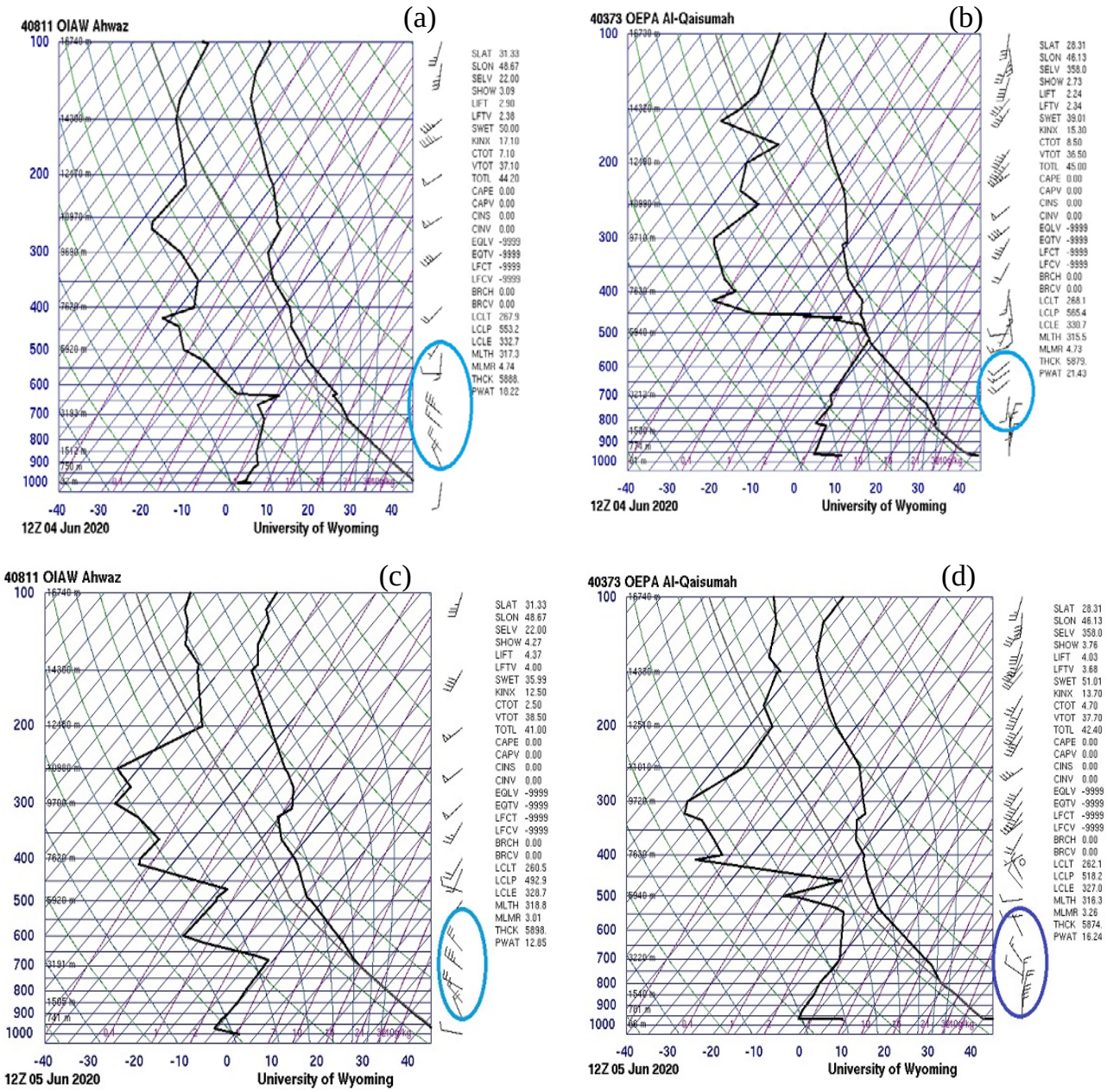

Figure 8. Skew-T diagram of a) Ahvaz and b) Al-Qaisumeh station at 12UTC 4th Jun and12UTC 5th Jun (respectively c, d)

Figure 9 shows vertical wind profile at 00 UTC on 4th and 5th Jun over Deilam by using the WRF model output that shows LLJ at 925 hPa level. The negative values of meridional speed show northerly flow. LLJ develops at 950 hPa with more wind speed compared with the Ahvaz profile (not shown here) and the LLJ speed reached 22 ms^{-1} during early morning on 5th Jun and night of 4th Jun (18UTC).

During afternoon time on 5th Jun the wind speed decreased. At Genaveh port the LLJ exists at 925 hPa with the maximum wind speed 20 ms^{-1} (Fig.10). There is a significant difference between Kuwait wind speed profile during morning and afternoon time at the selected period. The nightly LLJ is clear at 975 hPa (Fig.11).

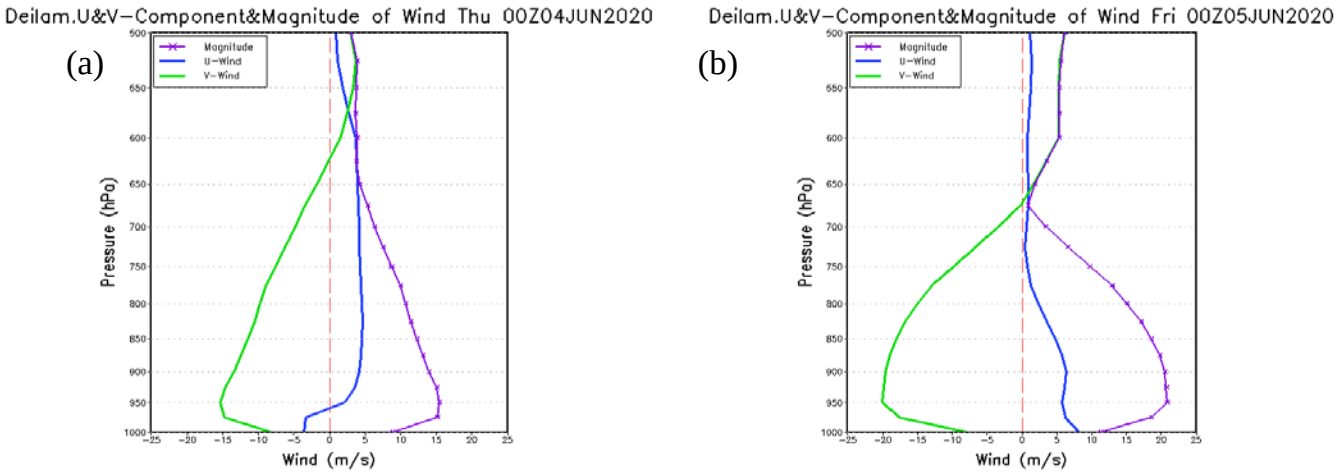

Figure 9. Deilam vertical profile of zonal wind component (blue color), meridional wind component (green color) and wind speed magnitude (purple color) at 00UTC on a) 4th Jun 2020, b) 5th Jun 2020

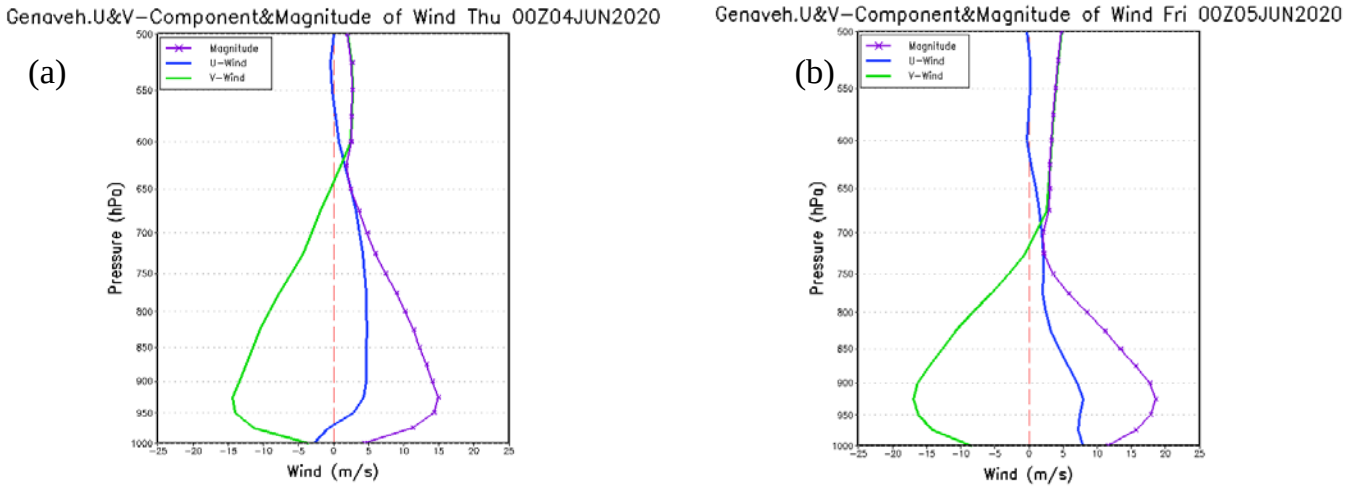

Figure 10. Genaveh vertical profile of zonal wind component (blue color), meridional wind component (green color) and wind speed magnitude (purple color) at 00UTC on a) 4th Jun 2020, b) 5th Jun 2020

The LLJ at Bushehr existed at 925 hPa level during morning time on 4th Jun and then it existed with larger wind speed at lower level 975 hPa during afternoon and nighttime (12 and 18 UTC) (Fig.12).

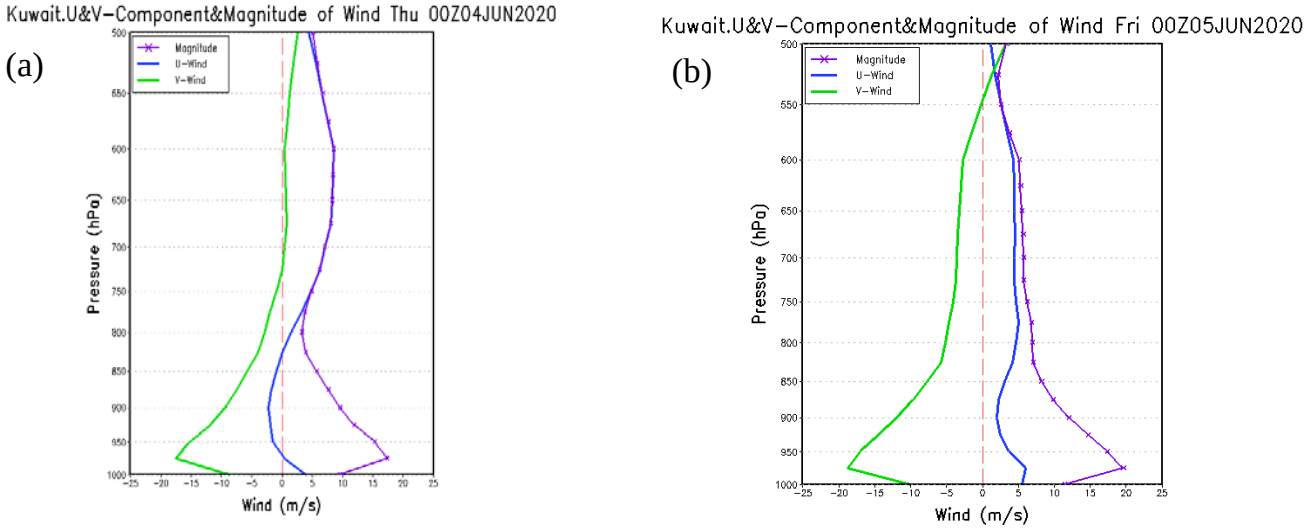

Figure 11. Kuwait vertical profile of zonal wind component (blue color), meridional wind component (green color) and wind speed magnitude (purple color) at 00UTC on a) 4th Jun 2020, b) 5th Jun 2020

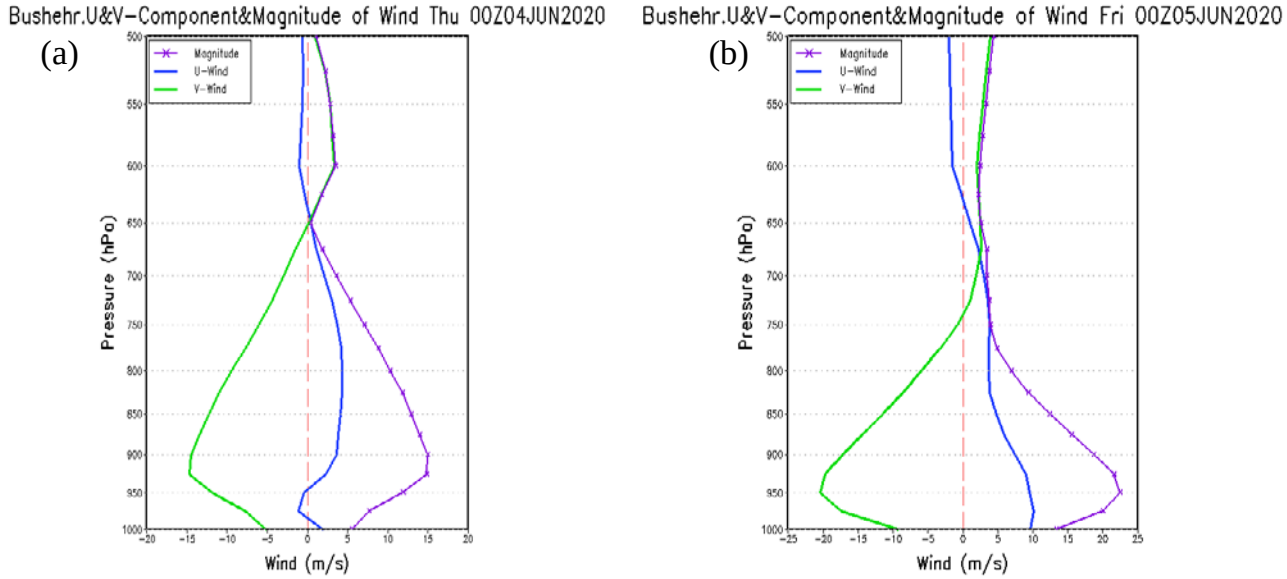

Figure 12. Bushehr vertical profile of zonal wind component (blue color), meridional wind component (green color) and wind speed magnitude (purple color) at 00UTC on a) 4th Jun 2020, b) 5th Jun 2020

3.3. Vertical cross-section of the wind speed and potential temperature

To better identify LLJ the variations in wind speed from surface to 700 hPa level by some cross sections over the study area have investigated. The first cross section crosses from Kuwait to the PG and north part of Bushehr (line AB at Fig.13). On 4th Jun 2020 (00UTC) the maximum wind speed (15 ms^{-1}) located over east of the PG and the minimum of the potential temperature 34°C is over surface and the PG (Fig.13.a). At 12 UTC on 4th Jun, increasing potential temperature have seen particularly over land because of difference between specific heat capacity of water and land. These differences between land and water's temperature and also the heat capacity are equivalent to the sensible heat flux that caused an increase in baroclinicity and is a helpful factor in increasing LLJ wind speed in the study area.

The maximum wind speed of 17 ms^{-1} can be seen over the east of PG and Bushehr from 975 hPa to 850 hPa. The heating during day time, increasing vertical motions and increasing of the mixing layer height cause the maximum wind speed extends to the upper level (850hPa) (Fig.13.b). At 18 UTC LLJ wind speed increased to 21 ms^{-1} that was the maximum value during the past 24 hours and limited to the lower level. (From 975 hPa to 900 hPa) (Fig.13.c). There is a minimum wind speed at 850 hPa and the upper level. In the early morning on 5 Jun, LLJ, with the maximum speed of 21 ms^{-1} can be seen from the level below 950 hPa to the upper than 950 hPa (Fig.13.d). Potential temperature increased by approaching the mountain that it shows decreasing in static stability and increasing in wind speed. The second cross section is over north of Bushehr to Um Qasr and Kuwait (line CD) that shows the maximum wind speed 15 ms^{-1} during afternoon time on 4th Jun because of boundary layer turbulent mixing from 975 hPa to upper altitudes(Fig.14.a, b).

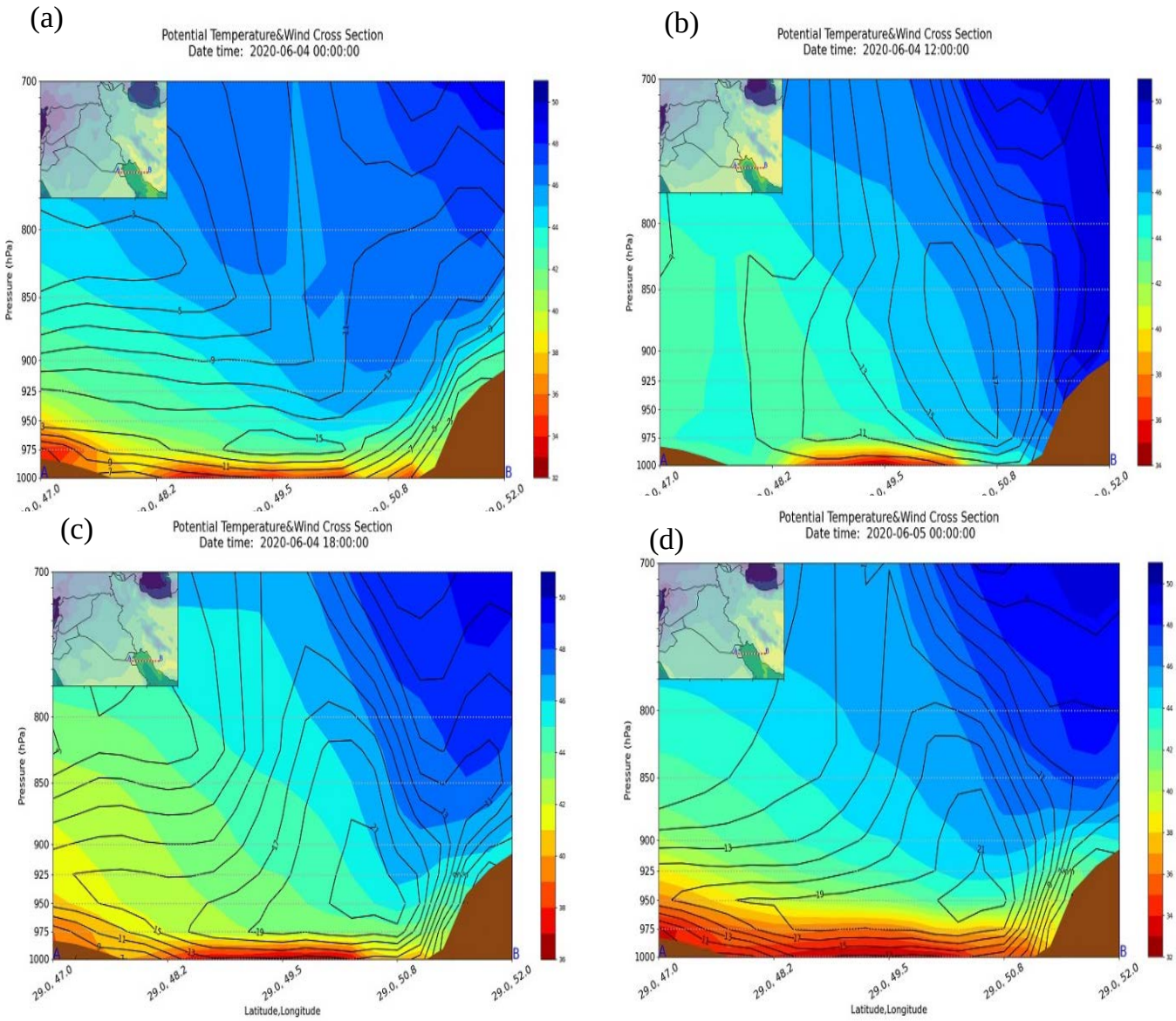

Figure 13. Vertical cross-sections of wind speed (black contour, m s^{-1}) and potential temperature (shaded, C) over PG along the line from A to B from 00UTC 2020-06-04 to 00UTC on 2020-06-05(respectively a to d)

At the night of 4th Jun, the maximum speed of LLJ's core reached to 17 ms^{-1}. At early morning of 05 Jun the core speed increased to 19 ms^{-1} and cover larger area but only around 950 hPa (Fig.14.c, d). Adiabatic changes in temperature cause decreasing in potential temperature during nighttime of 4th Jun and early morning of 5th Jun (Fig.14.c, d). As discussed at synoptic patterns, the pressure systems caused northerly flow over southwest of Iran and PG that figure 15 shows the vertical diagrams over some places near to Um Qasr (the position which Behbahan cargo vessel sank) such as Deilam port and Abadan, Bushehr, Genaveh port, Khorramshahr, Kuwait are not shown here (Fig.15).

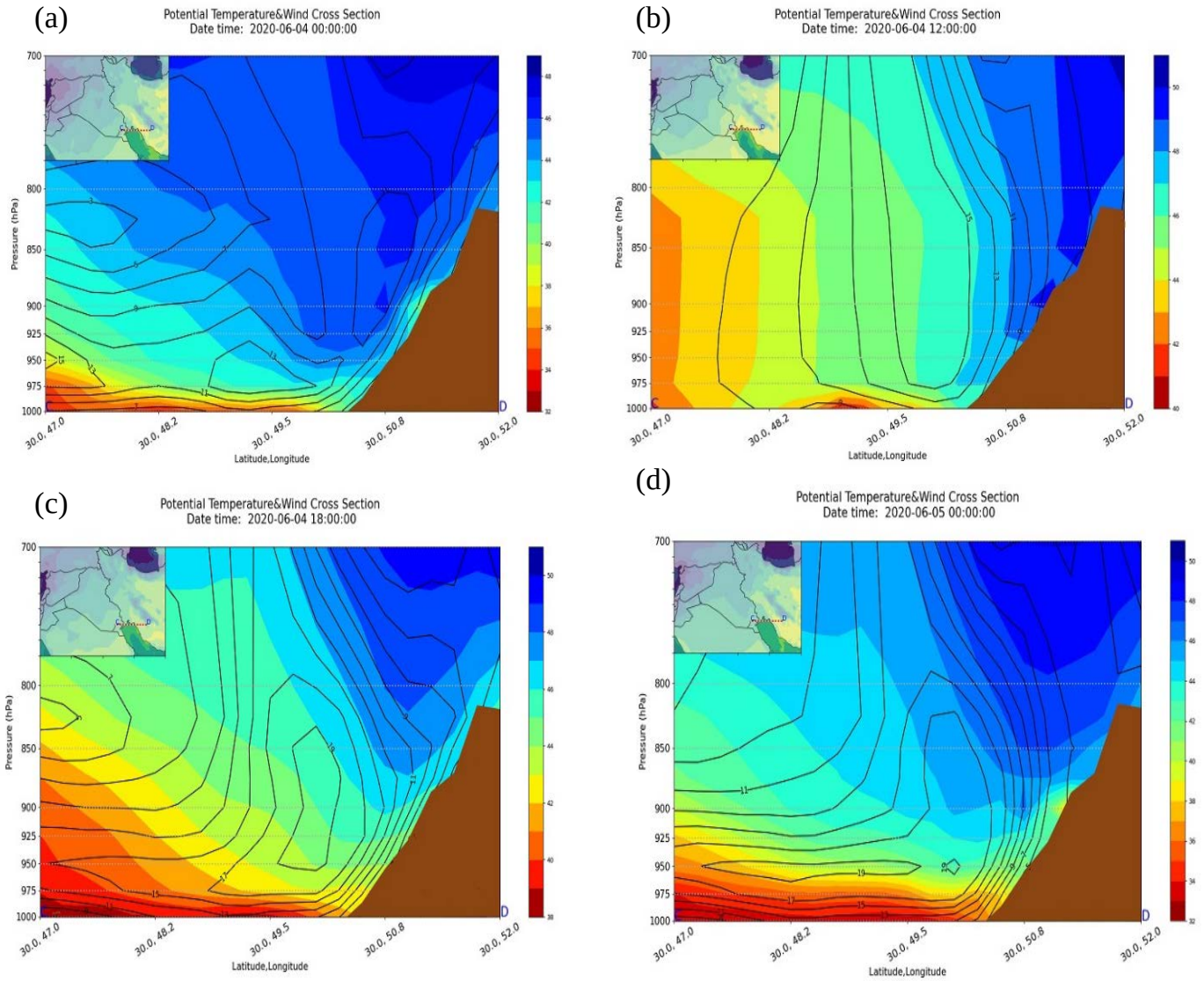

Figure 14. Vertical cross-sections of wind speed (black contour, m s^{-1}) and potential temperature (shaded, C) over PG along the line from C to D from 00UTC 2020-06-04 to 00UTC on 2020-06-05(respectively a to d)

These diagrams show the formation of LLJ by the maximum wind speed 25ms^{-1} from 975 hPa level to 950 hPa and then decreasing at upper levels. The maximum wind speed of the LLJ formed over northern part of the PG such as Bushehr and Genaveh port. By using model output data, the vertical profile of wind speed and the time of formation of LLJ (night of 4th Jun and early morning of 5th Jun with the maximum speed 18 ms^{-1} at 950 hPa level) over Kuwait and Abadan shown. The other diagrams also show the same time for the LLJ formation. (Fig.16). LLJ formed at lower level at Kuwait, Bushehr, Abadan and Ahvaz but at Deilam port and Genaveh port LLJ formed at the level upper than 950 hPa near to the 850 hPa (Fig.16).

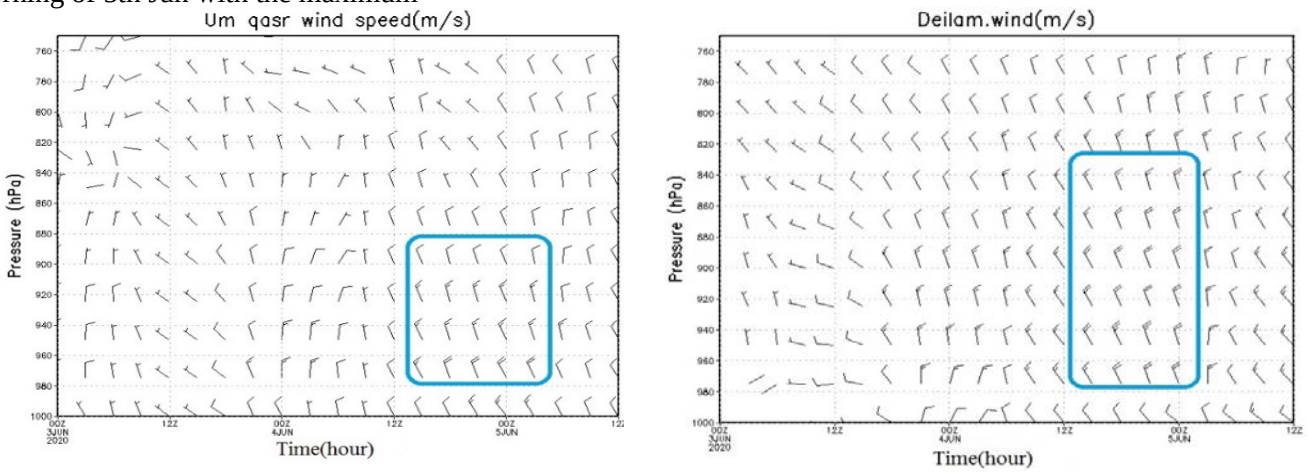

Figure 15. Vertical profile of wind speed (m s^{-1}) over some points of the study area from 2020-06-03 to 12UTC of 2020-06-05

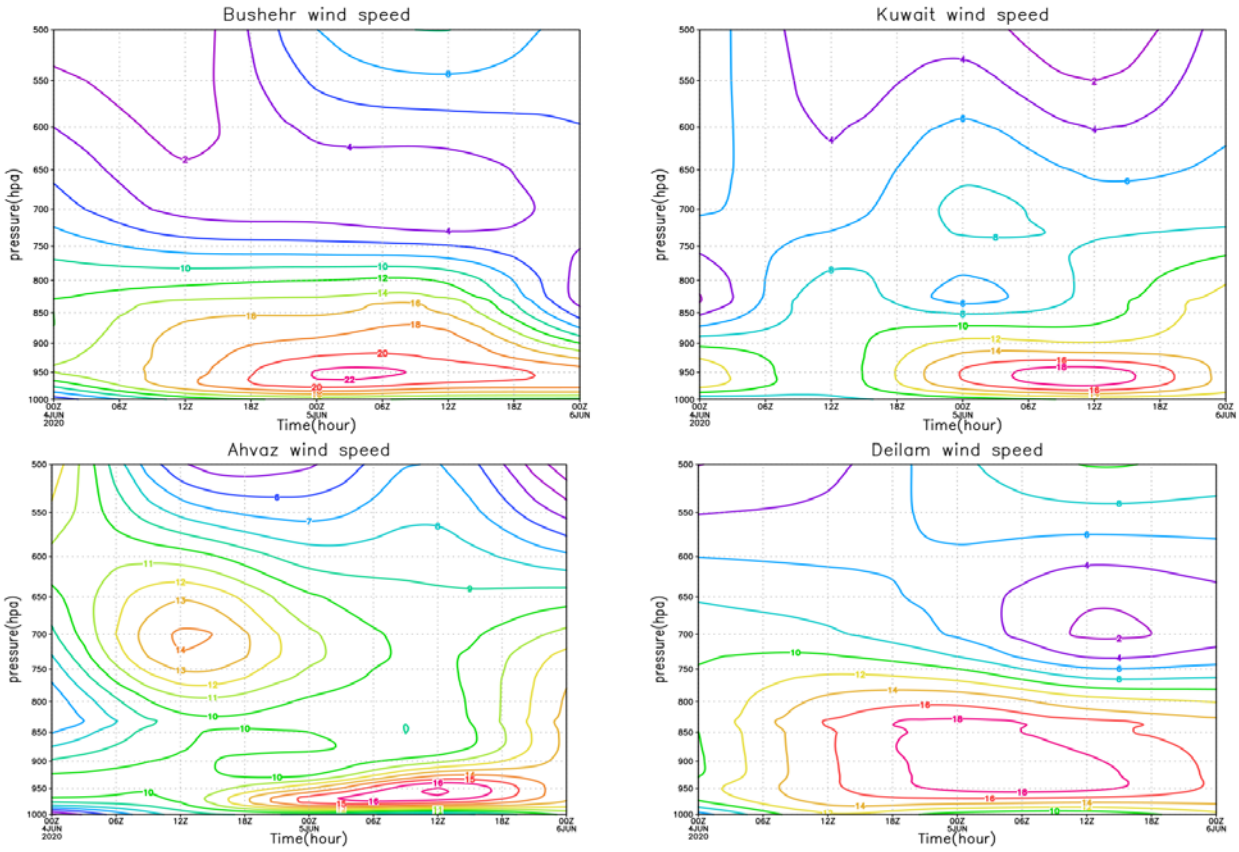

Figure 16. Time cross section of wind speed (m s^{-1}) over some points of our study area from 2020-06-03 to 12UTC of 2020-06-05

4. Conclusions

Mesoscale LLJs over southwest of Iran and Northern the PG (NPG) are essential in rippling NPG and shipping. Throughout the nighttime in the warm season, because of cooling and decreasing turbulent mixing layer's height, the decoupling of surface layer from boundary layer occurs, which reduces friction and increases the wind speed at upper level than surface layer. At surface pressure pattern, there is a high system over the Zagros mountain area that increases to its maximum 1016 hPa during LLJ formation time. A low pressure system 1004 hPa forms simultaneously over south of the PG that a deep surface trough extends northward to the north of the PG and Khuzestan that causes an increasing in the east- west pressure gradient. At 925 hPa, the pattern looks like to the surface map and there is a low system over the PG that its trough extends to the north of the PG. A high system forms east of the Mediterranean Sea that its ridge extends to the west of Iran and then gradually extends to the east and the trough extends to higher latitudes that simultaneously increased pressure gradient over the study area and increased wind speed from nighttime of 4th Jun to 5th Jun. At 850 hPa the pattern is similar to the 925 hPa level, but by less instability which geopotential gradient is weak so the wind speed is also weak. At the upper levels the instabilities going weaker so the best level at which the LLJ formed was 925 hPa. Ahvaz's Skew-T diagrams (12UTC) showed northwesterly winds with an intense speed at the lower than 700 hPa level. The LLJ can be seen at 925 hPa at Al-Qaisumah and Al-damam port. The instability indexes like CIN, CAPE, were very low. The KI has had a little increase during nighttime of 4th Jun and morning of 5th Jun. The study of anomaly of surface wind speed shows increasing anomaly during the time of the LLJ formation that the maximum value 6 ms^{-1} was on 5th Jun morning. LLJ has formed mostly at altitudes from 975 to 950 hPa. The maximum wind speed of the LLJ was over Bushehr shores especially Bushehr and Genaveh 22 ms^{-1} and 20 ms^{-1} respectively during nighttime (18 UTC) 4th Jun and 5th Jun morning (00UTC). The cross section of wind speed and potential temperature show increasing of wind speed during the LLJ formation's time that because of the weakness of the turbulent mixing the increasing of wind speed happens at the lower levels while during morning and afternoon time the turbulent mixing increases and the wind speed decreases. Time cross sections showed that the LLJ at some regions like Kuwait, Bushehr and Abadan formed at lower heights (under 950 hPa) and at the other points formed at upper levels (950 hPa to 850 hPa) but LLJ in the study area formed during nighttime of 4th Jun to afternoon of 5th Jun 2020. Due to the low height of LLJs, the momentum transmit to the surface quickly, significantly during morning time which causes increasing the surface wind speed, the wave height over the PG and the disturbances in vessels and boats movement. Temperature differences and specific heat

capacity difference between land and sea over the PG are the other factors that cause baroclinicity and form the LLJ. Behbahan vessel sank during the early morning of 5th Jun because of the formation of LLJ.

Acknowledgment

We are appreciative of helps and very valuable comments of Mr. Mostafa Hadizadeh (North Khorasan Meteorological Administration).

5. References

1- Bonner, W. D., (1968), *Climatology of the low level je*t. Mon. Wea.Rev., Vol. 96, pp.833–850.

2- Doyle, J. D., Warner, T. T., (1993), *A three-dimensional numerical investigation of a Carolina coastal low-level jet during GALE IOP*. Mon Wea Rev, Vol. 121(4), pp.1030–1047.

3- Whiteman, C. D., Bian, X., Zhong, S., (1997), *Low-level jet climatology from enhanced rawinsonde observations at a site in the Southern Great Plains*. J Appl Meteor, Vol. 36(10), pp.1363–1376.

4- Colle, B. A., Novak, D. R., (2010), *The New York Bight jet: climatology and dynamical evolution*. Mon Wea Rev, Vol. 138(6), pp.2385–2404.

5- Rife, D. L., Pinto, J. O., Monaghan, A. J., Davis, C. A and Hannan, J. R., (2010), *Global distribution and characteristics of diurnally varying low-level jets*. J Clim, Vol. 23(19), pp.5041–5064.

6- Hu, X. M., Klein, P. M., Xue, M., Lundquist, J. K., Zhang, F. and Qi, Y., (2013), *Impact of low-level jets on the nocturnal urban heat island intensity in Oklahoma City*. J Appl Meteorl Climatol, Vol.52 (8), pp.1779–1802.

7- Berg, L. K., Riihimaki, L. D., Qian, Y., Yan, H. and Huang, M., (2015), *The low level jet over the Southern Great Plains determined from observations and reanalyses and its impact on moisture transport*. J Clim, Vol. 28(17), pp.6682–6706.

8- Vanderwende, B. J., Lundquist, J. K., Rhodes, M. E., Takle, E. S. and Irvin, S. L., (2015), *Observing and simulating the summertime low-level jet in central Iowa*. Mon Wea Rev, Vol. 143(6), pp.2319–2336.

9- Smith, E. N., Gebauer, J. G., Klein, P. M., Fedorovich, E and Gibbs, J. A., (2019), *The Great Plains low-level jet during pecan: observed and simulated characteristics*. Mon Wea Rev, Vol.147 (6), pp.1845–1869.

10- Blackadar, A. K., (1957), *Boundary layer wind maxima and their significance for the growth of nocturnal inversions*. Bulletin of the American Meteorological Society, Vol.38, PP. 283–290.

11- Holton, J.R., (1967), *The diurnal boundary-layer wind oscillation above sloping terrain*. Tellus,Vol 19, pp. 199–205.

12- Bonner, W.D., Paegle, J., (1970), Diurnal variations in boundary-layer winds over the south-central United States in summer. Mon. Weather Rev, Vol. 98, pp. 735–744.

13- Markowski, P and Richardson, Y., (2011), *Mesoscale meteorology in midlatitudes*, Wiley-Blackwell, ISBN: 978-0470742136. 430 pp.

14- Membery, D.A., (1983), *Low-level wind profiles during the Gulf Shamal*. Weather, Vol. 38, pp. 18-24.

15- Rao, P. G., Hatwar, H. R., Al-Sulaiti, M. H and Al-Mulla, A. H., (2003), *Summer Shamals over the Arabian Gulf*. Weather, Vol. 58, pp. 471–478.

16- Stull, R. B., 1988. *An Introduction to Boundary Layer Meteorology*. Kluwer Academic, 670 pp.

17- Liu, M., Westphal, D. L., Holt T. R. and Xu, Q., (2000), *Numerical simulation of a low-level jet over complex terrain in southern Iran*. Monthly Weather Review, Vol.128, pp. 1309–1327.

18- Alizadeh-Choobari, O., Zawar-Reza, P. and Sturman, A., (2014), *The wind of 120 days and dust storm activity over the Sistan Basin*. Atmospheric Research, Vol 143, pp. 328 –341.

19- Gevorgyan, A., (2018), *A Case Study of Low-Level Jets in Yerevan Simulated by the WRF Model*. Journal of Geophysical Research: Atmospheres, Vol.123, pp.300-314.

20- Vazifeh, A., Aliakbari-Bidokhti, A. A., Mazraeh Farahani, M., (2019), *A climatological study of the Low Level Jet in Central Desert of Iran (Dashte Kavir)*. Journal of the Earth and Space Physics, Vol. 45(3), pp. 687-704.

21- Bidokhti, A. A., Boromand, N., (2006), *Study of Gap Winds in the Lut Plateau*. Desert, Vol.11 (1), pp.13-30.

22- Mobarak Hass, E., Ghafarian, p., (2018), *Low- level Jet (LLJ) Simulation by Different WRF- Chem Boundary Layer Schema in Khuzestan province*. J. Meteorol. Atmos. Sci., vol 1(2), pp.287-303.

23- Giannakopoulou, E. M. and Toumi, R., (2012), *The PG summertime low-level jet over sloping terrain*. Q. J. R. Meteorol. Soc, Vol. 138, pp.145–157.

24- Du, Y., Chen, Y. L., Zhang, Q., (2015), *Numerical simulations of the boundary layer jet off the southeastern coast of China*. Mon Wea Rev, Vol.143 (4), pp.1212–1231.

25- Chen, F., & Dudhia, J., (2001), *Coupling an advanced land-surface/hydrology model with the Penn State/NCAR MM5 modeling system. Part I: Model description and implementation*. Monthly Weather Review, vol. 129(4), pp.569– 585.

26- Dudhia, J., (1989), *Numerical study of convection observed during the Winter Monsoon Experiment using a mesoscale two dimensional model*. Journal of the Atmospheric Sciences, vol. 46(20), pp.3077– 3107.

27- Mlawer, E. J., Taubman, S. J., Brown, P. D., Iacono, M. J. and Clough, S. A., (1997), *Radiative transfer for inhomogeneous atmosphere: RRTM, a validated correlated-k model for the long-wave*. Journal of Geophysical Research, vol. 120, pp.663– 682.